FACULTY OF SCIENCE AND TECHNOLOGY

Department of Geosciences

Characteristics and failure mechanisms of the Sieidi unstable rock slope

Interpreting slope kinematics at Sieidi from slope morphology, structural analysis, thin sections and 2D InSAR

Fabrice Kaltenrieder

Master's thesis in Hard rock geology, GEO-3900, May 2024

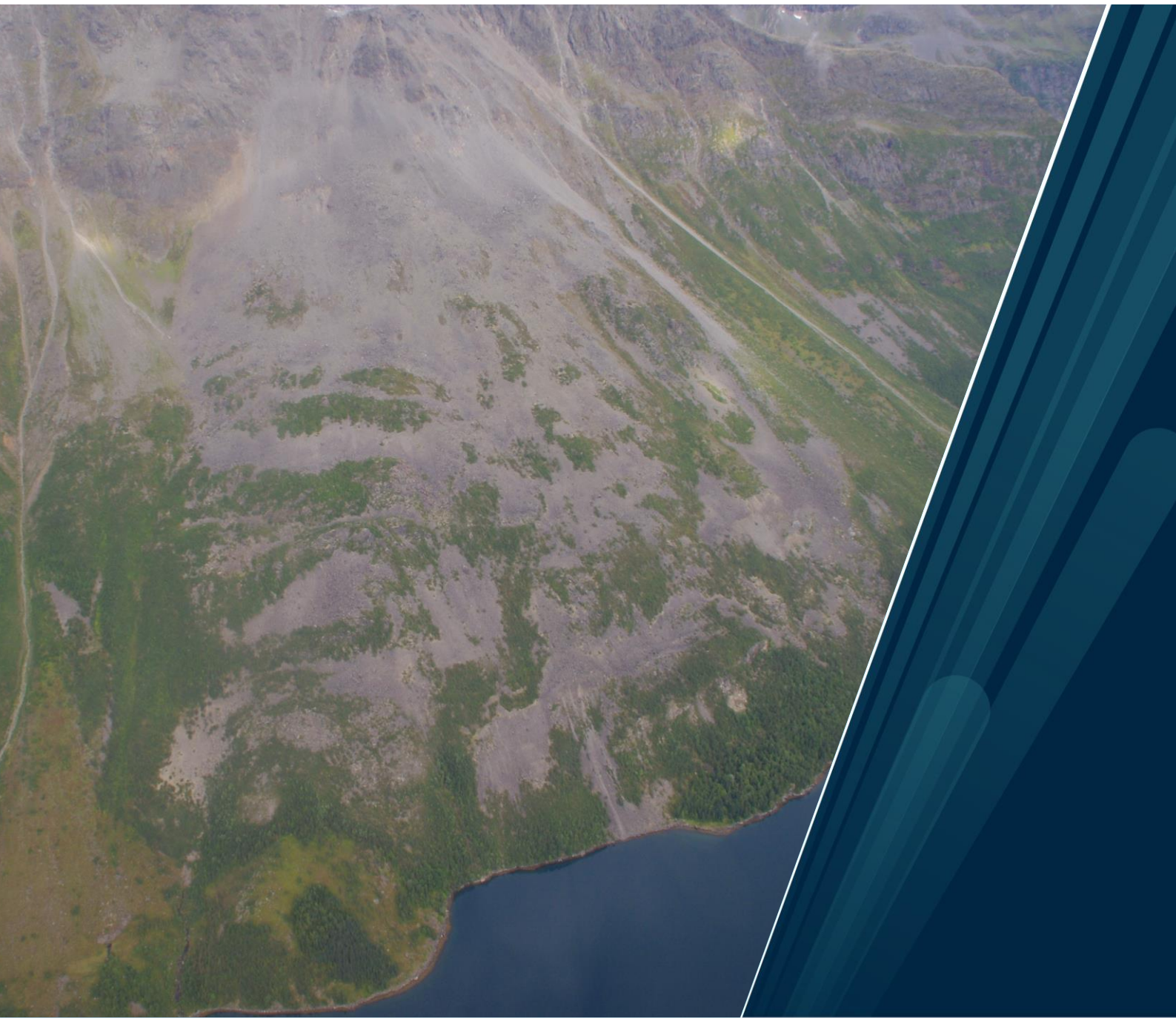

Cover photo by NGU

Abstract

Seidi is an unstable rock slope at the western end of the Sørfjord in Tromsø municipality, Troms County, northern Norway. It displays clear signs of rock slope deformation: an offset at the crest, multiple scarps, talus and loose material and a bulging slope. The objective of this work is to interrogate the failure mechanics in order to determine the degree of control lithology and bedrock structure have on the slope deformation and identify the underlying and kinematics and their influence on the deformation patterns of the Sieidi unstable rock slope.

This thesis outlines a multifaceted approach to the analysis of the kinematics, structural properties, and failure mechanisms of the Sieidi unstable rock slope (URS)in Troms County, northern Norway. The analysis of the Sieidi URS is based on 2D InSAR displacement rates, morphological observation, 416 structural measurements, and the analysis of 25 thin sections.

It elaborates on how structural discontinuities, namely schistosity planes and joint sets, are decisive factors of rock slope stability. Moreover, it accentuates the importance of the anisotropy of the rock since the microcracks form along the schistosity plane S1, which represents the main weakness zone in the rock mass that controlles the fracture propagation. It concludes clearly that the schistosity plane S1 (9°/246°) and joint sets denote the preeminent pathway for fracturing and failure propagation by interconnecting the schistosity and joint planes, leading to stepped fractures. The kinematic interpretation postulates a complex morpho-structural geometry with a translational basal failure mechanism with a convoluted component augmenting spatially towards the south. The rear rupture surface is controlled by joint set 1 (80°/103°), whereas the main morphological features, the major scrapes, are controlled by joint set 2 (89°/335). The observed joint sets play an essential role in weakening slope strength, deforming the slope and forming a basal and rear rupture surface. The unstable area, which has clear lateral boundaries shown morphologically and by InSAR spatial data, is moving a 9.8mm/a downwards.

In conclusion, the rock slope hazard classification system established by NGU classify the Sieidi unstable rock slope as a low risk object.However, the results of this study underscore the existing uncertainties and the need for sporadic monitoring and further investigation of the study area. The study also emphasises the usefulness of an integrated methodology approach in rock slope stability analysis and the urgency for future research efforts to refine monitoring techniques and to enhance the understanding of slope processes, thereby contributing to developing more effective slope stability management.

Table of contents

Figure table

List of tables

1 Introduction

1.1 Motivation

Landslides occur worldwide, in all climates, on land and underwater. They cause billions of USD in damage to infrastructure and to the economy and are responsible for thousands of casualties every year. With a growing population and an expansion of infrastructure, the problems will persist or get more severe with climate change (Highland & Bobrowsky, 2008).

Norway's mountains are defined in many parts by deep fjords and steep mountainous terrain continuously affected by several glacial cycles since their creation, e.g. isostatic uplift, weathering, and erosion. The country is extremely prone to landslides and experiences 2-6 major ones every century (R. L. Hermanns et al., 2014). Besides the destructive potential of these landslides by a direct hit, another threat emerges if they hit a body of water and cause a displacement wave. As many Norwegian settlements are located in proximity to the sea, this makes the communities vulnerable to these displacement waves, like the Tafjord disaster in 1934, which killed 40 people (Blikra et al., 2006).

The contingency of being affected by a landslide is small, but such an event can have catastrophic consequences for infrastructure and life. Therefore, the Norwegian Geological Survey (NGU) and the Norwegian Water Resources and Energy Directorate (NVE) work together to prevent such catastrophes. The NGU is responsible for catering geological information to the Norwegian society, mapping Norway's territory, identifying unstable rock slopes (URSs), and evaluating their failure potential and danger. The NVE monitors the high-risk slopes and needs systematic or continuous surveillance with appropriate tools. The NGU haffectedas determined over 300 unstable rock slopes throughout the Norwegian mainland, 130 of which are located in Troms County (NGU, 2024a).

Northern Norway's landscape is dominated by alpine settings, where the bedrock predominantly consists of a metamorphic rock mass with anisotropic properties. These conditions favour instabilities and, thus, also slope deformation as deformation follows zones of weaknesses such as discontinuities or preexisting structures (Vick et al., 2020). Therefore, it is fundamental to investigate and assess the regional lithologies, preexisting structures, and their geological history to understand the mechanical properties and failure mechanisms.

All in all, every unstable rock slope behaves differently since it is affected by local lithology, structures, morphology, and periglacial processes in its unique way. These parameters influence the possibility of slope failure, the magnitude of a possible event and the run-out zone. In any

case, all data about unstable rock slopes help us understand further how they behave and how slope deformation and failure mechanisms interact, leading to a better understanding of failure.

The unstable rock slope Sieidi is one of many creeping rock masses in the Ullsfjord (Figure 1). Opposite Seidi, across the fjord, are the mountains Stortinden, Piggtind and Skulvatinden, which contain multiple instabilities and rock glaciers along its mountain ridgeline. Further to the southwest, the mountain Laksvatnfjellet has instabilities, too. Therefore, the area stands out as a location of interest regarding the ground deformation map (Figure 11), as numerous highlighted rock slopes show ongoing movement. Work by previous master's students, namely Sandbakken (2021) on Piggtind and Skulvatinden and Rasmussen (2011) on Laksvatnfjellet, as well as published literature from academia and NGU reports (Eiken et al., 2013; Henderson et al., 2008; Vick et al., 2020) have aimed to interpret the failure mechanisms and solve the mysteries of the surrounding instabilities of Seidi.

It is exciting to further these studies by focusing on Sieidi for several reasons. Firstly, the structures and lithologies ought to be similar to those of the surrounding mountains like Piggtind or Laksvatnfjellet, despite the high deformation and the slope facing the opposite direction. Secondly, Seidi is a smaller instability with reasonably clear boundaries that can be easily interpreted by geomorphological observations, the deformation rate given by InSAR, and the assessment of a digital terrain model. Another advantage of the area being smaller is that it reduces the number of variables to be considered when analysing the failure mechanisms. This implies that the failure mechanism will be more straightforward to interpret than its neighbouring rock slope instabilities. Lastly, Sieidi has not been studied before and requires a detailed investigation.

1.2 Objective

The objective of this Master's thesis was to interpret the failure mechanisms of the unstable rock slope Sieidi in the Tromsø municipality (Troms County, Norway). This has been achieved through an assessment of the controlling structural and lithological parameters of the unstable slope, as well as its surroundings, by fieldwork and surface displacement by InSAR and ground-based radar.

Moreover, detailed geomorphological mapping of the slope was conducted, with a focus on gravitational structures, to interpret the extent and mechanism of the unstable rock slope to facilitate the decision-making and planning in the immediate surroundings of Sieidi, e.g. future monitoring and safety measures or follow-up studies. Furthermore, the results help to further the understanding of rock slope failures in the country.

This study aims to determine the degree of control lithology and bedrock structure have on the deformation at Sieidi. In addition, the aim is to investigate the degree of deformation of a rockslide compared to the stationary rock outside the lateral boundaries along the slope profile while variations in lithology are considered. Moreover, the research is concerned with assessing how structural parameters outside these limits influence the stability of the rock slope. Finally, the investigation aims to identify the underlying geometry and kinematics and their influence on the deformation patterns of the Sieidi unstable rock slope.

1.3 Study area

The Sieidi USR measures around 1.5 km^2 and is located at the western end of the Sørfjord (Figure 1) in Tromsø municipality, Troms County, northern Norway.

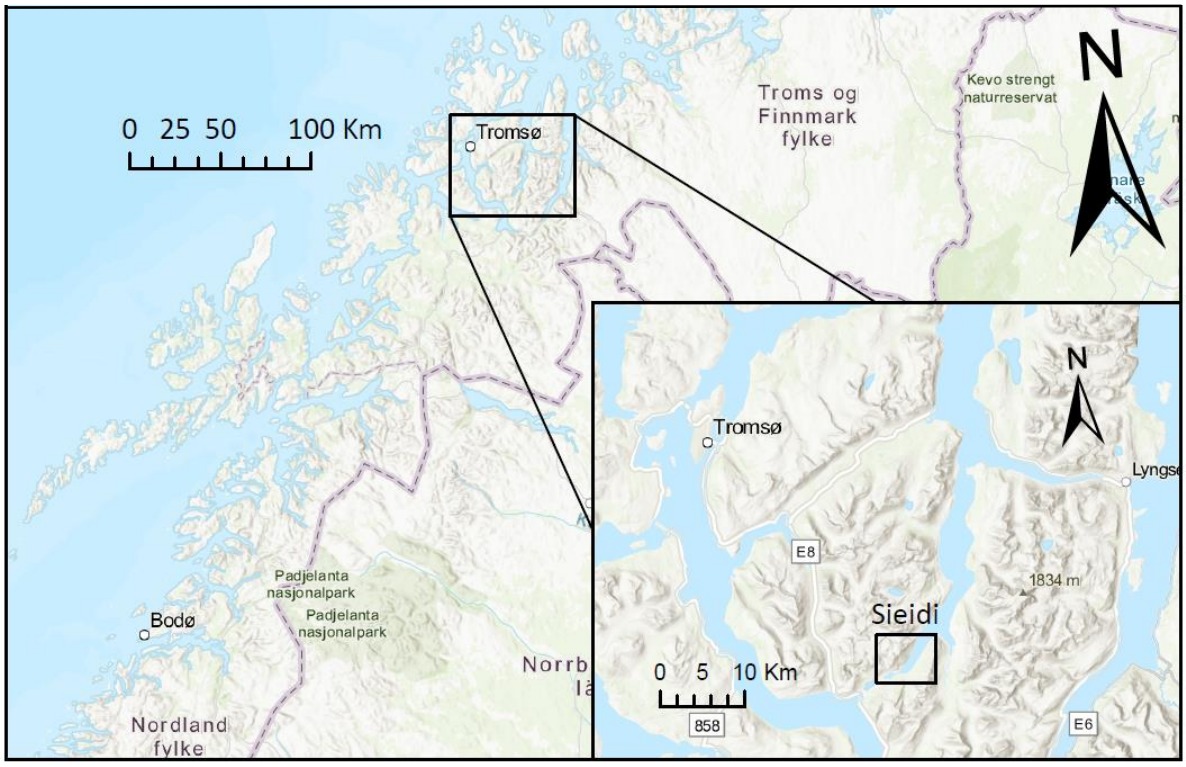

Figure 1 Overview of the study area; map drawn using ArcGIS Pro

Figure 3 Sieidi URS (Photo taken by NGU 2019)

The URS is situated on the southeast-facing slope of a mountain called Sieidi (northern peak 1045 masl, southern peak 1060 masl), with the backscarp between them (Figure 2). The average slope angle is 33° and has a dip direction of around 135° (Figure 2). The slope is covered by rockfall/talus deposits and disintegrated rock. In certain places, displaced blocks can be seen, which are related to landslide processes and slope deformation at hand.

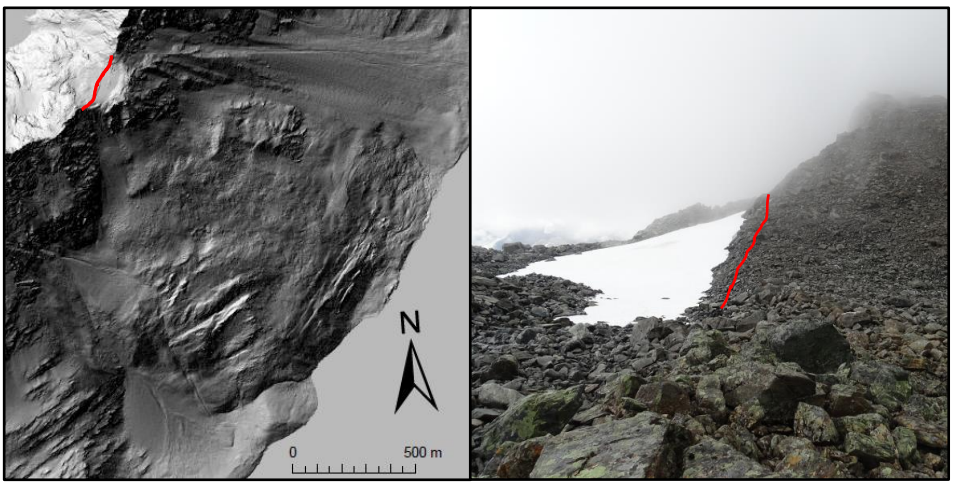

Figure 2 Hillshade map of the Sieidi URS with the backscarp indicated in red; DEM 1m resolution; developed in ArcGIS Pro

The vegetation cover varies in density and gradually gets thinner with altitude before ending around 400-450 masl. The area is sparsely inhabited, with the closest residential areas being on the other side of the fjord, Mellemjord and Grønvoll.

1.4 Climate

Troms County's variable topography and proximity to the coast lead to a wide variation of climatic conditions throughout the County. It has a subarctic climate with long winters and short summers. The coldest month is February, with an average temperature of -2 °C at the coast and -6 to -9 °C in the interior regions. The warmest month is July, with an average temperature of 11 to 12°C at the coast and 14°C inland. However, it is not unusual for summer temperatures to reach 28-30°C. The annual precipitation inland lies between 300-600mm, whereas in the coastal regions, it is 1000-1500mm per year (Dannevig, 2023).

Since Sieidi is situated far from the open sea but directly adjacent to the Sørfjord, it is influenced by it, meaning it gets a mixture of coastal and inland climate conditions. It gets around 850-950mm of precipitation each year. During October, the temperatures usually drop below zero for extended periods, and the first snow starts to settle. The snow cover lasts until May, depending on the altitude. Over 200 days show a daily minimum temperature below the freezing point, meaning that frosty nights can occur year-round (Meteorologisk institutt, 2023).

1.5 Regional Geology

Studying regional geology is essential to investigate the parameters influencing rock slope deformation, such as failure mechanisms and mechanical characteristics. Emphasis is put on preexisting structures and potential changes in lithology that could affect the rock slope on a large scale.

The mountainous area of northern Norway is part of the Scandinavian Caledonides (Figure 4). Its nappes are divided into four units: the lower, middle, upper, and uppermost allochthons (Steltenpohl et al., 1990). The peak metamorphic conditions increase westwards and structurally upwards (Ramberg et al., 2013).

In the Caledonian orogeny, during the Ordovician- Silurian period, the nappes were thrust onto the Baltic shield along ductile thrust faults after the closure of the Iapetus Ocean. They formed an imbricated foreland fold/thrust belt. Moreover, the nappes show a ductile thrust fault contact marked by a high degree of deformation along the shear zones (McKerrow et al., 2000; Northrup, 1996). According to Steltenpohl et al. (1990), the sediments were deposited in a marginal shelf environment before they formed the present lithologies.

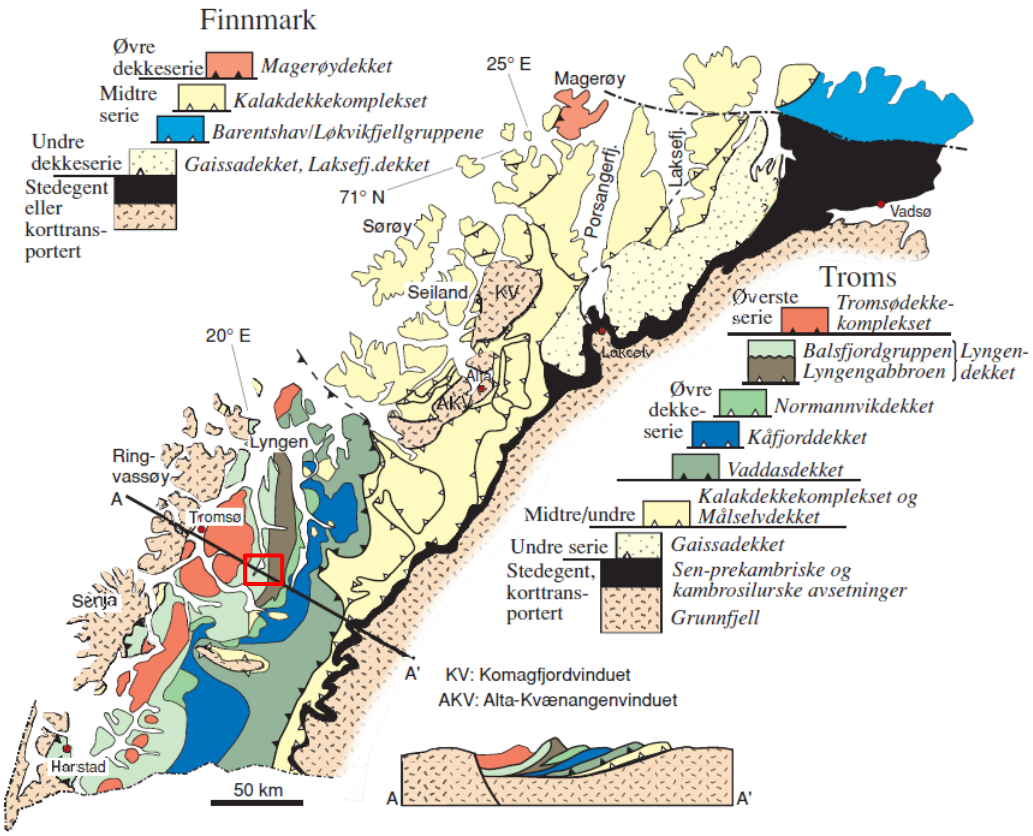

Figure 4 Regional geology of northern Norway; (Ramberg et al., 2013).

On the tectonic map, the study area is marked as part of the Balsfjord series (Zwaan et al., 1998) and belongs to the Uppermost Caledonian nappes (Steltenpohl et al., 1990). The area of the Sieidi URS is only mapped on a 1:250,000 scale by Zwaan et al. (1998) (Figure 7), and the geological map indicates, as seen in Figure 5 and Figure 7, that the predominant lithology (39) found is schist with various degrees of chlorite, muscovite and biotite. In the literature, it is often called the Malangen schist (Coker-Dewey et al., 2000).

The Balsfjord series shows an inverted metamorphic gradient with a Barrovian sequence from chlorite to sillimanite zones (Coker-Dewey et al., 2000).

The peak metamorphic conditions augment from tectonostratigraphic lower levels in the SE to higher levels in the WNW. Thermodynamic calculations estimated the P-T conditions of a maximum of 450°C and 6.5kbar in the garnet zone levels and 600°C and 8kbar in the uppermost levels, which are staurolite-bearing. The U–Pb dating of monazite gave a peak metamorphic age between ca. 425–435 Ma (Höpfl & Konopásek, 2023).

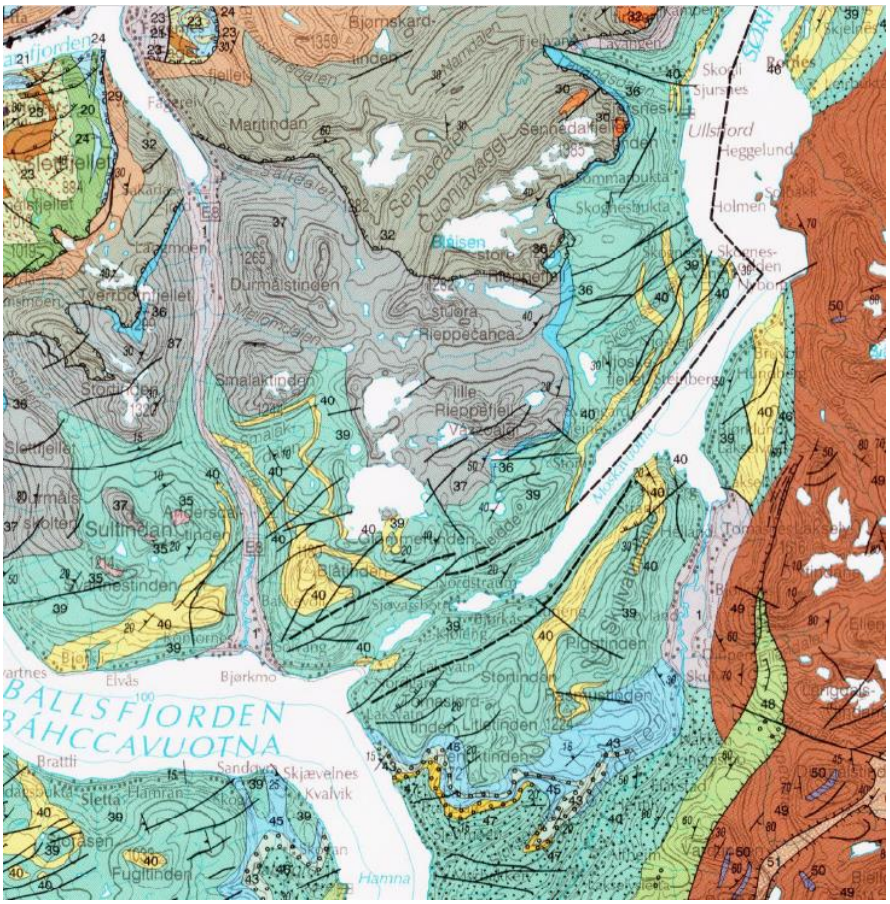

Figure 5 Geological map of Sieidi area, published by NGU; mapped by Zwaan et al. (1998)

1.6 Post-Caledonian brittle structures

Basins and fjords occur along major faults, which derive from the collapse of the Caledonian orogeny, several rifting and extensional events in the Paleozoic, and the opening of the Atlantic Ocean from the late Palaeozoic to the early Cenozoic (Bergh et al., 2007; Indrevaer et al., 2013).

According to Bergh et al. (2007), there were three rifting and extensional events. The first event occurred during the Permian-Jurassic period and formed NNE–SSW–trending normal faults dipping ESE and WNW. The second occurred in the Early to Late Cretaceous period and formed NE-SW to ENE-WSW-striking normal faults. Lastly, the third event resulted in the opening of the North Atlantic Ocean and formed NE-SW-trending normal faults.

During the opening of the North Atlantic Ocean, by continental extension, followed by continental break up and seafloor spreading in the late Palaeozoic to the Early Cenozoic, northern Norway's North Atlantic passive margin formed (Koehl et al., 2019). This divergence was simultaneous with the formation of extensional fault complexes offshore, e.g. the listric Troms–Finnmark Fault Complex or onshore, e.g. the planar Vestfjorden–Vanna Fault Complex (Figure 6), both trending in an NE-SW and ENE-WSW direction and dipping towards the SE (Bergh et al., 2007; Indrevaer et al., 2013; Koehl et al., 2019). The most pronounced and biggest of these faults are also represented on the geological/tectonic map (Figure 7), and all indicate a strike direction of NNE–SSW- and ENE–WSW (Koehl et al., 2019; Zwaan et al., 1998).

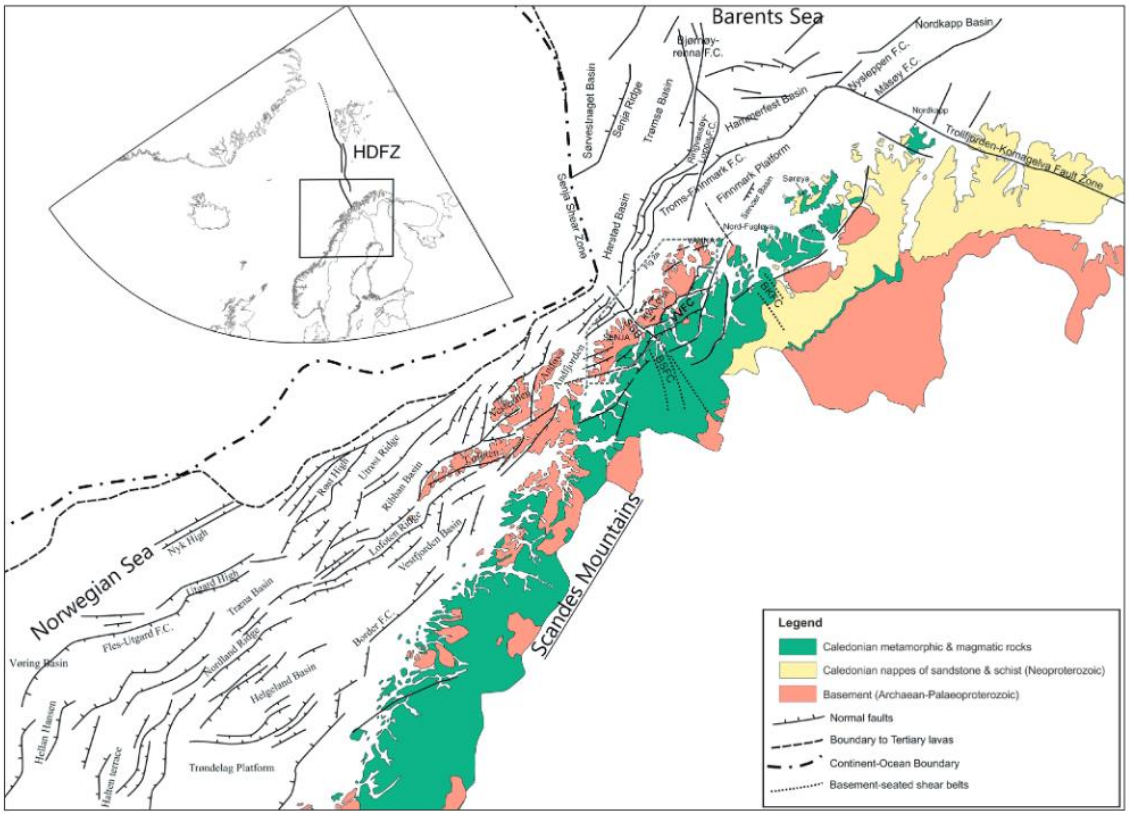

Figure 6 Onshore-offshore tectonic map of northern Norway (Indrevaer et al., 2013)

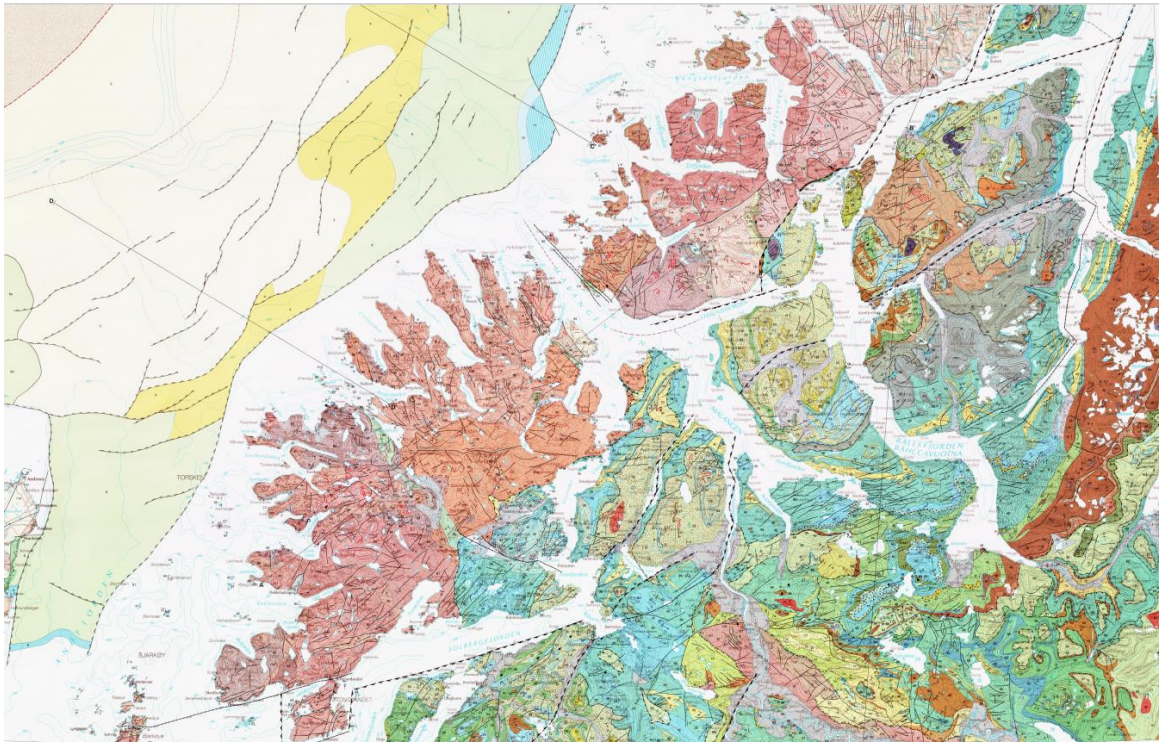

Figure 7 Geological map Tromsø, published by NGU; mapped by Zwaan et al. (1998)

1.7 Geomorphology and Quaternary geology

A geological quaternary map (Figure 8) published by the Norwegian Geological Survey (NGU) is publicly available on a 1:250,000 scale and has been mapped by Lysså (1999). The map used aerial photographs and photographs taken from the other fjord side as data.

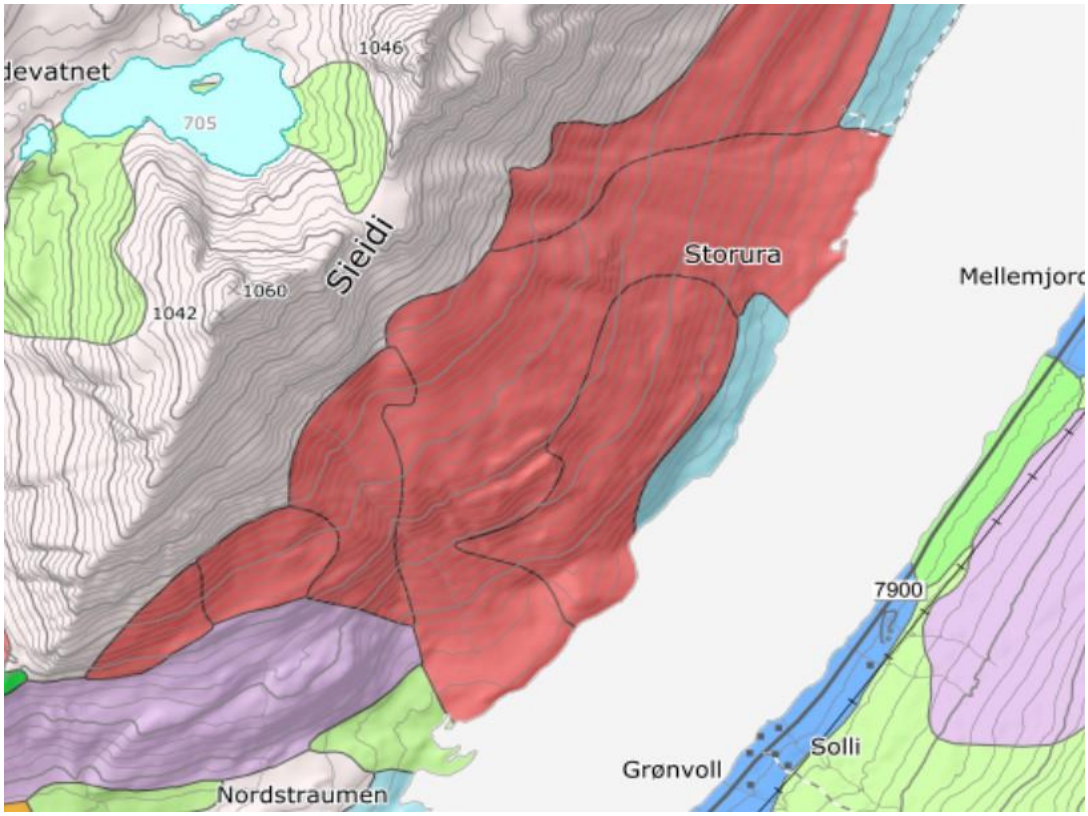

Figure 8 Quaternary map of the Sieidi area; published by NGU; mapped by Lysså (1999)

The map conveys a general understanding of the area, but a 1:250,000 scale is insufficient for a more detailed study. The map shows that the area is covered by Snow and Rock avalanche deposits (red), and close to the sea, it is mapped as sea, fjord, and beach deposits (blue). In the SW, it is classified as moraine deposits.

1.7.1 Glaciation

During the Quaternary, considerable changes in environmental conditions have occurred. During this period, temperatures fluctuated frequently and varied in severity, resulting in glaciation and inter-glacial periods (Olsen et al., 2013). These climate changes are the result of several parameters, such as the influence of the Milankovitch cycles, changes in the chemical composition of the atmosphere, the position of the continents, and the effect of orogenies (Bradley, 2015). The periods of glaciation and melting influenced the topographical setting by erosion and sedimentation. The last glacial maximum (LGM) in the Troms County dates to 25ka-18ka before present (B.P.) when the Fennoscandian ice sheet reached its furthest extension (Olsen et al., 2013). However, there were several advances and retreats of the ice sheet after the LGM in the Troms County region, like the Younger Dryas event, which was 11ka-10ka B.P., the Ørnes event, which happened 9.9ka-9.8ka B.P. and the Skibotn event taking place during 9.6-9.5ka B.P.. Once the ice sheet started to melt and its weight had been decreasing, the continental plate began to rise in order to obtain an isostatic equilibrium (Ramberg et al., 2013).

Glaciation can cause over-steepening and deepening of rock slopes and valleys through erosion. This process can be amplified along pre-existing bedrock fabrics and structures that are oriented in a favourable orientation, leading to an augmentation of the internal rock stress. With the retreat of the ice, the rock slopes are left without the support of the glacier, and the pressure it exerts may destabilise the over-steepened rock slopes as the augmented stress might surmount the rock strength. This excess energy is often realised as tensile stress along pre-existing bedrock fabrics and structures oriented in a favourable direction. This process is called debuttressing. The above-mentioned isostatic uplift also contributes to the weakening of over-steeped rock slopes as the relief increases in the uplifting area. Those are the major processes of glaciation affecting rock slope stability, which can result in a multitude of failure mechanisms (Ballantyne, 2002; Böhme, 2014).

1.8 InSAR

1.8.1 Theory

Interferometric Synthetic Aperture Radar (InSAR) uses microwaves to record ground surface movements, with accuracy up to less than one millimetre a year. In geoscience, it is used, for

example, to detect slow ground deformation rates (Crippa et al., 2021) like in unstable rock slopes (Vick et al., 2020) or to investigate the seasonal effects on the permafrost landforms (Rouyet et al., 2019). The data relevant to this thesis is collected by the Sentinel-1A/-1B Synthetic Aperture Radar satellites from the EU Copernicus programme and processed with a Persistent Scatter Interferometry (PSI) method (Ferretti et al., 2001).

The results are publicly available on the InSAR Norway mapping service (https://insar.ngu.no/). The satellites move along a polar orbit around the Earth and transmit pulsating electromagnetic waves in the microwave spectrum towards the Earth's surface. These pulses are emitted and travel through the atmosphere along a specific line of sight (LOS) (Figure 9), and are reflected back to the satellite upon hitting the surface. The sensor detects the signal with its amplitude and phase components. The phase component is correlated to the distance between the satellite and the ground surface, whereas the amplitude reflects the characteristics of the substrate hit by the microwaves. It is possible to measure the phase difference between two measurements of the same spot taken at different times, which relates to the surface displacement along the LOS (Lauknes, 2010; NGU, 2024b).

The satellites move in opposite directions along their polar orbit, one from N to S, called the descending pathway, or from S to N, termed an ascending pathway (Figure 9). Using Sentinel-1, the LOS is always towards the right along the direction of movement, resulting in the ascending satellites having an LOS directed towards E-NE and the descending satellites having an LOS looking towards W-NW. Therefore, the detected changes measured are well represented in the E-W plane but poorly constrained in the N-S plane (Eriksen et al., 2017; NGU, 2024b). To remedy this, a necessary N-S LOS can be achieved using a third observation direction, e.g. using a ground-based radar.

The aim is to record changes to the sensor-to-ground distance within a pixel over time because this represents the relative displacement rate. However, the collected data always has noise that must be filtered out. Phase changes may be caused by changes in vegetation or variations in the snow cover that might be wrongly interpreted as movement (Eriksen et al., 2017; NGU, 2024).

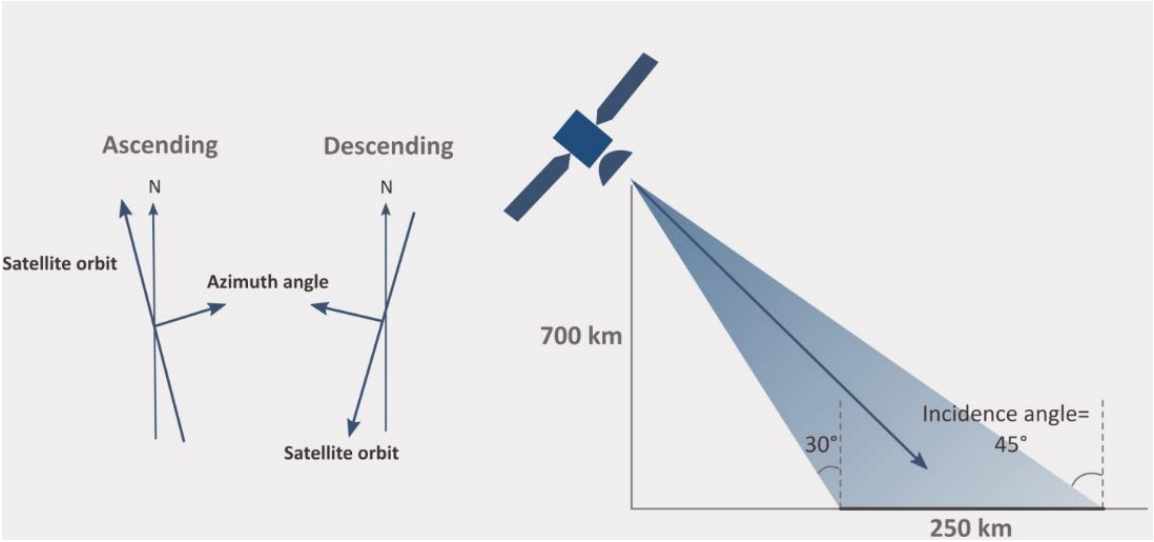

Figure 9 Left: ascending and descending satellites. Right: the average line of sight LOS (NGU, 2024)

Moreover, atmospheric noise must also be filtered out. This process might be incomplete in deep valleys due to strong effects of the stratosphere. Another source of noise is the wetlands because the water level can change and affect the ground properties (NGU, 2024b). Since noise is always present, it is important not to analyse single pixels with potentially unrepresentative displacement patterns but the behaviour of a more significant area in order to understand the displacement rate of a whole landform.

To solve the problem of snow cover in Norway, InSAR Norway only uses the data collected during the snow-free months, and then the years can be connected by extrapolating between the documented seasons (NGU, 2024b). Yet, this must be done with caution and not used as truth since landslides do not always behave linearly. This intrapolated information is only to be used to get an interannual overview.

Other limitations of the InSAR include, firstly, on steep mountain slopes facing the satellite, foreshortening/layover can occur, which leads to an ambiguous mix of reflected signals along the slope.

Secondly, the datasets available on InSAR Norway are processed as tiles of 5x5 kilometres. It is challenging to accurately align and merge these tiles because they are each processed individually. Thus, the boundaries of the tiles may show a linear shift of the displacement values (NGU, 2024b).

1.8.2 2D InSAR used for displacement trend interpretation

Identifying all the geomorphological elements in the field is very complex and time-consuming, and for a deformed rock slope even impossible since the superficial disintegrated rock or talus

obscures morphological structures, rendering them challenging to discern. Moreover, secondary structures can be observed within primary structures, augmenting the slope complexity.

InSAR displacement maps can help define the boundaries of landslides. Additionally, 2D InSAR cross-sections provide estimated deformation rates and provide a more comprehensive understanding of the relationship between movement along the basal-rupture surface and the morphological features involved (Figure 10). This approach further helps in determining the structures that control the deformation process (Eriksen et al., 2017; Frattini et al., 2018).

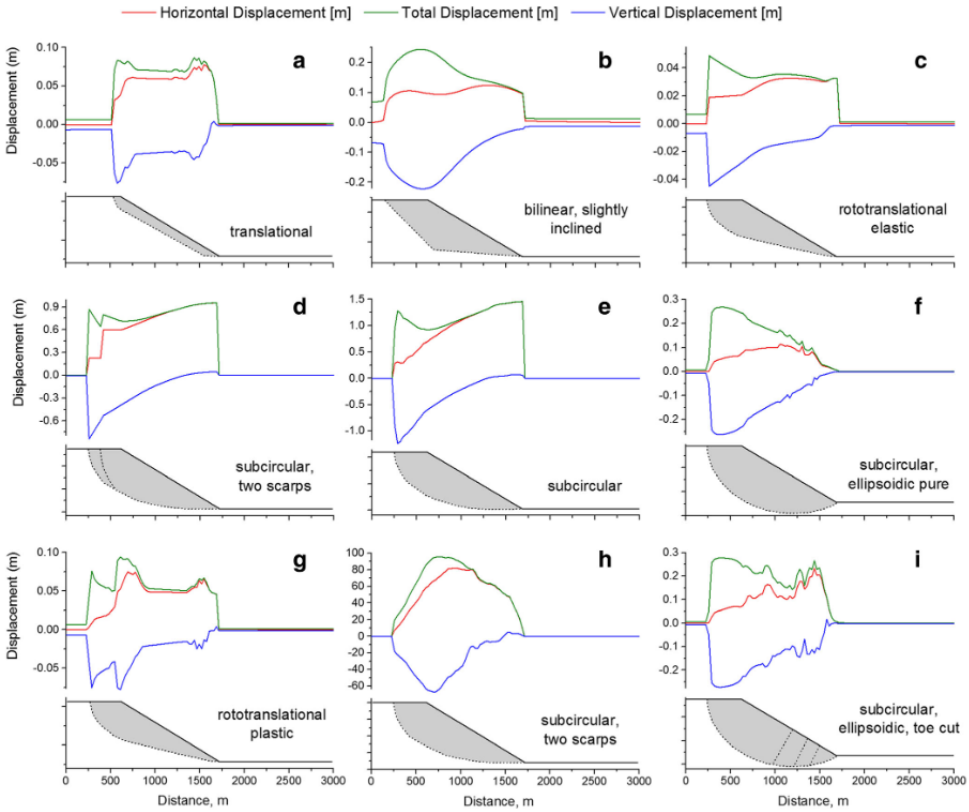

Figure 10 Examples of how structural variations of URS change the vertical velocity measured along the surface. a, b Translational landslides. c, d Rotational slide with different toe displacements. e, f Rotational slide within an inactive and a partially active deeper phenomenon. f, h Rotational slide with semi-graben and multiple scarps and a secondary active; (Frattini et al., 2018)

Several factors contribute to longitudinal changes of InSAR displacement rates along a landslide. These are the geometry of the rupture surface (at the rear and basal ends), the positioning of the LOS regarding the displacement vectors along the slope, the characteristics of the substrate or the presence of other features, e.g. secondary landslides, rock glaciers, solifluction or scarps. A positive change in vertical displacement indicates upward movement of the slope, which is observable in rotating or compressed toe domains. Conversely, a negative change in vertical displacement indicates a sub-vertical movement caused by a scarp or secondary landslide. Between the extensional and compressional parts of a biplanar landslide or in the circular midpoint of a rotational landslide, the overall displacement may be close to zero. This could be due to it shifting from a sub vertical to a more horizontal movement, i.e. from rotating/roto-

translational to planar or sub-planar basal rupture surface. Internal rock mechanics influence how displacement vectors are directed. Brittle scarps show a sudden change in vector direction as they become more vertical, and ductile or progressively deformed scarpes exhibit gradual, curved chances of displacement vector directions. Rotational displacements exhibit larger variations and more complex changes along their longitudinal profiles in contrast to translational, planar, or biplanar landslides (Frattini et al., 2018).

1.8.3 InSAR Norway data of the Sieidi URS

The unstable rock slope Sieidi is one of many creeping rock masses in the Ullsfjord. Opposite Seidi, across the fjord, are the mountains Stortinden, Piggtind and Skulvatinden, which contain multiple instabilities and rock glaciers along its mountain ridgeline.

Further to the southwest, the mountain Laksvatnfjellet has instabilities, too. They can all be identified easily on the InSAR map (Figure 11) by the accumulation of red or blue points (the colour changes if the other satellite is chosen).

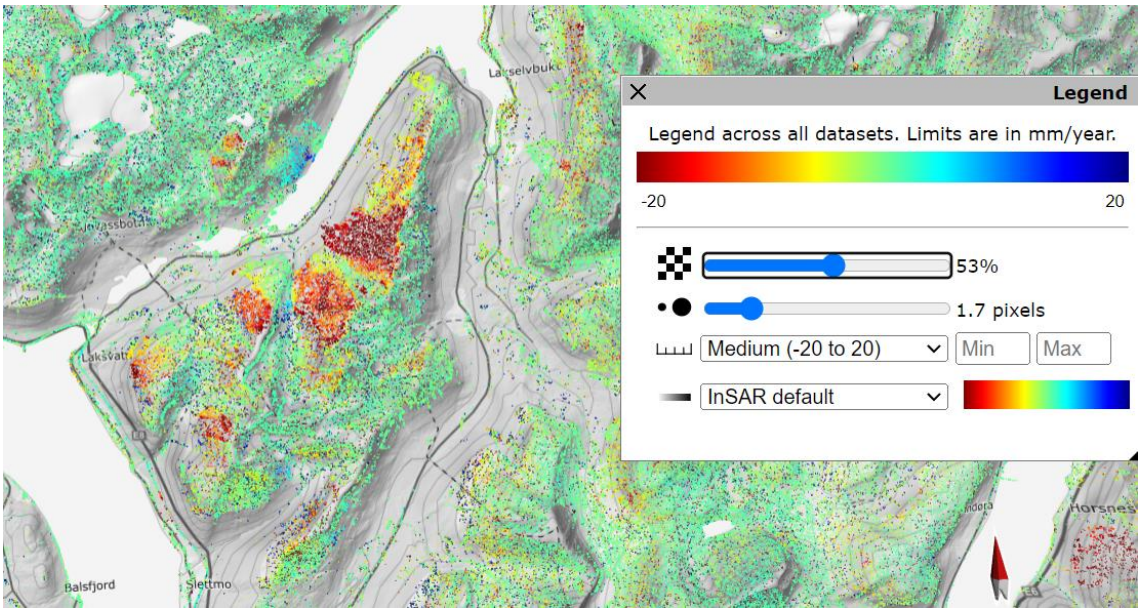

Figure 11 Annual displacement rate of landslides in the area (Descending 1; 2019-2023); (Screenshot from https://insar.ngu.no, April 2024)

The average displacement velocity of the study area is around 9.8 mm/year while considering 14'942 points of measurement taken from InSAR Norway. As shown in Figure 12, the displacement rate varies significantly between different areas of the same landslide. The most significant displacement is considered to be surface movement and not related to the deformation of the rock slope.

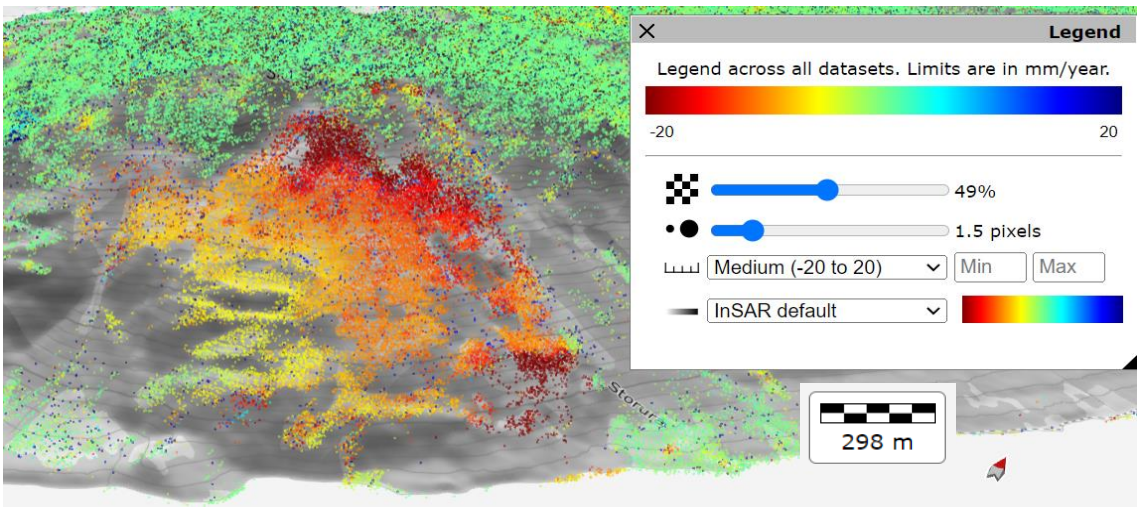

Figure 12 Annual displacement rate (Ascending 1; 2019-2023); (Screenshot from https://insar.ngu.no, April 2024*)*

InSAR data from InSAR Norway is only one-dimensional. Hence, it detects movement only along the LOS direction, which is different for the ascending and descending orbits. This represents a significant drawback since movement is seldom aligned completely parallel to the LOS (Wright et al., 2004). For a complete comprehension of the magnitude of the real displacement, it is essential to gain a thorough understanding of the movement direction in relation to the LOS (Samsonov et al., 2019) which is enabled by 2D InSAR datasets provided by NORCE. They merged two overlapping SAR geometries with different LOS to estimate combined 2D displacement (mean annual velocity). The combination ensures the best possible spatial coverage. Moreover, it enables the 2D velocity vector to be decomposed into a horizontal (E-W) and vertical (up-down) vector component. It allows the visualisation of 2D displacement rates in map view along a topographic profile and the vertical velocity measured along the surface. The outcome of these calculations is presented in the chapter "Results".

2 Theory

2.1 Classification

Landslides are the movement of material down-slope when gravity acting on the material exceeds the resisting force of the slope. They can happen suddenly or over a long period (BGS, 2023). Sometimes, the term mass wasting is also used, which Allaby (2020) describes as the displacement of Earth material down-slope through gravity acting on the material.

Varnes (1978) published the best-known classifications for landslides and then Hungr et al. (2014) updated the old classification (Figure 13) and described 32 types of landslides and provided a definition of each.

The mass wastings are categorised by the type of movement along the mountain slope and the kind of material enmeshed. The type of movement is divided into six kinematic movements: fall, topple, slide, spread, flow and slope deformation. Out of these six movements, slide and slope deformation are the most relevant for the Sieidi RSD.

Type of movement	Rock	Soil
Fall	1. *Rock/ice* fall[a]	2. *Boulder/debris/silt* fall[a]
Topple	3. Rock block topple[a]	5. *Gravel/sand/silt* topple[a]
	4. Rock flexural topple	
Slide	6. Rock rotational slide	11. *Clay/silt* rotational slide
	7. Rock planar slide[a]	12. *Clay/silt* planar slide
	8. Rock wedge slide[a]	13. *Gravel/sand/debris* slide[a]
	9. Rock compound slide	14. *Clay/silt* compound slide
	10. Rock irregular slide[a]	
Spread	15. Rock slope spread	16. *Sand/silt* liquefaction spread[a]
		17. Sensitive clay spread[a]
Flow	18. *Rock/ice* avalanche[a]	19. *Sand/silt/debris* dry flow
		20. *Sand/silt/debris* flowslide[a]
		21. Sensitive clay flowslide[a]
		22. Debris flow[a]
		23. Mud flow[a]
		24. Debris flood
		25. Debris avalanche[a]
		26. Earthflow
		27. Peat flow
Slope deformation	28. Mountain slope deformation	30. Soil slope deformation
	29. Rock slope deformation	31. Soil creep
		32. Solifluction

Figure 13 Varnes' classification system (Hungr et al. 2014)

Catastrophic rock slope failures are characterised as a rock slope failure that undergoes a hefty fragmentation of the rock during the runout with an influence on an area bigger than the one of a rockfall (R. L. Hermanns & Longva, 2012). They usually have a volume bigger than 10^6 m^3 and a through-going rupture plane between the sliding rock mass and the underlying rock body. They present a hazard to society because physical measures cannot usually neutralise a failure of a large unstable slope due to its potentially enormous volume, reach and velocity (5- > 100m/s), and they can also prompt secondary events. Therefore, they can have catastrophic

consequences (R. L. Hermanns & Longva, 2012). A failure can be defined as the moment a body loses cohesion under stress and divides into several parts (Allaby, 2020). Thus, rock slope failure can be characterised as the rapid mass movement of a rock mass down a slope, driven by gravity (Braathen et al., 2004).

2.2 How do slopes deform and fail?

The deformation of landsides occurs in different stages. They can be divided into pre-failure, syn-failure and post-failure deformation (Figure 14&Figure 15) (Hungr et al., 2014). The rock mass undergoes progressive slope damage accumulation and propagation, i.e. rock bridge degradation and destruction of roughness and asperities (Stead & Eberhardt, 2013), both at the rear and along the lateral boundaries of the deforming rock mass. It progresses based on spatial orientation and spacing of pre-existing structures, i.e. foliation, joints, folds and faults. These rupture surfaces advance through the rock mass by utilising these weakness zones until it reaches a point where failure becomes kinematically possible(Elmo et al., 2018; Stead & Eberhardt, 2013). Hence, failure is a progressive process that starts with the initiation of slope damage and is followed by the gradual buildup of slope damage, ending with an eventual failure of the slope (Vick et al., 2020). The Sieidi URS is currently in the pre-failure stage, with the accumulation of slope damage.

The response to stress and strain is constrained by the rock's lithology and its spatial distribution of structures on all scales. If the discontinuities are closely spaced, they have an important control -combined with the properties of the intact rock- on the rock mass' strength. In contrast, if the discontinuities are well-spaced, the properties of the intact rock are the main controlling factor (Hoek et al., 2002).

The failure of the slope marks the most noteworthy deformation stage of slope deformation as it indicates the development of a continuous rupture surface. Unstable rock slopes do not necessarily undergo only one major failure event as they can occur as small frequent failures over a period of time, or they can show sudden or progressive large-scale failure or slow non-catastrophic deep-seated slope deformation. Some might even never show a major failure (Agliardi et al., 2001, 2012; Hungr et al., 2014; Leroueil & Locat, 1996).

An intact rock mass does not undergo failure. Consequently, any deformation that takes place is concentrated within the already damaged zones of the rock mass. Thus, all deformation acts on pre-existing deformation, discontinuities, and weaknesses. The process of deformation and failure is primarily influenced by gravitational forces, with failure transpiring when the shear stress surpasses the shear strength (Stead & Eberhardt, 2013; Vick, 2023).

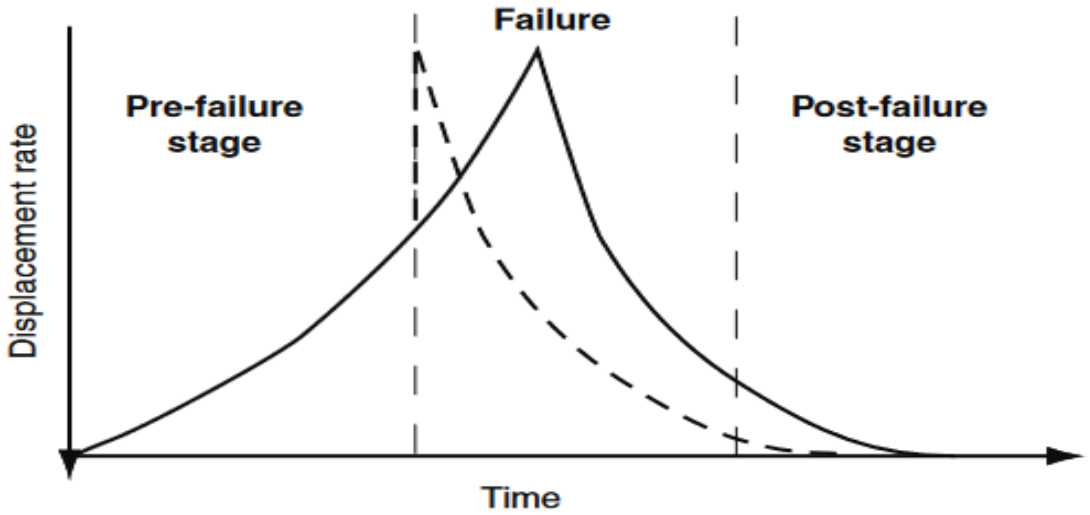

Figure 14 Different stages of slope movement leading to rock-slope failure (Hermanns & Longva, 2012)

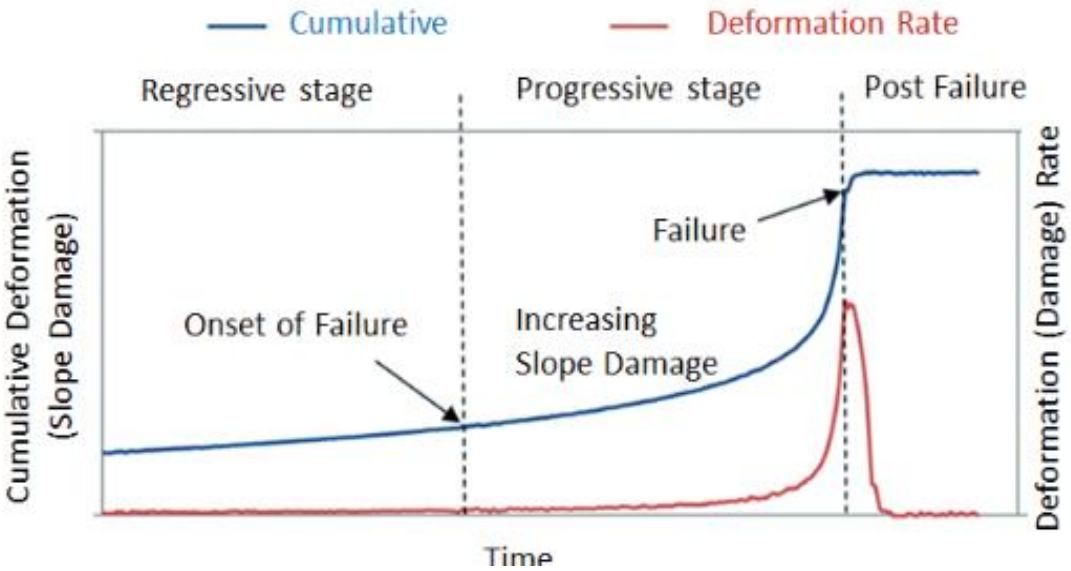

Figure 15 Different stages of slope deformation and damage in deforming rock slopes (Stead & Eberhardt, 2013)

2.3 Slope deformation

As shown in Figure 13 there are two different types of slope deformation of a rock mass. The parameter that distinguishes these two types primarily is scale.

Firstly, rock slope deformation (RSD) is within the range of heights of up to a couple hundreds of meters, often occurring in a weak rock mass. Further characteristics are that the deep-seated slope deformation often shows extremely slow movement rates. Additionally, a sagging of the

crest with the formation of faults and cracks is often observed without developing a well-defined rupture surface (Hungr et al., 2014).

Secondly, mountain slope deformation (MSD) is a large-scale rock mass deformation (bigger than RSDs), often showing morphological structures like scarps, benches, bulges, cracks, and trenches. MSDs lack a fully developed rupture surface, and they move very slowly to even unmeasurable velocities (Hungr et al., 2014). MSDs are often called deep-seated gravitational slope deformation (DSGSD). They can be described as the movement of an extensive mass on high-relief walls, which reaches from the valley or fjord floor all the way up to the ridge crest. They usually have a volume superior to 0.5km^3, low displacement rates and badly defined lateral boundaries (Agliardi et al., 2012). Moreover, certain morphological structures are exemplary for DSGSDs (Figure 16). The upper part of the slope often shows extensional or mixed deformation conditions, expressed by morphological features like double-ridges, depressions, trenches, graben structures, scarps, and counterscarps. The lower/frontal part of the slope often displays signs of compression, which can be observed as toe bulging and buckling and signs of secondary failures are frequently present (Agliardi et al., 2012).

DSGSDs' main controlling kinematic mechanisms are the multitude of basal sliding planes on which the body advances (Agliardi et al., 2001). According to Crosta et al. (2013), these sliding planes are shear zones with a thickness of up to 10m made out of cataclastic breccias in a fine matrix. The resulting decreased permeability and shear strength are considered to be the main controlling factors of contemporary deep-seated gravitational slope deformation.

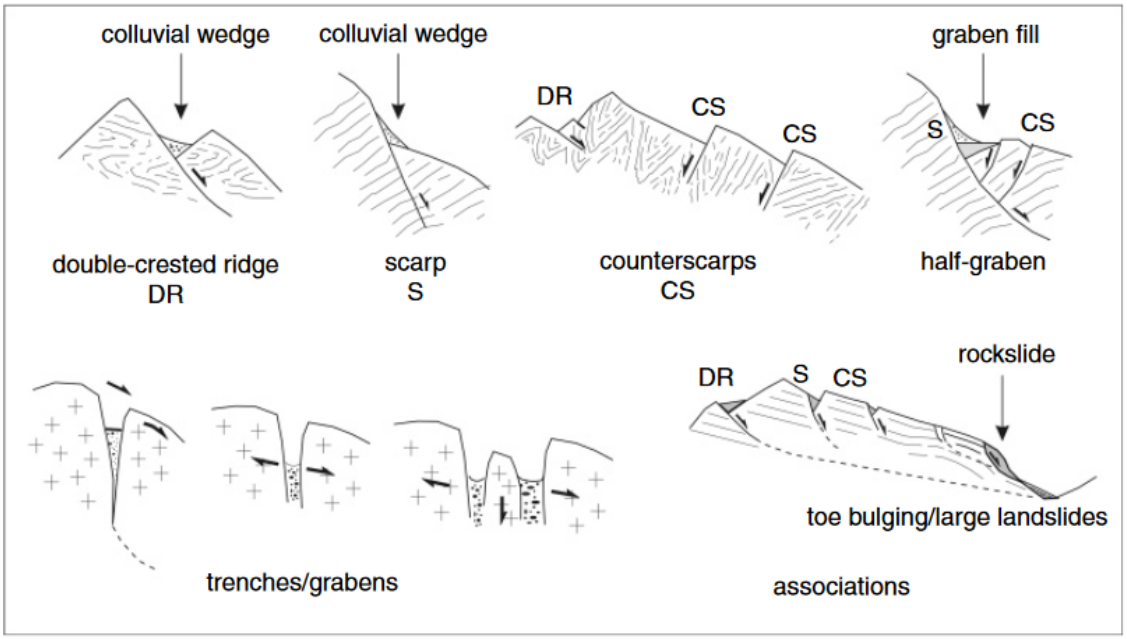

Figure 16 2012 Morpho-structural features of DSGSD (Agliardi et al., 2012)

2.4 Slides

Rock slides are classified along a spectrum, with rotational and translational slides being the two end members. Because the transition is gradual, it is difficult to distinguish them in the field (Hungr et al., 2014; Zangerl et al., 2008).

Rotational slides (Figure 17) chiefly take place in mechanically isotropic rocks, moving on a concave curved rupture surface and moving at slow to moderately slow velocities. Due to the rotational movement, there is little internal deformation except for the lower part of the slope, where even uplift is possible. At the top of the slope, the movement is steep to almost vertical, leading to the surface being tilted backwards toward the scarp, which can result in the formation of depressions or trenches (Highland & Bobrowsky, 2008; Hungr et al., 2014; Zangerl et al., 2008).

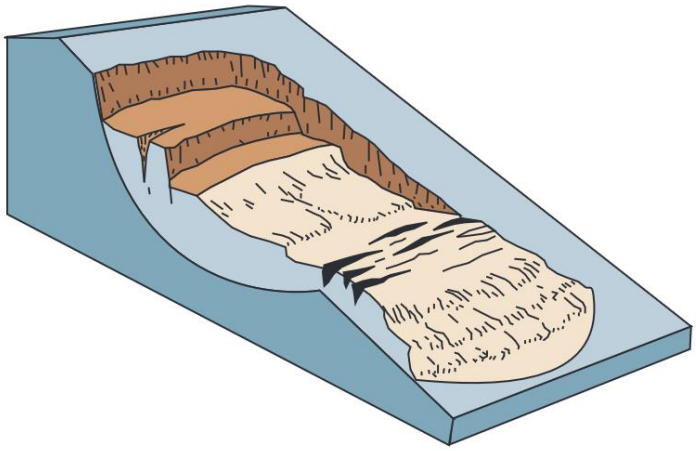

Figure 17 Schematic depiction of a rotational slide (Highland & Bobrowsky, 2008)

Translational slides (Figure 18) occur in layered metamorphic or sedimentary rocks, where the failure happens along fault planes or schistosity planes, and in intrusive rocks, where the failure occurs along stress relief joints (Highland & Bobrowsky, 2008; Hungr et al., 2014). They move along a planar rupture surface with little to no rotation or internal deformation, and they move with extremely rapid velocities. In addition, these slides have a high probability of occurring in the same spatial areas where they happened in the past (Highland & Bobrowsky, 2008; Hungr et al., 2014). Wedge sliding is a special form of translational slide since both have similar kinematics. The rupture surface in a wedge slide comes from two downslope facing and intersecting planes, i.e. sliding or discontinuity plane (Highland & Bobrowsky, 2008; Hungr et al., 2014; Zangerl et al., 2008).

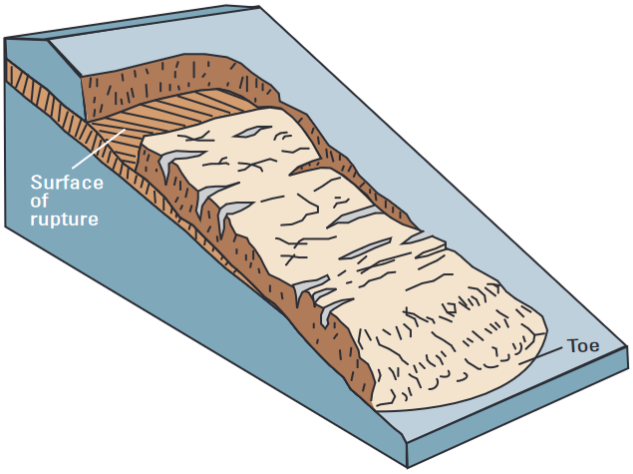

Figure 18 Schematic depiction of a Translational slide (Highland & Bobrowsky, 2008)

A further difference between the end members is the fact that rotational slides tend to restore the slide equilibrium, whereas translational slides can progress unrestrained over large distances if the sliding surface is inclined enough (Highland & Bobrowsky, 2008; Zangerl et al., 2008).

Lastly, compound and irregular slides are a lot more complicated in terms of kinematics and failure mechanisms. Compound slides have a more sophisticated gliding surface, often made of several planes or having an uneven curvature surface. In these slides, kinematic movement down-slope requires internal distortion, which results in the formation of horst and graben structures at the head. Irregular slides move on an irregular gliding surface comprised of randomly oriented joints which are disjointed by intact rock, i.e. rock bridges (Hungr et al., 2014).

2.5 Landslides in Troms County

All landslides in Trom County except the Mannfjellet URS (rotational slide) exhibit movement along shear zones, foliation or faults since the rocks present are too competent to develop into a rotational slide. Rotational slides occur most commonly in homogeneous, weak isotropic rock masses, like tuff, shale or marl (Bunkholt et al., 2012).

Furthermore, rock slope failures and related displacement waves represent one of the main geohazards to human life or infrastructure in Norway. For example, in 1934, in the Tafjord disaster, 40 people were killed by a displacement wave caused by 3,000,000 m^3 of rock mass falling into the ocean (Blikra et al., 2006). During the last 120 years, more than 250 people have lost their lives due to rock slope failures in Norway (Solhaug, 2015).The alpine relief with fjords reaching far inland and former glacier valleys that are over-steepened and lack the support of the ice creates a morphology in Troms, which is very favourable to landslides. In addition, there are exacerbating factors such as the favourable structural conditions and the periods of intense

Holocene precipitation, snowmelt and freezing/thawing periods. Moreover, because the landscape is mountainous in Troms, most people live close to the coast. Thus, the greatest danger for these communities are displacement waves caused by rock slope failures (Harbitz et al., 1991).

According to NGU (2024), more than 160 unstable rock slopes have been mapped in the Troms County (Figure 19). The spatial distribution of unstable rock slopes in Troms clusters to the East and West of the Lyngen Alps and on the Eastern side of Storfjorden (Bunkholt et al., 2012). The detected landslides mainly occur in mica schist and can be classified according to their deformation characteristics as: sagging slopes, toppling failures, compound slides, translational slides, and rotational landslides (Blikra et al., 2006; Bunkholt et al., 2012). The deadliest rock avalanche in Troms happened in 1819 in Lyngen and claimed 14 lives as a result of a displacement wave impact (Blikra et al., 2006).

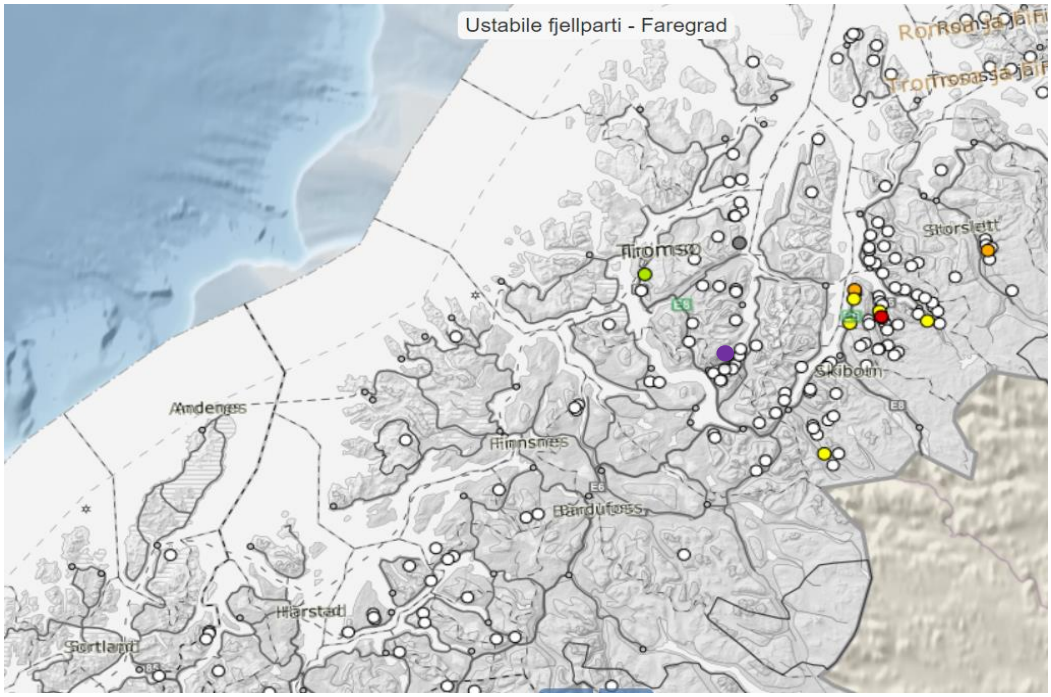

Figure 19 Mapped unstable rock slopes in Troms County; Purple Sieidi URS, green hazard level low, yellow hazard level middle, orange hazard level high and red hazard level very high; Mapby NGU (2024)

3 Methodology

The different methods applied were a desktop data study, the conduction of fieldwork investigation in order to collect rock samples and to map geological structures as well as map the bedrock, and the investigation of the thin section to identify potential small scale weakness zones and identify micro scale contributing factors to the weakness of the rocks mass.

3.1 Desktop data study

The desktop investigation aimed to get familiar with the field and what to expect before starting the fieldwork, and it was consulted to create a geomorphological map of the study area.

The geological/tectonic map in 1:250,000 by Zwaan et al. (1998) (Figure 7) and the Quaternary map in 1:250,000 by Lysså (1999) (Figure 8) were consulted to prepare for fieldwork.

To further investigate and study the area a project was created in ArcGIS Pro (ESRI) version 3.1.3 with the coordinate system ETRS 1989 UTM Zone 33N_1.

The Digital Elevation Models (DEMs) are publicly available and are provided by *hoydedata.no*. After uploading them (NDH Jiehkkevárri 2pkt 2017) to ArcGIS Pro, they were merged to a single DEM with a resolution of 1m. Furthermore, using this DEM, several hillshades with different lighting angles were made to enhance the morphological features. To be able to compare the hillshades to Orthophotos, the orthophoto series from Tromsø mainland and Lyngen taken on 27-07-2020 were exported from *norgeibilder.no* in a 0.1m resolution and imported to ArcGIS Pro project.

Additionally, photographs taken by NGU out of a helicopter on 17-08-2019 and 15-08-2023 were used for the desktop study.

Using all the data mentioned above and field observations, a geomorphological map was produced using ArcGIS Pro.

3.2 Fieldwork

The fieldwork focused on taking structural measurements of foliation planes and fracture planes. Furthermore, samples were taken to investigate the bedrock geology and for thin section analysis. The fieldwork was conducted during several excursions between 15-08-2023 and 25-10-2023. For the data acquisition, I was some days assisted by a fellow master's student (3x) and two professionals from NGU (2x), who also provided a helicopter for one day.

The focus was on getting measurements from outside the lateral boundaries of the Sieidi URS. Therefore, 17 different locations (Figure 18) were chosen to collect data, and 2 sites within the URS (M2/M3) were collected to compare them. Moreover, the morphology presented was recorded to support the digital data and draw a geomorphological map of the study area.

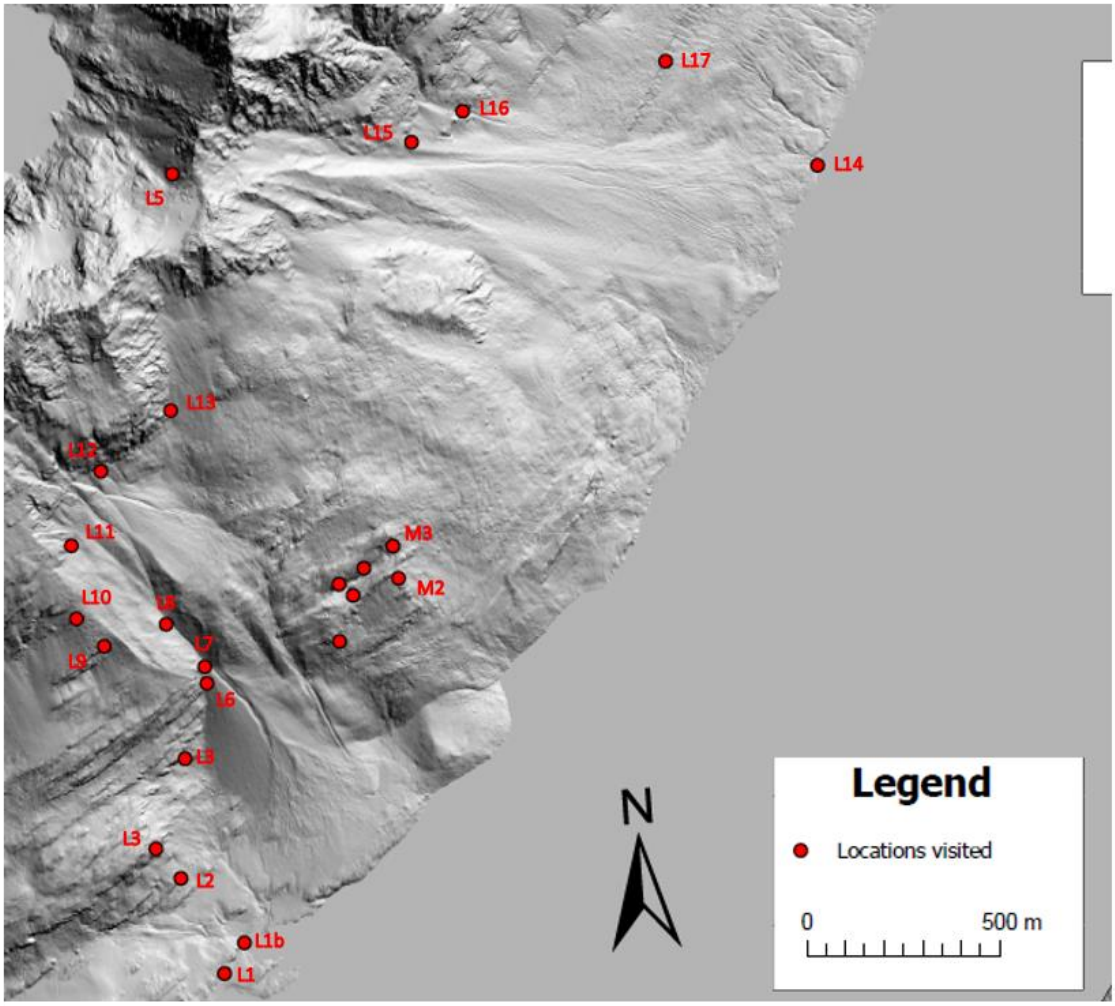

Figure 20 Map showing where the measurements were taken, developed using ArcGIS Pro.

The structural measurements were taken with a geological Suunto MC-2 compass and a Samsung Galaxy A53 5G using the application FieldMove Clino Pro version 2.5.19 with a declination of 10.69999981 In total. 281 fracture planes and 135 foliation planes were measured in the form of dip direction and dip. This data was processed by using the Rocscience software Dips 8.025. To analyse the poles of the measurements, a lower hemisphere, polar, equal area stereographic projection was chosen. The measurements were divided into three joint sets and one foliation set. Next, the variability cone for each set was displayed using one standard deviation (68.26%).

Rock samples were collected at all the locations (excluding: 1, 2, 7) outside the lateral boundaries of the Sieidi URS. They were collected with the help of a geological hammer in a location where it was assumed that the rock was in situ. Moreover, parts of the displaced rock mass were used

to gather two samples within the URS. While a sample was collected, its orientation in space was recorded by taking pictures after the sample was separated from the bedrock. The samples were classified using field observations, the expertise of NGU and Dr.Carly Faber and the website www.alexstrekeisen.it.

3.3 Thin section

The samples were cut into blocks of approximately 4 cm length, 2 cm width and 1 cm height, perpendicularly to the foliation, with a diamond-enforced rock saw (Figure 21). If the sample was big enough, two blocks were sawed out for the production of two thin sections; otherwise, two thin sections from the same block were ordered from the laboratory. The thin sections were polished to a thickness of 30 µm to then be analysed under a polarised microscope.

Figure 21 Sample blocks (left), Rock saw used (right)

In total, 25 thin sections were analysed by a Leica DMLP microscope (Figure 22), 21 originating from the stable part and 4 from within the URS. They were studied in terms of their mineralogy and microstructures both in plan polarised (PPL) and cross polarised (XPL) light. To capture the results as an image, a Leica DM 4500 P microscope was used, which was retrofitted with a scanning stage (Figure 22). The pictures were all taken in regard to the orientation in the field, i.e. the part facing the sky is at the top of the image. The findings are used to qualitatively interpret the rock strength and mechanisms of failure at a microscale.

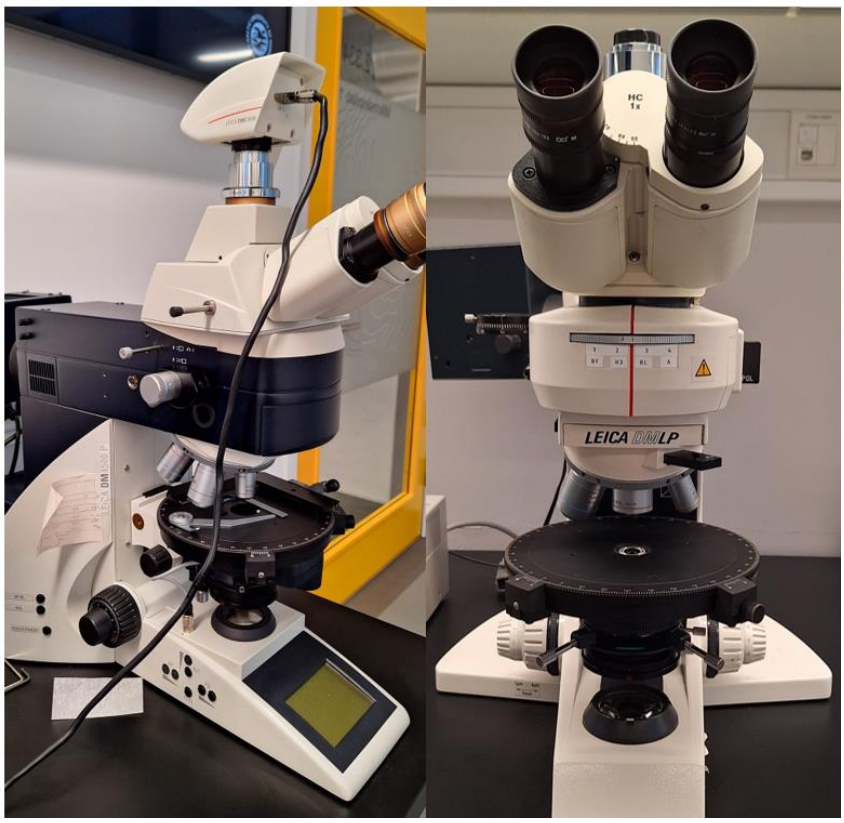

Figure 22 left Leica DM 4500 P microscope; right Leica DMLP microscope

3.4 InSAR

NORCE provided the 2D InSAR data. They merged two overlapping SAR geometries with different LOS to estimate combined 2D displacement (mean annual velocity). One ascending geometry (Sentinel-1 (20219-2023) Ascending 2 (As-6-160) data from InSAR Norway) and one descending geometry (Sentinel-1 (2019-2023) Descending 1 (D1-4-095) from InSAR Norway. The 2D calculation has been further constrained based on a 10m DEM from the Norwegian Mapping Authorities, assuming zero movements perpendicular to the slope direction.

The results have been analysed to determine the basal rupture geometry based on the work of Frattini et al., (2018) Intrieri et al., (2020) and Sandbakken, (2021). The subsequent instructions delineate the process for assessing the depth and geometry of the basal rupture surface, following the vector inclination method proposed by (Intrieri et al., 2020) (Figure 23).

The process involves several steps.

1. One needs a cross-section of the landslide with the displacement vectors displayed. It is important to note that the first vector should accurately represent the movement near the back scarp.

2. The normal (yellow line) is drawn to selected vectors (blue arrow), the intersections between two consecutive normals are determined, and the angle is measured.

3. The angel is divided by two, and a bisection line (green line) is drawn between the two consecutive normals.

4. To determine the first point of the sliding surface, a line(dotted line) parallel to the first displacement vector is drawn. The line starts at the back scarp and ends at the intersection with the first bisection line.

5. The following line is perpendicular to the next normal and drawn from the end of the last line until the intersection with the next bisection line. This systematic process is repeated for each movement vector, creating a series of lines that represent the sliding surface.

6. The entire procedure is repeated, beginning from the toe of the landslide and working upslope. This results in a second sliding surface, which can be interpolated with the first one. This ensures a comprehensive understanding of the geometry of the landslide. However, this step can be challenging as it necessitates the identification of the toe area, which can be difficult in complex slope deformations. (Crosta et al., 2013).

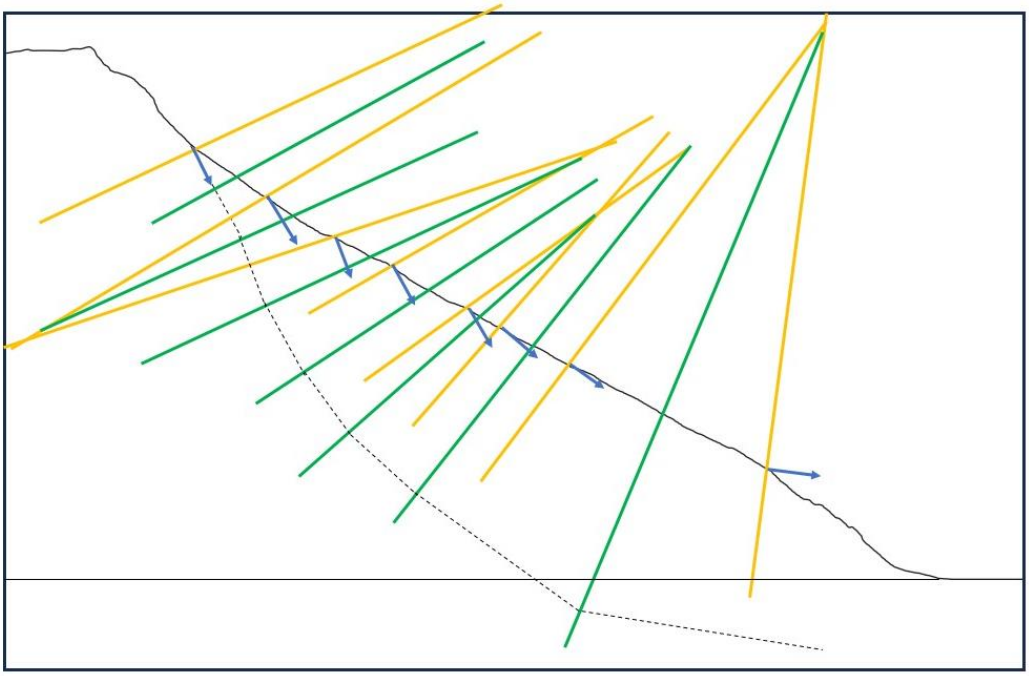

Figure 23 Graphical method to interpret the geometry and depth of the basal rupture surface (dotted line); normal line (yellow), bisection line (green), displacement vectiors (blue)

4 Result

The subsequent chapter presents the results. The observations of disparities in bedrock lithologies, with a petrological description, are presented, followed by the description of the geomorphological map of the study site and its features. Furthermore, structural orientation data is presented in two parts, the first being the foliation and the second being the joint sets. The results are presented as stereographic projections and field observations. The subsequent section presents the results of the thin section analysis, providing a comprehensive overview of the micro scale characteristics of the sampled rocks. Lastly, the InSAR section showcases the spatial extent and variations in velocities are shown in various formats, each providing a distinct perspective to display the data.

4.1 Bedrock/lithologies/ petrographic observations

It is essential to determine the level of anisotropy in rocks, as rock materials exhibiting anisotropic behaviour undergo variations in their mechanical properties when subjected to stress in various directions. By identifying weak planes and understanding the anisotropic nature of the rock mass, valuable insights can be gained regarding potential failure points. The area of the Sieidi URS is part of the Balsfjord series (Zwaan et al., 1998), meaning it is underlain by metamorphosed bedrock from the Caledonian orogeny. The rock mass has undergone a greenschistfacies metamorphism (e.g. Höpfl & Konopásek (2023); Zwaan et al. (1998)), and in the study area, two lithologies can be identified, phyllite in the lower altitudes and schist in the top part, with a gradual change rather than an abrupt transition. Thus, it is not possible to define a line where the lithology changes.

The rock samples are grouped into three categories: phyllite, transitional group and schist (Figure 24). They differ in metamorphic grade and, therefore, in the mineral assemblage of quartz, chlorite, muscovite, and biotite. The percentage of chlorite decreases with a higher metamorphic grade compared to the increasing percentage of biotite. This results in a change from a chlorite phyllite to a muscovite schist to a biotite-muscovite schist. The biotite grains differ from fine to coarse, the latter of which can be identified with the naked eye.

The samples collected at the locations 3, 4, 6, 8, 14, 15, 16, M2, and M3 (Figure 20) are classified as phyllites.

The samples 9, 10, 11 and 17 (Figure 20) show characteristics of both phyllites and schists. Therefore, they are grouped as members of a transition zone.

Samples from locations 12, 13 and 5 (Figure 20) represent schists, with the sample collected at location 5 being the most apparent representative of that lithology.

Figure 24 Examples of different lithologies at Sieidi; L3/L15/L14 phyllite, L11 transitional group, L13&L5 schist; In the order from southern bottom lateral boundary to the summit to the northern bottomlateral boundary.

The dominant minerals at Sieidi are quartz (qz), muscovite (ms), chlorite (chl) and biotite (bt). Since different oxide minerals never represented more than 5% of the modal mineral assemblage, they were omitted and considered unimportant for rock strength.

In the phyllite, the mineral assemblage fluctuates from 35-50% quartz, from 30-55% muscovite, from 10-30% chlorite and 0-5% biotite.

In the transition group, the mineral assemblage varies from 35-40% quartz, from 15-30% muscovite, from 15-50% chlorite and from 0-15% biotite.

In the mica schist, the mineral assemblage fluctuates from 35-45% quartz, from 20-25% muscovite, from 10-20% chlorite and from 15-25% biotite. The percentage and grain size of biotite increases towards the back scarp at location 5.

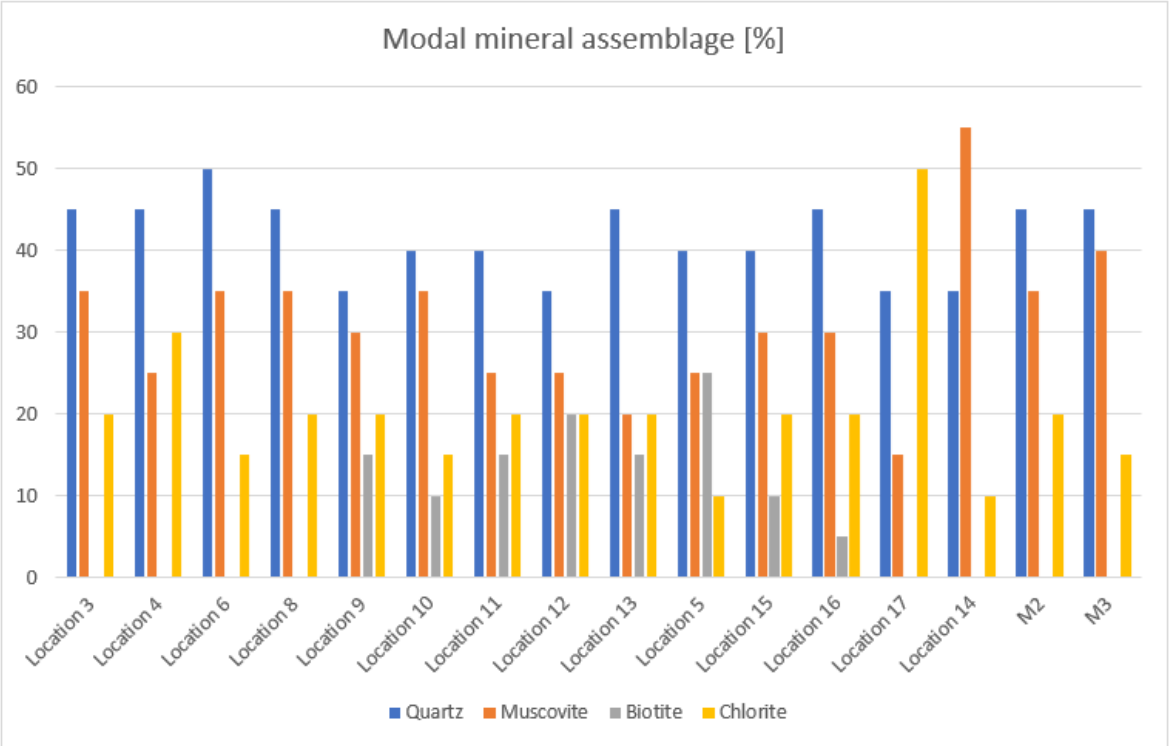

Figure 25 Mineral assemblage observed in each sample; the samples are listed according to the altitude recorded with location 5 representing the highest location and 1&14 the lowest.

The mineral composition varies from sample to sample, as seen in Figure 25 and Table 3. The grain size indicated is comparable between the minerals where “very fine” (VF) means smaller than 0.15mm, “fine” (F) 0.15-0.3mm, “medium” (M) 0.3-0.5mm and “coarse” (C) bigger than 0.5mm.

Furthermore, the rock mass in the Sieidi area marks a well-developed schistosity (S1) along different phyllosilicate mica minerals. In some places, two different generations (S2) of schistosity can be observed by the naked eye (Figure 26)

Figure 26 Two generations of schistosity S1 (green) and S2 (red)

4.2 Morphology

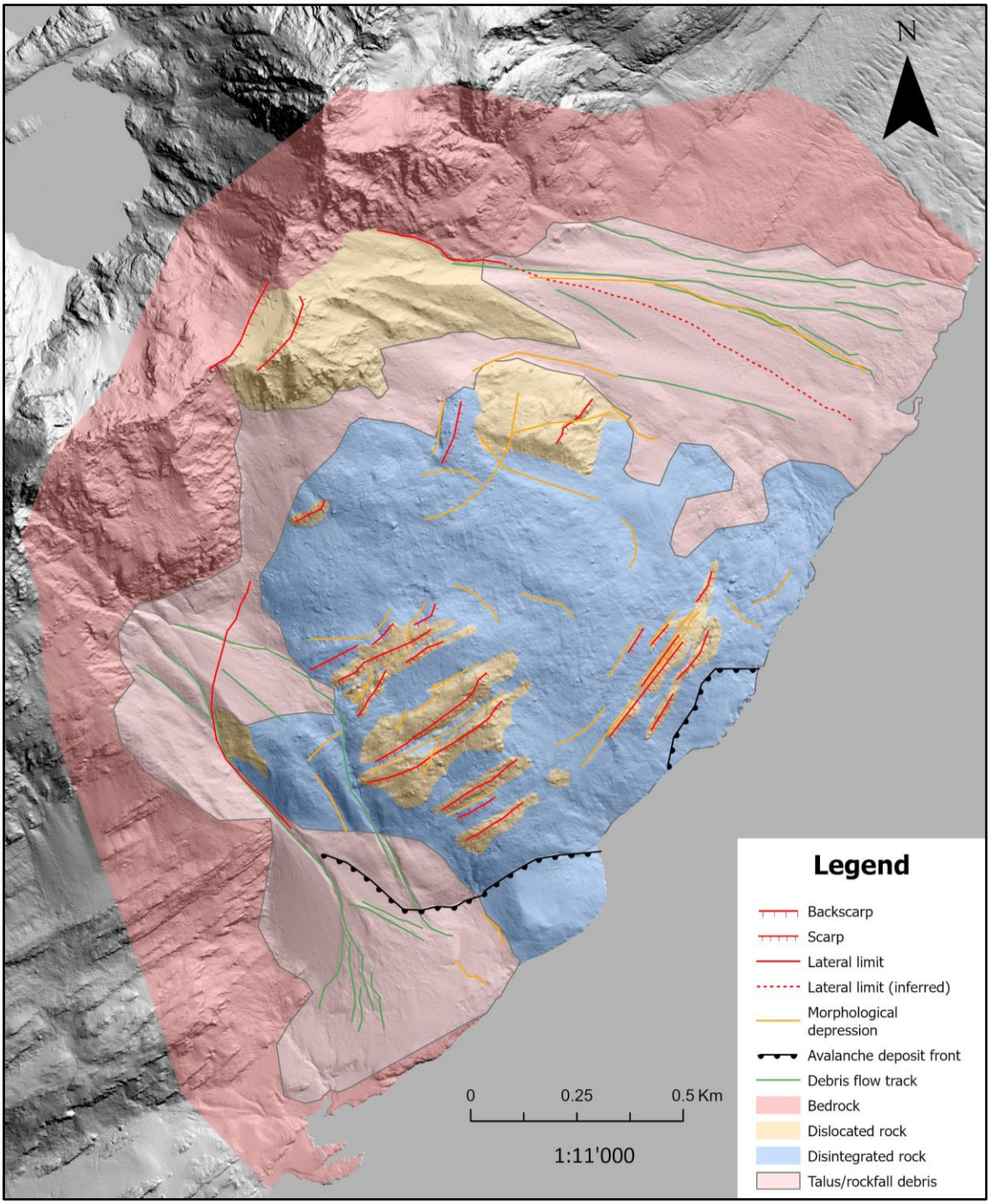

Figure 27 Morphological map of the Sieidi URS; drawn in ArcGIS Pro

Seidi is a smaller unstable area relative to other URS in the region, for example, Piggtinden or Nordnesfjellet. It exhibits a slope bulge within well-contained and clear lateral limits in the northwest and southeast. It is a SE-facing slope with an average dip direction of roughly 135°. It has an average slope angle of 33°, with an inclination up to 55° in the steepest, northwestern parts of the URS. The most prevailing morphological elements at Sieidi are a back scarp (Figure 28), scarps, depressions, debris-flow channels/lobes, ridges, and bulging in the toe area. The study area comprises intact bedrock, disintegrated, disaggregated rock and talus/rockfall debris (Figure 27).

The slope is mainly covered by disintegrated rock, and in certain areas, dislocated blocks penetrate the boulder field and are visible as scarps or counterscarps. Talus and rockfall debris cover the slope between the bedrock and the disintegrated rock (Figure 3). Below the tree line, vegetation has grown in areas with low to no disturbance for plant growth (Figure 30). The back scarp is challenging to see in the field, firstly because it is not well developed, and a vast displaced block obscures the view, which makes it only observable from the top. Secondly, large boulders cover it, and sometimes snow/ice (Figure 28). Nonetheless, in studying the DEM, the back scarp is clearly visible, as shown in Figure 28. A clear indication of slope movement are the major scarps in the southern part of the URS striking in a NE-SW direction (Figure 29 & Figure 30). The rock mass shows a drop of up to 20m from the head of the scarp to the boulder field. The area around the major scarps is densely covered by vegetation, and the area in between is made up of mainly boulders (Figure 29). Around the scarps further upslope, the vegetation decreases as the altitude reaches the vegetation limit. More minor scarps can be observed in the toe area, which are covered with boulders and strike in an NNE-SSW direction (Figure 30). In the vicinity of these scarps, the vegetation is absent, too. Some morphological depressions below the vegetation limit are covered, whilst others are not. Furthermore, several debris flow tracks are observed at both lateral boundaries that follow natural drainage paths (Figure 31). These paths are easily recognisable on the DEM, even if tracing them in the field is difficult. In addition, within the URS, there is no evidence of debris flow tracks. All the field observations, together with the interpretation of the photographs taken and the orthophotos available on “norgeibilder.no” with the study of the DEM, are summarised on the morphological map of the Sieidi URS area in Figure 27.

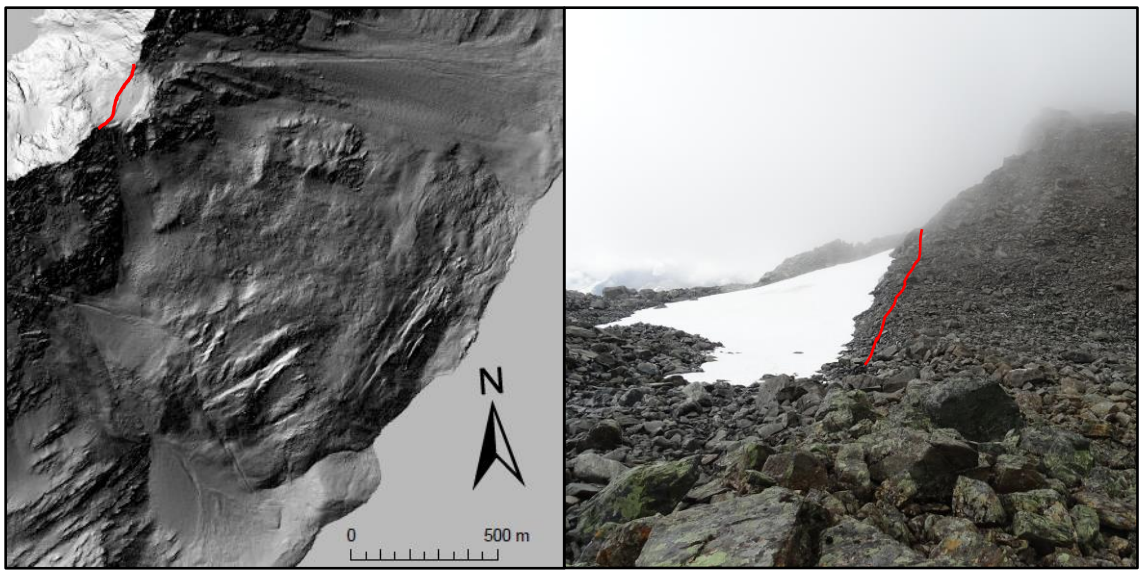

Figure 28 Back scarp on the DEM (left) and in the field (right)

Figure 29 Big scarp and counterscarp

Figure 30 In the front left corner: big scarp and counterscarp; in the back right corner: small scarps covered by boulders (Photo taken by NGU 2019)

Figure 31 Southern (left) & northern (right) lateral boundary(red; inferred limit: dotted line) with debris flow tracks (Photo to the left taken by NGU 2019)

4.3 Structural measurements/foliation/joint sets

In total, 135 foliation measurements and 266 fracture plane measurements were taken. To analyse and present the data, a lower hemisphere, polar, equal area projection was used with a pole vector as plot mode. The treated data is displayed in Figure 32, with the error margin in Table 1 and the mean set planes in Table 2. The raw data can be found in the Appendix p.IX-XV.

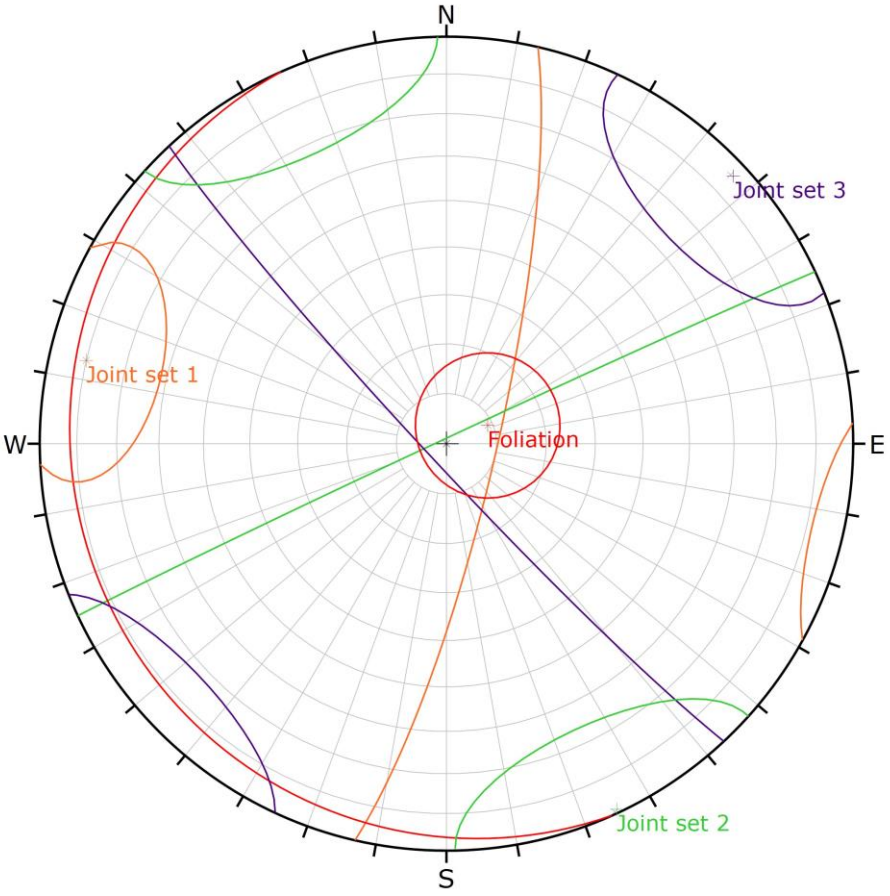

Figure 32 Foliation and joint sets displayed with one STDV

Set	Poles	1 STDV (68.26%)
Joint-set 1	65	18.68°
Joint-set 2	85	23.43°
Joint-set 3	33	21.04°
Foliation	103	13.99°

Table 1 Number of poles and the error margin; The number of poles indicates the number of measurements in the joint or foliation set

Mean set planes	Dip [°]	Dip Direction [°]
Joint-set 1	80	103
Joint-set 2	89	335
Joint-set 3	87	228
Foliation	9	254

Table 2 Mean set planes of the foliation and joint sets.

4.3.1 Foliation

As mentioned above, there are only a few outcrops where both schistosity generations S1 and S2 were observed in the field. The schistosity that is observable in all outcrops is S1. This is, therefore, also the one that was measured. Mica minerals form the S1 schistosity (Figure 33), and it varies from outcrop to outcrop as to how well it is expressed. The mean foliation set plane is oriented 254°/09° (Figure 33).

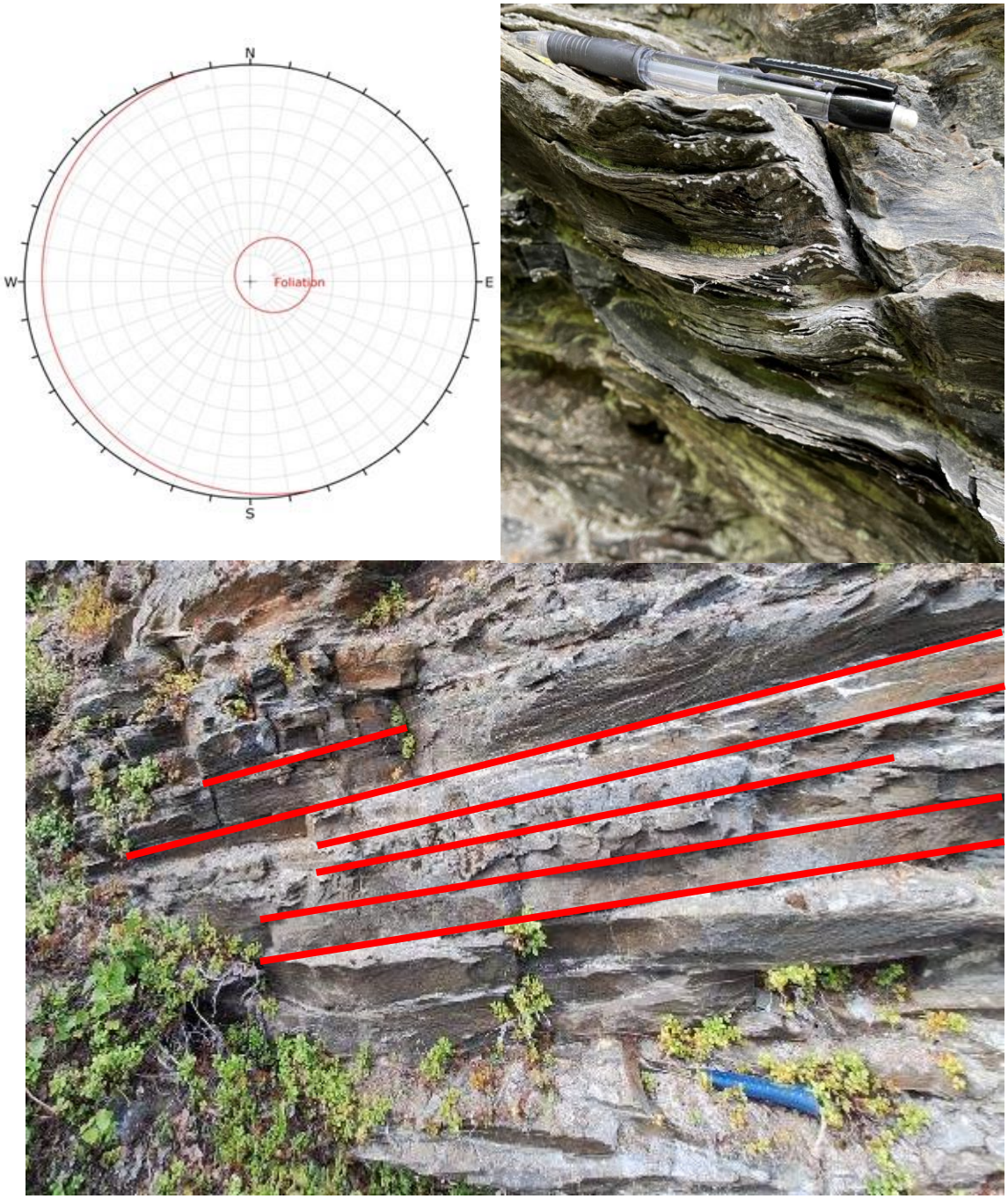

Figure 33 Foliation set projection; Foliation expressed in the field (picture top right taken by NGU 14/08/23)

4.3.2 Joint sets

At Sieidi, three joint sets are observed (Figure 34). Joint set 1 (orange) dips at 80° to the west (103°). The other two sets are considered to be conjugate. Joint set 2 (green) dips NNE (335§) at 89°, whereas joint set 3 (purple) strikes 87° to the SE (228°). These conjugate joint sets are best observed at locations 10-16 (Figure 36, Figure 37, Figure 38), excluding location 14. The joint set 1 is easily recognisable at the locations (Figure 20) 1, 3, 5, 7 (Figure 35), 11, 12 and 14-17 (Figure 38). With regard to the dip direction, sets 1 and 2 are oblique to the foliation compared to joint set 3, which is roughly parallel. Since all the fracture planes dip very steeply, the joint sets comprise areas on opposite sides of the stereonet. Some examples of how the joint sets are represented in the field are shown in Figure 35 to Figure 38.

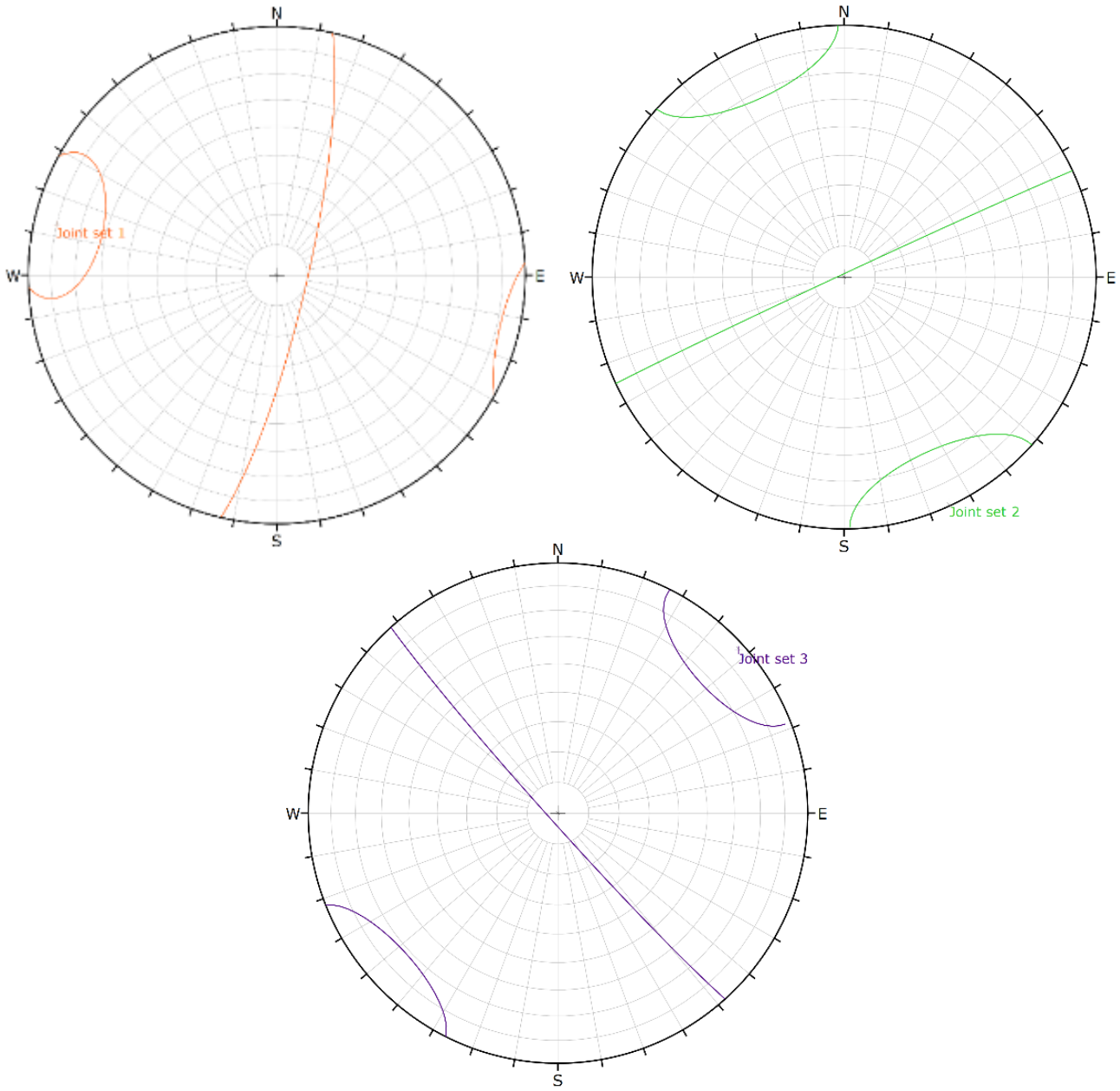

Figure 34 Joint sets 1-3

Figure 35 Joint set 1 (orange) & 2 (green) at location 7

Not all locations showed the same joint sets equally well. In some locations, it was only possible to measure some sets since it was too dangerous or inaccessible to measure with the compass.

Around location 10, joint sets 2 and 3 became more pronounced in the rock mass. They were also even observable by looking at outcrops further away, showing similar structures as seen in Figure 37. In certain locations, all three joint sets could be clearly observed and measured. However, the sets are never equally represented at any outcrop. Nevertheless, the joint sets present are similar, whether on the bottom southern, top southern, bottom northern, or top northern side of the Sieidi URS.

Figure 36 Joint set 2 (green) & 3 (purple) at location 10

Figure 37 Joint set 2 (green) & 3 (purple) at location 13

Figure 38 Joint set 1 (orange), 2 (green) & 3 (purple) at location 16

4.4 Thin sections

The goal of microstructural analysis with the microscope was to determine the degree to which brittle fractures utilise inherent weaknesses in the rock at a microscopic level and to identify the nature of those. The samples for the thin sections were collected both within and outside the URS, with an emphasis on obtaining samples that are representative of the area. One of the blocks for the thin section from locations 4, 8 and 14 fell apart during the preparation and had to be glued together along the fracture plane in the laboratory. The scale in the bottom right corner of the thin section photographs represents 250 µm.

All the observations made by analysing the thin sections are summarised in Table 3. Two different generations of schistosity are observed in certain thin sections, as was expected after field observations (Figure 26). Schistosity generation S1 is always perpendicular to the orientation and shows a phillitic schistosity. The second generation S2 is expressed as a crenulation schistosity parallel to the orientation (Figure 39 to Figure 41).

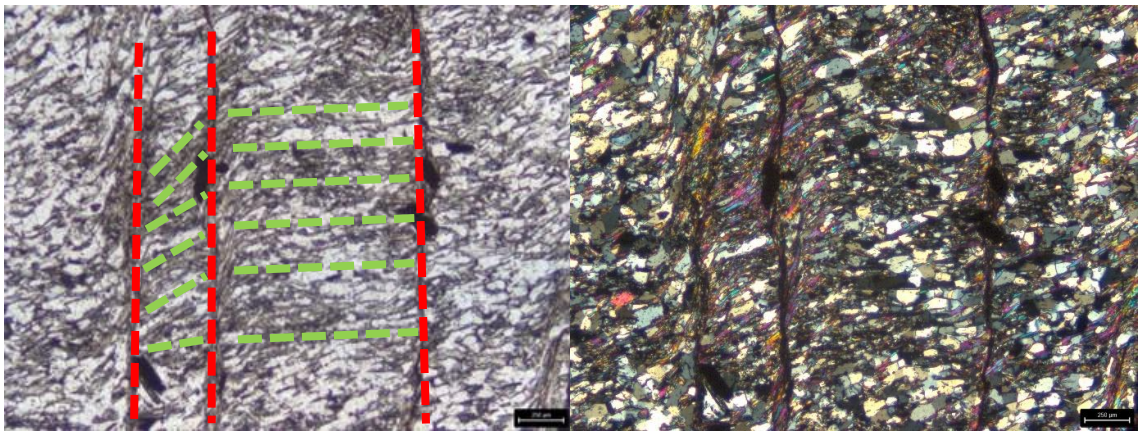

Figure 39 Thin section from location 4, showing S1 (green) and S2 (red) in PPL on the left and in XPL on the right.

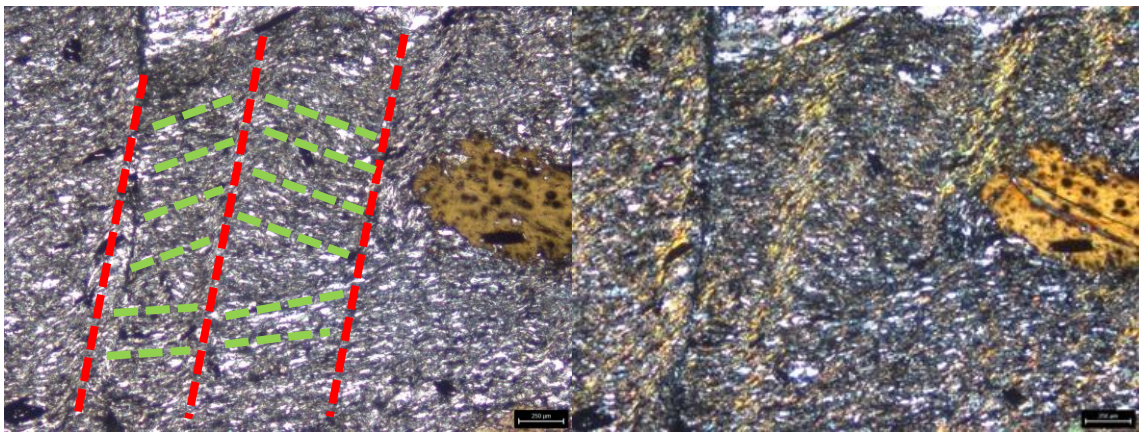

Figure 40 Thin section from location 12, showing S1 (green) and S2 (red) in PPL on the left and in XPL on the right.

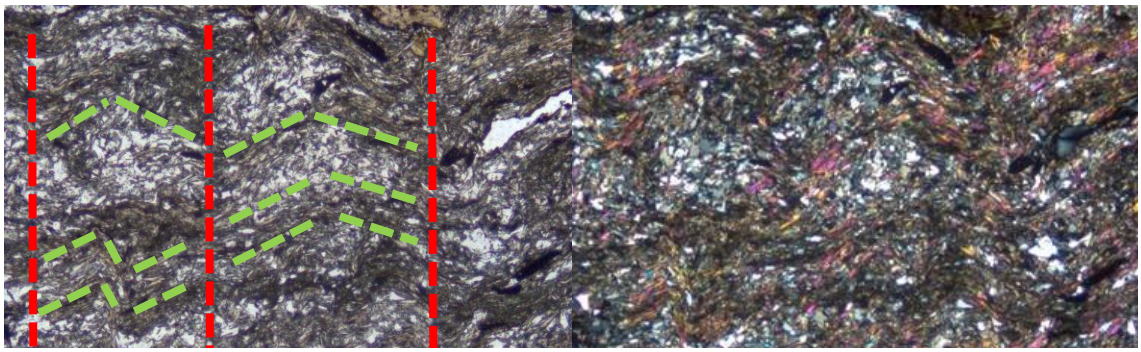

Figure 41 Thin section from location 13, showing S1 (green) and S2 (red) in PPL on the left and in XPL on the right.

In the thin sections 8-10 and 15 (Figure 20), an S-C fabric is observable (Figure 42). These are not regarded as S2 because the S-surface has not finalised the crenulation process, meaning it represents an earlier stage in the deformation process. There are often fractures along the C-surfaces, as seen in Figure 42. The direction of the S-surfaces changes between the surfaces, indicating a change in shear direction/ stress.

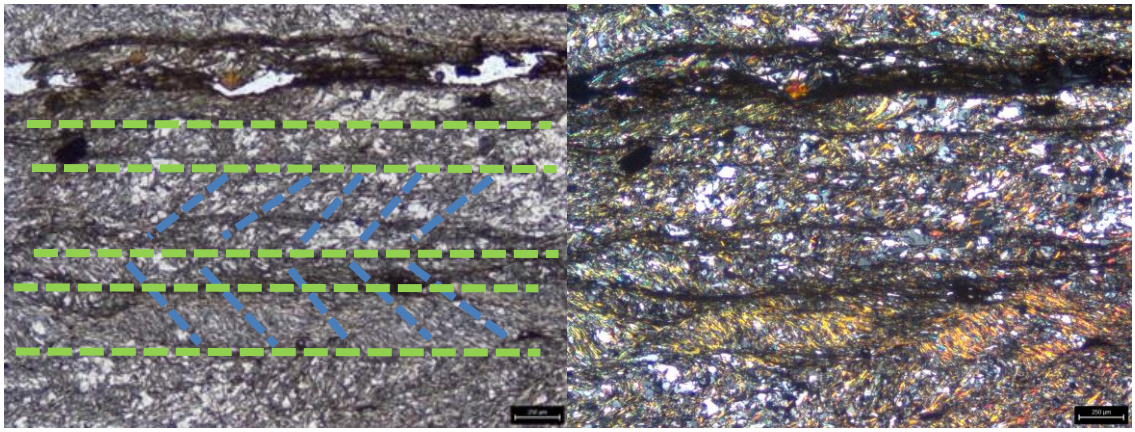

Figure 42 Thin section from location 9, showing S1 (green) and S-C fabric (blue) in PPL on the left and in XPL on the right.

The fractures always occur along the schistosity and mostly along S1. Most of them are, therefore, perpendicular to the orientation (Table 3). The fractures are mainly along the muscovite grains but also occur along the chlorite grains and rarely along the biotite grains. The minerals mentioned in Table 3 are listed in the order of importance along which the fractures occur. The abundance of the present fractures in each sample varies greatly and is grouped into: Abundant (Ab.), Common (Co.), Frequent (Fr.), Occasional (Oc) and Rare (Ra). The scale is relative and not absolute because the thin sections only represent a minuscule part of the outcrop where the sample was collected. Some samples show fractures that have been refilled by quartz minerals, and those fractures were not considered for the classification mentioned above.

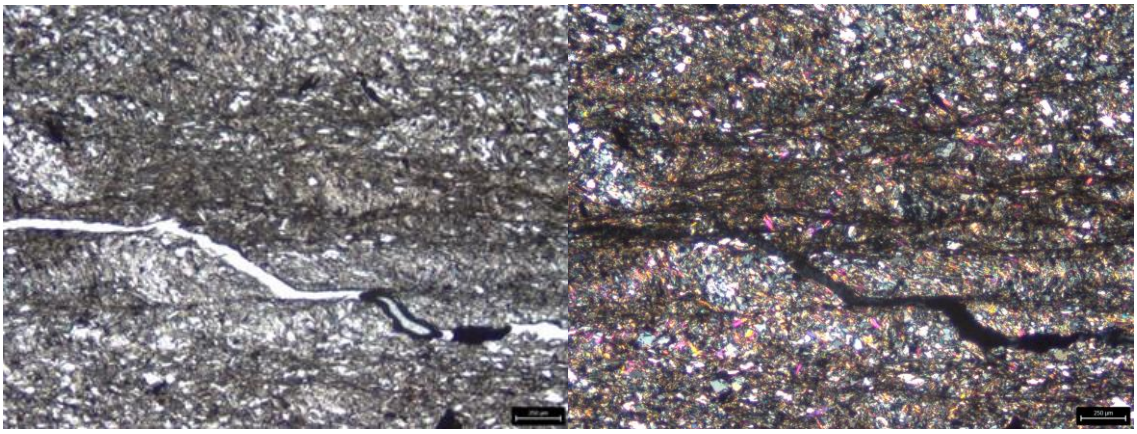

Figure 43 Thin section from location 8, showing S1, S-C fabric and a stepped fracture in PPL on the left and in XPL on the right.

The thin sections from the moving part show a mineral composition similar to the samples from locations 6 and 8. The orientation of the foliation and fractures is the same as well. The only observable difference is the abundance of fractures, which is higher in the samples from the stable part (Table 3).

In the thin section taken from location 8, an example of a shear-dominant stepped fracture is observable (Figure 43). The fracture follows the S-surface and the C-surface (shear plane) along the foliation, showing how different fractures along S1 can be connected, forming one long fracture. Similar stepped fractures can also be observed but on a scale of one magnitude bigger, as seen in Figure 44.

Figure 44 Stepped fracture in a phyllite.

Location	Mineral assemblage (modal %)	Grain size	Schistosity	Fracture orientation	Fracture abundance	Fracture favouring	Comments
3	Quartz: 45 Muscovite: 35 Chlorite: 20	F to C F to C F to M	S1 ⊥ S2 -	⊥	Fr.	S1 ms, chl	
4	Quartz: 45 Muscovite: 25 Chlorite: 30	F to M F VF to M	S1 ⊥ S2 II	II	Co.	S2 ms	S1&S2 visible with the naked eye
5	Quartz: 40 Muscovite: 25 Chlorite: 10 Biotite: 25	VF to C VF VF to M F to M	S1 ⊥ S2 -	⊥	Ra.	S1 ms	Fractures filled with qz
6	Quartz: 50 Muscovite: 35 Chlorite: 15	F to C VF to F VF to M	S1 ⊥ S2 -	⊥	Fr.	S1 ms, chl	Fractures filled with qz
8	Quartz: 45 Muscovite: 35 Chlorite: 20	VF to F VF to F VF to F	S1 ⊥ S2 -	⊥ & II	Ab.	S1 ms, chl	S-C fabric
9	Quartz: 35 Muscovite: 30 Chlorite: 20 Biotite: 15	VF to M VF to F VF C	S1 ⊥ S2 -	⊥	Ab.	S1 ms, chl	S-C fabric
10	Quartz: 40 Muscovite: 35 Chlorite: 15 Biotite: 10	VF to F VF to F VF to M M to C	S1 ⊥ S2 -	⊥	Co.	S1 ms	S-C fabric
11	Quartz: 40 Muscovite: 25 Chlorite: 20 Biotite: 15	VF to M VF to M VF to F M to C	S1 ⊥ S2 -	⊥	Co.	S1 ms, chl	
12	Quartz: 35 Muscovite: 25 Chlorite: 20 Biotite: 20	S to M VF to F VF to F M to C	S1 ⊥ S2 II	⊥ & II	Fr.	S1&S2 ms, chl, bt	Crenulation schistosity
13	Quartz: 45 Muscovite: 20 Chlorite: 20 Biotite: 15	F VF to M VF to M F to C	S1 ⊥ S2 II	⊥	Oc.	S1 chl	Crenulation schistosity
14	Quartz: 35 Muscovite: 55 Chlorite: 10	VF to M VF to F VF	S1 ⊥ S2 II	⊥	Co.	S1 ms	S2 λ on cm scale
15	Quartz: 40 Muscovite: 30 Chlorite: 20 Biotite: 10	VF to M VF to F VF to F VF to F	S1 ⊥ S2 -	⊥	Oc.	S1 ms, (chl)	S-C fabric
16	Quartz: 45 Muscovite: 30 Chlorite: 20 Biotite: 5	VF to M VF to M VF to F VF to F	S1 ⊥ S2 -	⊥	Ra.	S1 ms	Fractures filled with qz
17	Quartz: 35 Muscovite: 15 Chlorite: 50	VF VF to M F to C	S1 ⊥ S2 -	⊥	Fr.	S1 chl	
M2	Quartz: 45 Muscovite: 35 Chlorite: 20	VF to F VF to F VF to F	S1 ⊥ S2 -	⊥	Ra.	S1 ms	
M3	Quartz: 45 Muscovite: 40 Chlorite: 15	VF to C F VF to F	S1 ⊥ S2 -	⊥	Oc.	S1 ms, chl	Fractures filled with qz

Table 3 Summary of the thin sections analysed of the sample at each given location; Modal mineralogy in percentage; Grain size: very fine (VF), fine (F), medium (M), coarse (C); Schistosity: generation 1 (S1), generation 2 (S2), Fracture orientation: perpendicular (⊥), parallel (II); Fracture abundance: Abundant (Ab), Common (Co.), Frequent (Fr.), Occasional (Oc) and Rare (Ra); Fracture favouring: along which schistosity and which mineral, muscovite (ms) or chlorite (chl)

4.5 InSAR

NORCE provided the processed InSAR data, velocity plots, and vector profiles. To calculate the combined 2D InSAR data, the following two data sets were used from Sentinel 1 between the period 2019-2023: Ascending 2 (A2-6-160) and Descending 1 (D1-4-095).

The resulting displacement rates (Figure 45) are presented with a colour code where red indicates movements of more than 20mm/a, orange 15-20mm/a, dark yellow 10-15mm/a, light yellow 5-10mm/a, light green 1-5mm/a and dark green 0-1mm/a (stable bedrock).

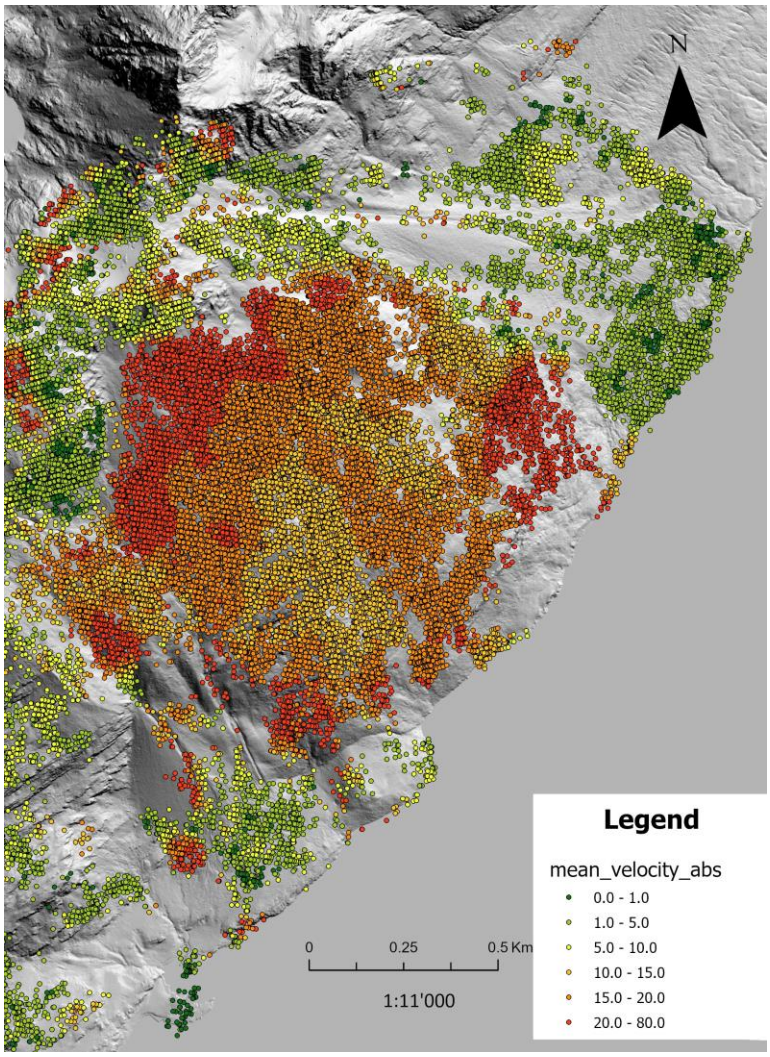

Figure 45 The combined absolute velocity, in mm/a

The data shows the highest movement rates in areas of higher altitudes and in the lower northern parts. In these regions, the displacement is greater than 20mm/a. The displacement of the uppermost block is the lowest, with around 5mm/a. In the southern central half, the movement is the second lowest, with up to 15mm/a. In the northern central half, it is slightly bigger, with up to 20mm/a. There are only a few measurements from the backscarp area because it is covered by snow and ice for the largest part of the year. Moreover, the vegetated

areas show fewer data points than the areas with no vegetation. Nevertheless, this is compensated if zoomed out to get an understanding of a bigger area.

Vector profiles (Figure 47) were made along the sections indicated in Figure 46. Different profiles were chosen to analyse the whole slope and see eventual changes in various areas.

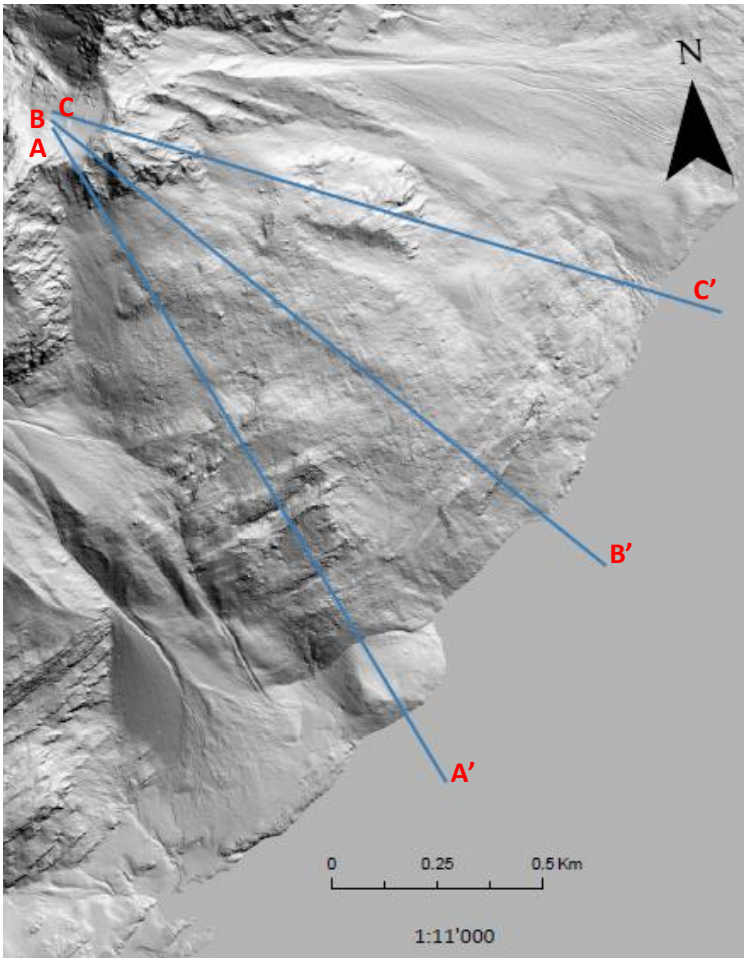

Figure 46 Location of the cross section profiles A-A', B-B' and C-C'

The profiles show a shift in direction between the head domain and the toe area (Figure 47). It shifts in all three profiles from a steep, vertically controlled (joint sets) to a more flat, horizontally (schistosity) controlled displacement. In certain areas, mainly in the top area of C-C', it was not possible to get combined data due to a data hole.

In the section between 250-500m along profile A-A', there are large, nearly vertical vectors displayed, which could indicate the presence of ice. The seasonal melt would explain the vertical displacement vectors. In the areas where the vectors follow the profile with a significant displacement rate, it depicts surface movement and not the slope movement, e.g. B-B' 1000-1200m. Where the vegetation is too dense, and the original InSAR data would require more data points, it is not possible to generate a combined 2D InSAR data coverage. This is the main reason

for blank spots in the data coverage. In Figure 48 these blank spots are represented as a dashed line.

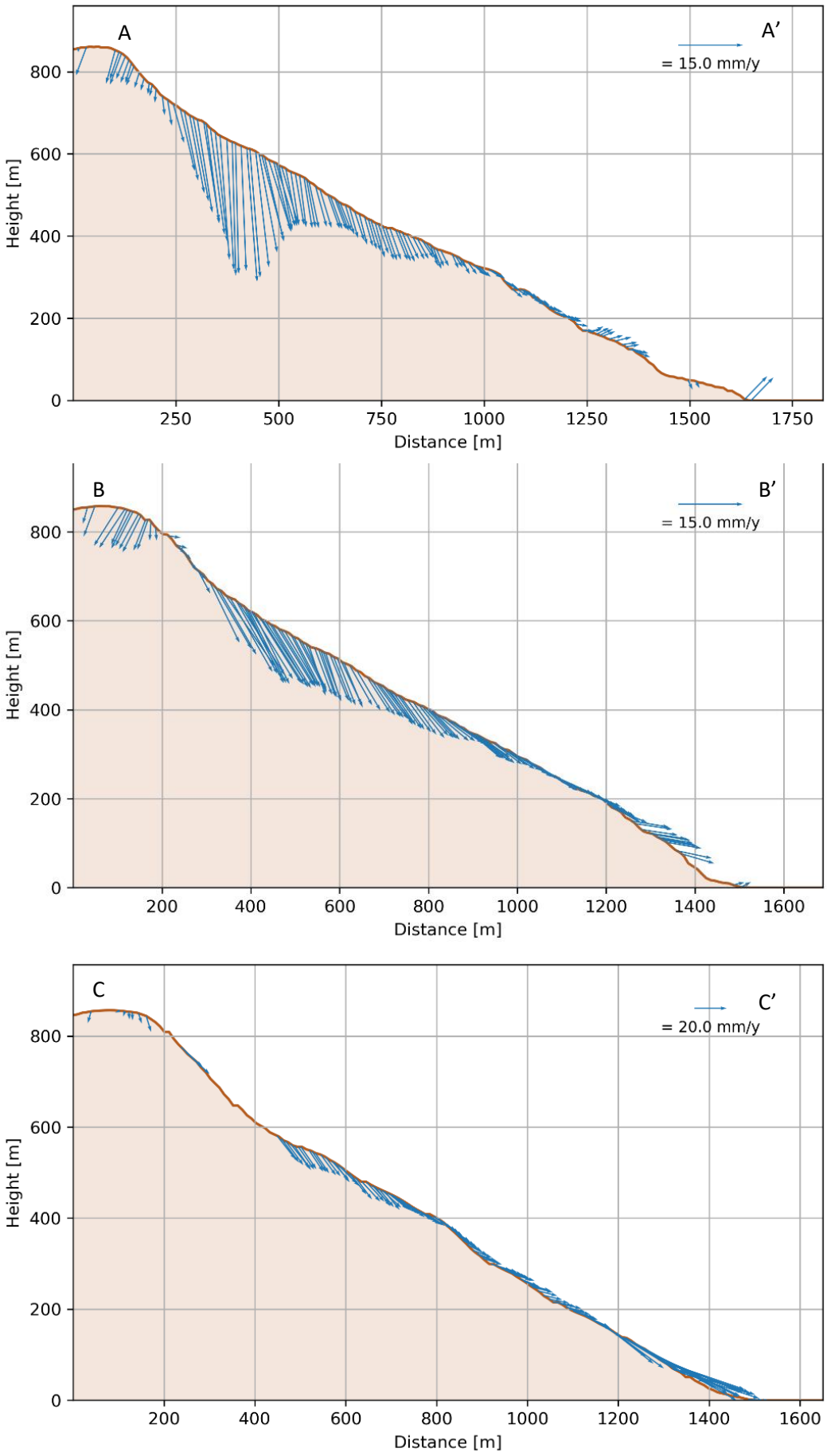

Figure 47 Vector profiles A-A', B-B', C-C'; NORCE

Furthermore, velocity profiles were made along the same profiles as indicated in Figure 46.

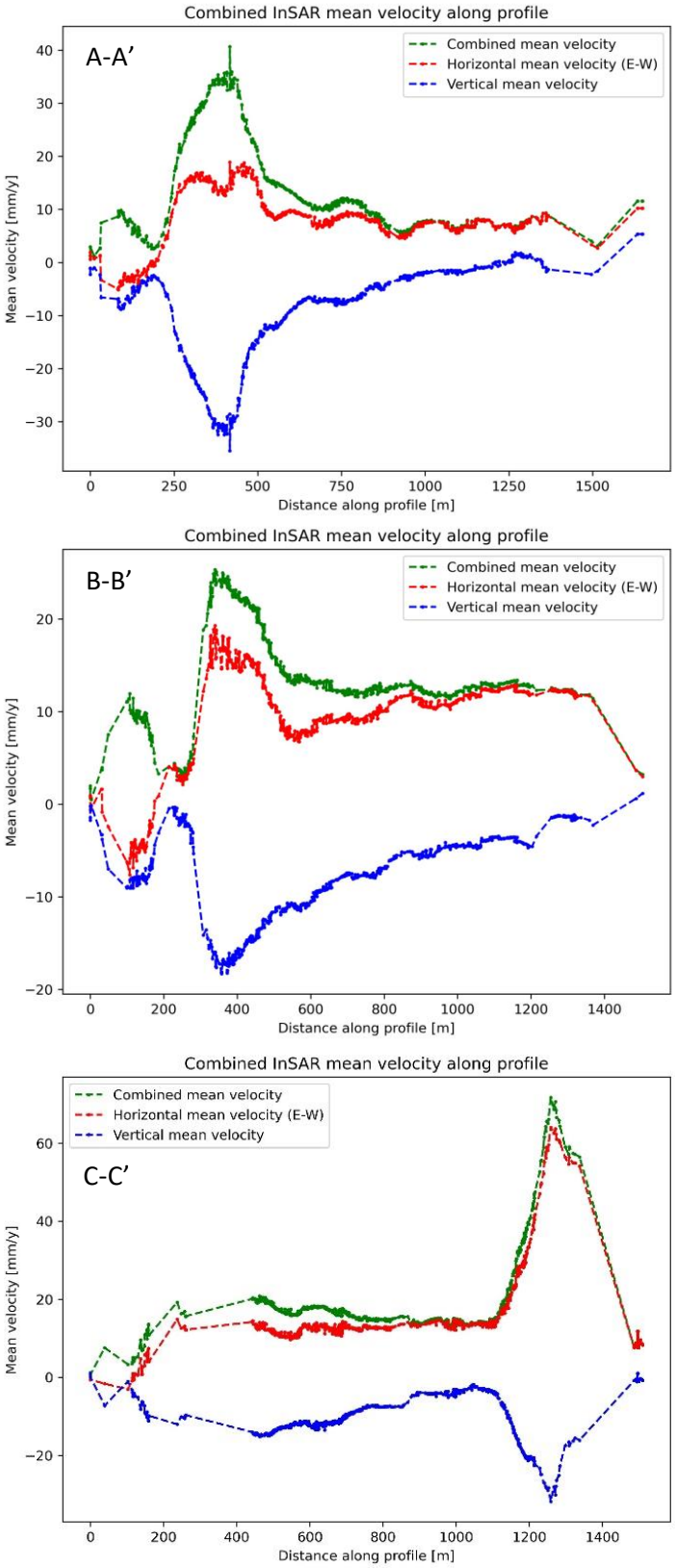

Figure 48 Velocity profiles A-A', B-B', C-C', showing the mean E-W velocity (red), the mean vertical velocity (blue) and the combined velocity (green); NORCE

The velocity profiles along A-A’ and B-B’ share a resemblance, with the combined velocity increasing before it drops slightly, indicating the uppermost block. After the drop, it increases greatly, followed by a short-lived rapid decrease before slowing down until reaching zero. The profile along C-C’ shows a lack of data until roughly 400m. Then, the combined velocity slowly decreases until it augments briskly around 1100m until it decreases just as fast towards the end of the slope.

5 Discussion

Discontinuities such as foliation planes, faults, or joints are essential factors in the failure of soils and rock slopes. These pre-existing structures play a crucial role in the formation and control of instabilities since they are considered to favour weaknesses in the rock mass to propagate (Einstein et al., 1983; Panazzolo & da Silva, 2017; Saintot et al., 2011). Most failures on steep slopes show brittle behaviour and structures aligning favourably to the orientation of the slope that greatly influence the slope stability (Paronuzzi et al., 2015; Saintot et al., 2011). Brittle faulting has been identified as a controlling factor for geometry in URS worldwide (Ambrosi & Crosta, 2006; Bois et al., 2008). The density of brittle structures influences the proneness of failure of URS since it influences the rock mass strength (Brideau et al., 2009; Stead & Wolter, 2015). Tectonic deformation caused the formation of the observable foliation through a ductile deformation process. This schistosity is defined as a continuous, sub-planar rock fabric expressed by the orientation of minerals (Allaby, 2020). Thus, it has an anisotropic effect on the rock strength and controls slope stability if oriented favourably for failure (Vick et al., 2020). Hence, it is significant to investigate the style and degree of anisotropy of the rock while studying unstable rock slopes. It is, therefore, crucial to analyse and understand the relation of all these structural discontinuities in an unstable rock slope. Moreover, these internal structures give essential information about the geological history of a particular rock and controlling factors regarding the geometry and development of a URS.

All the structural and morphological analysis results, 2D InSAR data, thin section observations generated in this thesis, as well as previously available data, are used to investigate the Sieidi URS's slope deformation. This multidisciplinary approach permits to analyse the deformation of the rock slope in comparison to the stable rock and to assess the degree of control lithology and bedrock structure have on the deformation by evaluating how and which structural parameters influence the stability of the rock slope. Lastly, an interpretation of the underlying geometry and kinematics and their influence on the deformation patterns of the Sieidi rock slop deformation is presented.

5.1 Morphological mapping

The morphological map provides a visual representation of the slope deformation, the spatial distribution of the landslide features and the type of surface rock. This is important in order to interpret the InSAR results accurately and ensure that the structural measurements reflect the stable bedrock structures. Furthermore, it guarantees that the samples taken represent the area and altitude from where they were sampled. Those samples and field observations did not

identify a distinct boundaries between different lithologies but instead revealed a gradual transition from phyllite to schist with higher altitude.

5.2 Lithology

The sample analysis confirmed the assumed mineralogical composition, with quartz being the dominant mineral, followed by muscovite, then chlorite, and the least abundant one is biotite. Biotite is not found in the lower altitudes and the percentage increases towards the top. This indicates that the rock underwent a greenschist facies metamorphism. Because of this gradual change in metamorphic history, it is impossible to determine a boundary between the lithologies. Furthermore, schist and phyllite, being rocks with strong anisotropy, exhibit a positive correlation between their strength and the resistance of the weakness plane to shear failure (Yin et al., 2019). Consequently, as bedrock, mica schist or phyllite are susceptible to undergo URS shear deformation along its foliation. Field and microscopy observations confirm that the foliation represents a continuous weakness plane. The thin sections show a high frequency of microfractures in the rock (Table 3), confirming a high anisotropy and its potential for failure. The fractures propagate along the schistosity planes (S1&S2) on both a macro and micro scale alike. The increased degree of metamorphism with elevation presents a fabric less prone to layering, suggesting decreased weakness at the micro scale in higher altitudes in the URS (e.g.Carter & Marinos (2020); Özbek et al. (2018)). Yet, to verify this, further strength testing would be necessary. In addition, various structures resulting from different phases of local tectonic deformation can be identified, such as crenulation schistosity, faults, folds and quartz veins. These structures serve as auxiliary zones of weakness within the URS and have been observed in various locations on both a micro and macro scale.

5.3 Foliation

The Sieidi URS shows a well-developed schistosity (S1) formed by different mica minerals on a macro and micro scale, which dips shallowly into the slope at 254°/09° compared to the slope dipping at 135°/33°. It, therefore, does not dip favourably for being a factor of initiating the instability and for it to be interpreted as a foliation-controlled landslide since the foliation alone cannot form a continuous sliding surface (e.g. after Vick et al., 2020). The fractures mainly occur along S1, i.e., perpendicular to the thin section orientation, indicating that the rock mass resists fracturing perpendicular to the foliation. In some places (Location: 4,12,13 and 14)(Figure 20), the second generation of schistosity (S2) is observable, whereas, in certain locations (Location: 8,9,10 and 15)(Figure 20), it is not fully developed and only shows an S-C fabric. Both the S and the C planes represent zones of weaknesses along which fractures propagate and become connected, forming step fracturing where the foliation S1 is flat and the S2 or S plane of the S-C

fabric form the step (Figure 49). These fractures result from the degradation of negative rock bridges.

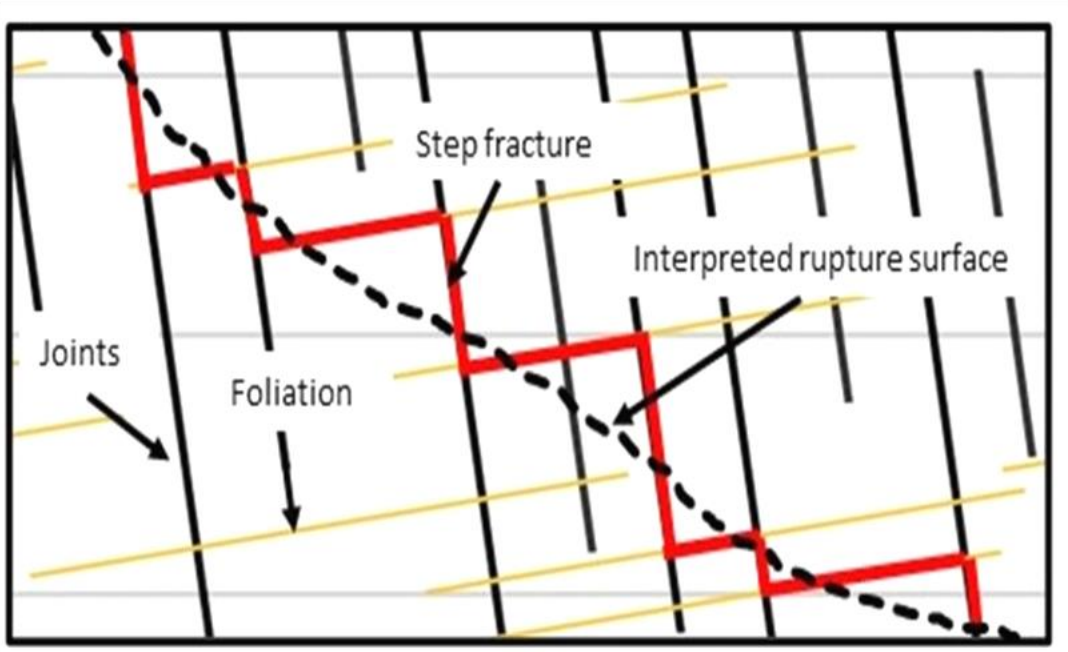

Figure 49 Interpretation of how the basal rupture surface is formed at Sieidi

The failure of the rock between an intricate network pattern of existing joints can manifest as a negative rock bridge. Neglecting the formation of those poses the risk of an incomplete failure analysis since it does not consider the full range of potential failure surfaces. If negative rock bridges are present they augment the resisting forces by enhancing shear resistance and acting as a stabilising factor. This results in failure through a zone of damage within the rock mass and not along a clearly defined surface. Moreover, negative rock bridges can contribute to the dilation of the rock mass by acting as separation surfaces, thereby augmenting the potential for block failure in terms of kinematics (Elmo et al., 2018). This can explain why there are rather few clearly visible big scarps (only in the southern part) along the slope since more energy is required to break through these negative rock bridges. The average foliation at Sieidi dips 9°into the slope and does not act as the controlling factor for failure. However, the slope inclination is steep enough that it might enable the degradation of rock bridges. This leads to step fractures to occur and a failure surface controlled by fracture planes to arise (Figure 43, Figure 44 and Figure 49).

5.4 Micro cracks

In the thin sections presented in this thesis, microcrack orientations frequently align with the mineral along the crystal and schistosity planes or even follow their boundaries exactly. This suggests that the crystallographically preferred orientation functions as a plane of weakness, influencing the fracture propagation trajectory (e.g. after Rigopoulos et al., 2013). Microcracks manifest as fracture zones comprising interconnected and separate microcracks, leading to a

more disorderly and broader fracture zone. Consequently, the degree of metamorphism and the subsequent alteration in mechanical properties influence the quantity of isolated and interconnected microfractures.

According to Kranz (1983), fractures occurring under compressive loading are not caused by the growth of a single crack but by coalescence and interaction with several microcracks. This implies that certain pre-existing isolated microcracks within and between grains may propagate and eventually connect during loading. This in turn leads to macro fracturing, as well as a decrease in the overall sum of microcracks, yet an increase in the length of the ensuing fracture (Rigopoulos et al., 2013). Furthermore, the thin sections within the URS show fewer micro fractures. This could be because the dislocated block already underwent failure and the stress exerted on it decreased thereafter.

5.5 Joint sets

Joint sets are a type of discontinuity, as mentioned earlier, thus rendering them essential to the understanding of the rupture and failure processes of landslides because the physical properties and brittle behaviour of fracture planes are critical for the development of instabilities. If the spatial orientation of joints is aligned with the one from observed morphological features, it indicates that the features might be controlled by the joint planes. The joint sets (J1, J2 and J3) are homogenously distributed throughout the URS. However, certain joint sets are better presented in certain locations than others, making it necessary not to neglect observation and measurement biases during the data acquisition. The three joint sets all dip very steeply, meaning that the direction in which the joint planes dip becomes less important, whereas the line of strike of the plane (dip direction ± 90°) better represents their significance. Joint set 1 (103°/80°) dips roughly perpendicularly and strikes subparallel to the backscarp (NNE-SSW) and, therefore, strikes perpendicularly to the slope direction (135°/33°). Joint set 2 (335°/89°) is subparallel to the major scarps in the southern part of the slope (striking NNE-SSW), and joint set 3 (228°/87°) strikes perpendicularly to the backscarp and the mountain ridge (both striking NNE-SSW). The latter two joint sets are very well defined at an altitude of 400 masl. or higher. Since all the thin sections were cut perpendicularly to the foliation, it is not possible to distinguish the joint sets under the microscope as they dip very steeply and the dip direction is unknown of the joins in the thin sections.

5.6 InSAR

The InSAR data show velocity values ranging from minimal (< 2.0 mm/a) or modest (2.0–5 mm/a) in the northwestern regions, close to the uppermost block, to 15–20 mm/a or even more in the

central or northwestern areas. However, the most compelling movements are due to continuous surface dynamics, and in the bottom part of the northwestern area, it could be due to the presence of a small rock glacier or bigger volumes of ice since they show the highest values primarily representing vertical movement hinting to the melting of ice (Delaloye & Echelard, 2021; Liu et al., 2013). In addition, the lateral boundaries of the URS observed in the field are supported by InSAR data showing an abrupt decrease in displacement rates.

Furthermore, instabilities have the potential to be internally segmented due to differences in movement direction and deformation velocity (e.g., Dahle et al., 2008; Blikra et al., 2009). Thus, profile sections (A-A', B-B', C-C') were made along different areas of the slope (Figure 46).

By comparing the velocity profiles against the model profiles presented by Frattini et al. (2018), it is interpreted that the profiles A-A' and B-B' show similar markers to a rototranslational plastic slide (Figure 10) after accounting for data holes. The total displacement shows a double peak before it decreases, and the vertical displacement shows the opposite with a double depression before it increases gradually. The velocity profile C-C' is more challenging to interpret as there is a larger lack of data close to the backscarp, the uppermost block and the toe domain. Nevertheless, the data available shows similarities with the signature of a translational slide. It displays a stable vertical movement in the central part along the profile with a dip towards the end before it increases to zero movement. This is a typical signature for a translational landslide.

Despite having areas lacking data or showing movement not related to the slope deformation, the vector profiles show similar indications regarding the gliding surface. Therefore, it is proposed that the Sieidi URS has a translational basal rupture surface, which changes geometry slightly by a rotational component from north to south. The rotational component does not display true rotational geometry; instead, it follows step-fractures connecting the joint planes and the foliation. In this scenario, it takes on a more listric shape with depth as the dip of the rupture surface lessens (e.g. after Stead & Eberhardt (2013) and Vick et al. (2020)).

The method proposed by Intrieri et al. (2020) to determine the geometry of the basal failure surface does not produce satisfactory results for several reasons. Firstly, there are large areas without enough data, in particular the backscarp region (see section 3.4). Secondly, the exaggeration of the displacement vectors caused by the proposed ice volume in the NE part below the displaced block need to be ignored (Figure 45). Thirdly, the vectors indicating surface displacement must be neglected for the interpretation. Despite these restrictions, it provides an idea of the geometry, and it was applied using the displacement vector profile B-B', as it is the least affected by the restrictions mentioned. However, the first usable vector was below the

uppermost block. The results are shown in Figure 50. (The original can be found in the Appendix p.XVI.)

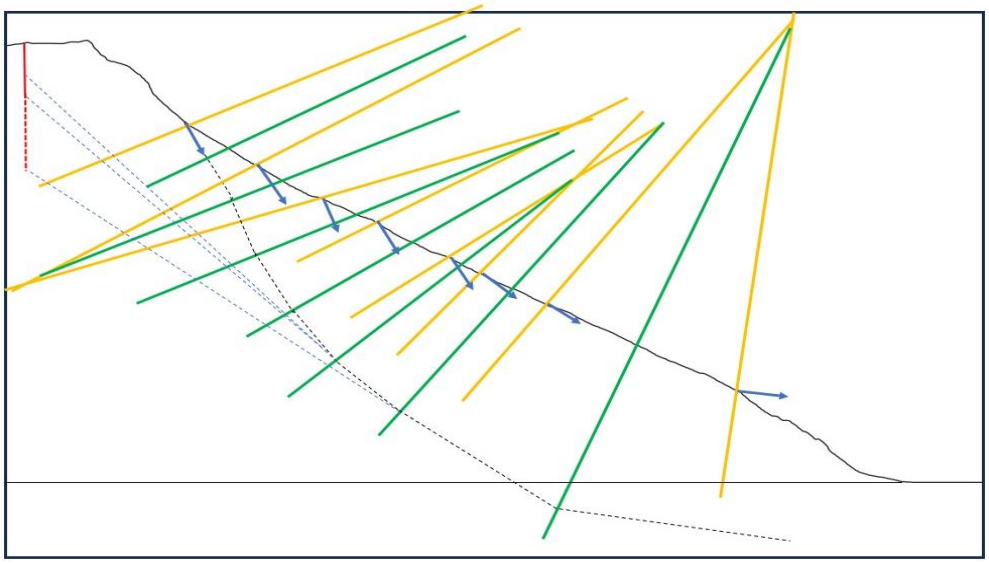

Figure 50 Graphical method to interpret the geometry and depth of the basal rupture surface (dotted line); normal line (yellow), bisection line (green), displacement vectiors (blue), possible rupture surface for the area without data (dotted blue line), back ruptur surface (red), possible back rupture surface (dotted red line)

5.7 Geological model

A kinematic interpretation of the slope is possible by combining displacement measurements, using 2D InSAR, mapped morphological features, as well as structural measurements. Three cross section profiles illustrate the dynamics of the Sieidi URS (Figure 51-Figure 53). The indicated foliation and joints are representative and adjusted to the apparent dip, while the colour code represents the gradual change from phyllite at the bottom to schist at the top. Moreover, the suggested rupture surface is drawn after compiling InSAR data structural data and morphological data. Since cross section B-B' shows very little morphological evidence of movement, the results have been interpolated from the other two cross sections. In Troms County, only the Mannfjellet URS is classified as a rotational slide. Therefore, assuming that the Sieidi URS behaves similarly to other landslides in the area in similar rock types and with a comparable geological history, the starting theory was that Sieidi has a translational rupture geometry, too. The geomorphological mapping and InSAR data provide strong evidence that the initial idea is correct. The data suggests the presence of a translational basal rupture surface with a slightly convoluted component close to the back scarp. However, the data does not allow the depth of the rupture surface to be determined. The delineation of the basal rupture surface is challenging as it is based on the absence of a clearly visible daylighting indicator at the surface in the toe domain and due to the lack of vector data at the back scarp to use the method proposed by Intrieri et al. (2020). The resulting rupture surface had to be adapted to fit the

observations and account for the data holes. The depicted depth of the basal rupture surface is, therefore, only an interpretation.

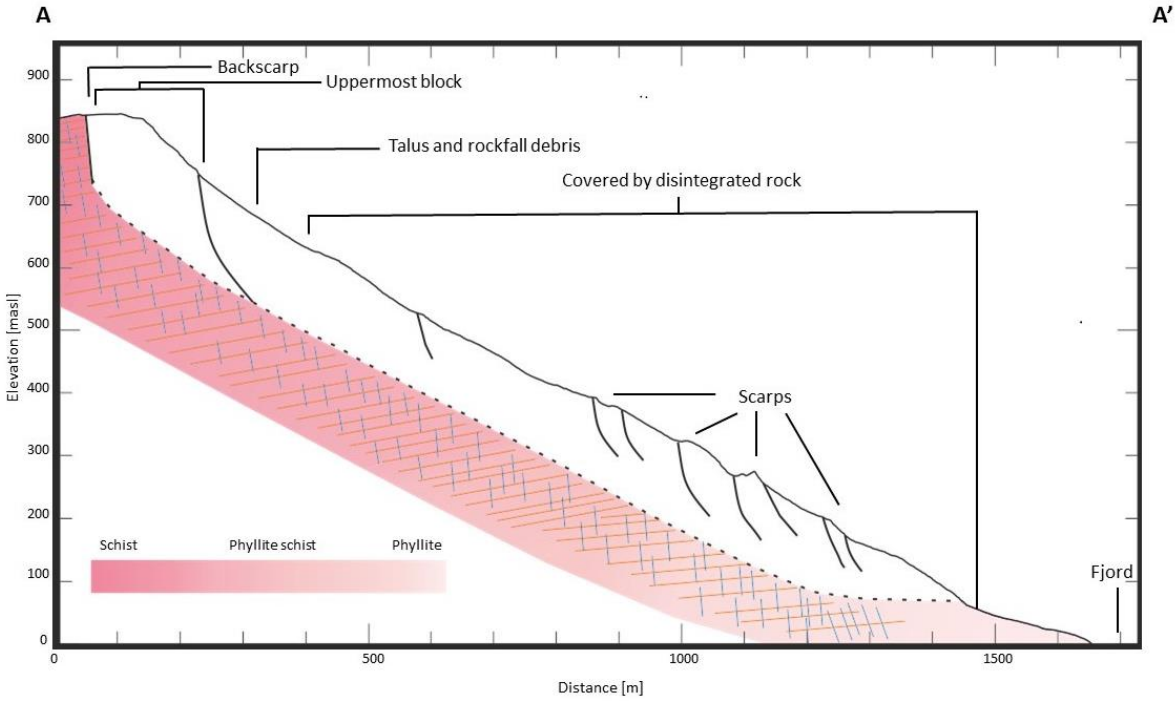

Figure 51 Geological interpretation along cross-section A-A', the foliation is drawn in orange, and the joints are blue in the cross-sections. The other structures are drawn in black and represent the interpreted morphological elements present. The dotted line represents the interpreted rupture surface and is not observable in the field. Drawn with CorelDRAW

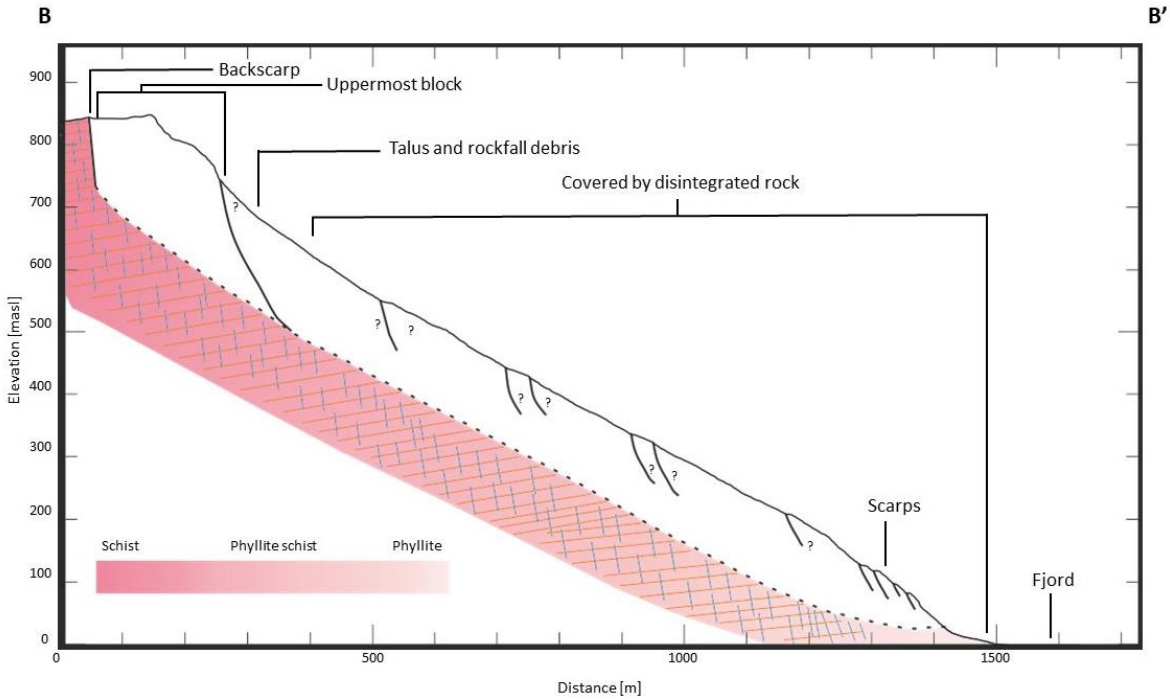

Figure 52 Geological interpretation along cross-section B-B', The elements that are interpolated are marked with a question mark as their presence cannot be confirmed as a cover of disintegrated rock might obstruct them. The foliation is drawn in orange, and the joints are blue in the cross-sections. The other structures are drawn in black and represent the interpreted morphological elements present. The dotted line represents the interpreted rupture surface and is not observable in the field. Drawn with CorelDRAW

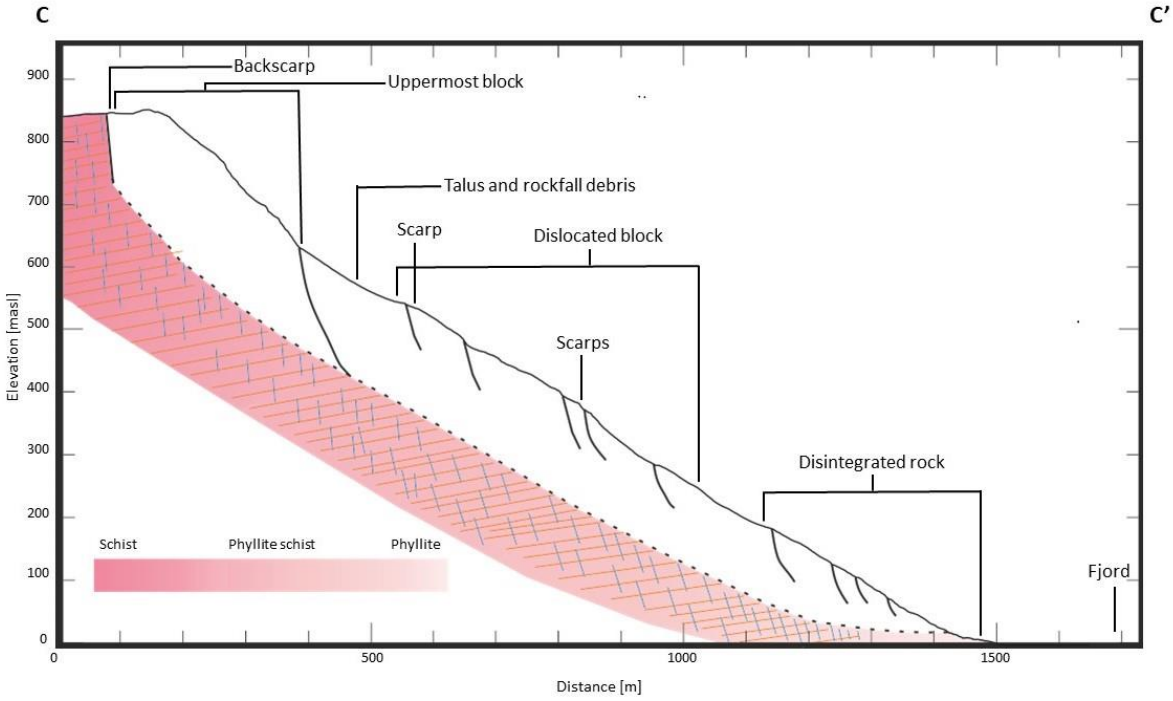

Figure 53 Geological interpretation along cross-section C-C', foliation is drawn in orange, and the joints are blue in the cross-sections. The other structures are drawn in black and represent the interpreted morphological elements present. The dotted line represents the interpreted rupture surface and is not observable in the field. Drawn with CorelDRAW

The study suggests that the current rupture along the backscarp occurs following the steep joint set 1. The extent to which the rear rupture conforms to joint set 1, however, remains uncertain because it is impossible to verify it within the rock mass. At the SE end of the back scarp, it changes slightly in direction and strikes in the same direction as a joint set 2. Given the steep nature of the joint set surface compared to the postulated basal rupture surface, it necessitates a transfer to the low-angled basal rupture surface since high-angled joints cannot daylight at the surface. Consequently, it remains uncertain to what extent the rear rupture surface persists at a deeper level, making it impossible to determine the transfer zone (e.g. after (Vick et al., 2020). Subsequently, the rear rupture must transition to a basal rupture at a lower point on the slope, likely following the foliation and joint sets along step fractures.

It is believed that the scarps observed are formed along joint set 2 since they are all aligned roughly in the same direction. As the joint sets dip steeply and are spatially well distributed, indicating their well-developed network of ruptures and role as rupture areas, they are believed to have significantly impacted the structural integrity of the rock mass present, thereby lowering the slope strength.

5.8 Hazard classification

In order to put the observations and interpretations of this study into context for society, the results are used to complete the hazard classification system implemented by NGU (R. Hermanns et al., 2012). It consists of nine categories corresponding to the slope's potential failure (Table 4). Each criterion is given a number of points to quantify them. The assigned points are individually explained and stated.

Backscarp

The backscarp is covered by disintegrated rock but is easily recognisable on the 1m DEM. The backscarp gets 0.5 point for a poorly developed backscarp.

Potential sliding structures

The foliation dips on average 9° into the slope, meaning it is not a potential failure surface. However, joint set 2 dips at 89° and is believed to coincide with the backscarp, representing a potential rupture surface. This criterion has 0.5 point.

Lateral release surfaces

The lateral release surfaces are not fully developed on both sides, giving this criterion 0.5 point.

Kinematic feasibility test

The software Dips allows to conduct basic kinematic analysis. They show that failure is kinematically possible but to a very low extent (Figure 54). This tool provided by Dips is not to be used as a final assessment yet rather to gather an impression of a more complex URS. This criterion was given 0.5 point.

Morphologic expression of the ruptured surface

Deformation is visible by the expression of scarps along the URS. Because it is not expressed equally well considering spatial distribution, only 0.5 point are given here.

Displacement rates

Displacement rates range throughout the slope from <5 mm/year to places with 20 mm/year.

It is to be noted that the InSAR may pick up surface displacement and not only the displacement of the URS. Thus, two points are attributed.

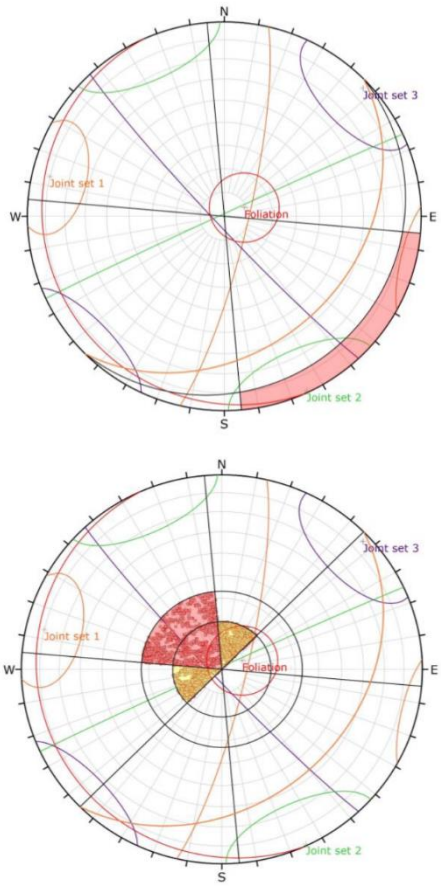

Kinematic Analysis	Flexural Toppling		
Slope Dip	33		
Slope Dip Direction	135		
Friction Angle	20°		
Lateral Limits	40°		
	Critical	Total	%
Flexural Toppling (All)	24	405	5.93%
Flexural Toppling (Set 13: Joint set 1)	6	65	9.23%
Flexural Toppling (Set 14: Joint set 2)	17	86	19.77%

Symbol	Feature
▪	Critical Intersection

Kinematic Analysis	Direct Toppling		
Slope Dip	33		
Slope Dip Direction	135		
Friction Angle	20°		
Lateral Limits	40°		
	Critical	Total	%
Direct Toppling (Intersection)	1454	81808	1.78%
Oblique Toppling (Intersection)	2237	81808	2.73%
Base Plane (All)	58	405	14.32%
Base Plane (Set 16: Foliation)	47	114	41.23%

Figure 54 Kinematic analysis; Top: Flexural toppling, Bottom: Direct toppling; analysis run on Dips

These scores are used to generate a hazard matrix (Table 4). The hazard classification corresponding to the evaluation above falls into the moderate (4.8 to 7.2) category, with calculated minimum, average, and maximum hazard scores of 3.3, 5, and 10, respectively.

	Criterion	Condition	Rating	Score		
				Average	Minimum	Maximum
1	Development of back scarp	Not developed	0	0.50	0.50	1.00
		Partially open over the width of slide body (few cm to m)	0.5			
		Fully open over the entire width of slide body (few cm to m)	1			
2	Potential failure surfaces	No penetrative structures dip out of the slope	0	0.50	0.00	1.00
		Penetrative structure dips on average < 20° or steeper than the slope	0.5			
		Penetrative structure dips on average > 20° and daylights on the slope	1			
3	Development of lateral release surfaces	No lateral surface developed	0	0.50	0.25	0.50
		Lateral surface partly developed on one side	0.25			
		Fully developed or free slope on one side or partly developed on two sides	0.5			
		Fully developed or free on one side and partly developed on one side	0.75			
		Fully developed or free on both sites	1			
4	Kinematic feasibility test	Kinematic feasibility test does not allow for planar sliding, wedge sliding or toppling	0	0.50	0.50	1.00
		Failure is partly kinematically possible (movement direction is more than ±30° to slope orientation)	0.5			
		Failure is kinematically possible (movement direction is less than ±30° to slope orientation)	0.75			
		Failure is partly kinematically possible on persistent discontinuities (movement direction is more than ±30° to slope orientation)	0.75			
		Failure is kinematically possible on persistent discontinuities (movement direction is less than ±30° to slope orientation)	1			
5	Morphologic expression of the basal rupture surface	No indication on slope morphology	0	0.50	0.50	0.50
		Slope morphology suggests formation of a rupture surface (bulging, concavity-convexity, springs)	0.5			
		Continuous rupture surface is suggested by slope morphology and can be mapped out	1			
6	Landslide displacement rates	No significant movement	0	2.00	1.00	3.00
		0.2-0.5 cm/year	1			
		0.5-1 cm/year	2			
		1-4 cm/year	3			
		4-10 cm/year	4			
		> 10 cm/year	5			
7	Acceleration (if velocity is >0.5cm/yr & <10cm/yr)	No acceleration or change in displacement rates Increase in displacement rates	0	0.00	0	1.00
		Increase in displacement rates	1			
8	Increase in rock fall activity on the unstable slope	No increase of rock fall activity	0	0.00	0.00	1.00
		Increase of rock fall activity	1			
9	Presence of post-glacial events along the affected slope & its vicinity	No post glacial events of similar size	0	0.50	0.50	1.00
		One or several events older than 5000 years of similar size	0.5			
		One or several events younger than 5000 years of similar size	1			
Totals			5	5.0	3.3	10.0
Hazard Class				Moderate	Low	Very high

Table 4 Hazard classification;points accredited for each criterion marked in red; modified after Hermanns et al. (2012)

For the consequence assessment (Table 5), it is necessary to quantify the elements at risk. Since the Sieidi URS ends at the fjord, no elements are directly at risk, but people living (13 residential houses) on the opposite side of the fjord are indirectly at risk of getting hit by a displacement wave. This study takes a conservative approach and assumes an average occupancy of 3 residents per house, with a minimum occupancy of 30% and an average of 60%.

For the worst-case scenario, the maximum value for each parameter was chosen, i.e. 100%.

The values for the least disastrous scenario were decided based on a conservative approach. The probability of propagation was set at 20% because the Sieidi RSD is distributed over a larger distance, and it is possible that the southern part does not fail when the middle or northern part fail. For the probability of presence, 30% was chosen since this equals roughly 8 hours, marking the time the inhabitants sleep and assuming they are not at home for the rest of the day.

For the average scenario, the probability of propagation was set at 40% because it does not behave linearly, and a reduced propagation is more probable. For the probability of presence, 60% was chosen since this equals roughly 14 hours, giving the inhabitants 9 hours for work and running their errands. For the vulnerability, the chance of surviving if hit is not linear; in that case, most people would die.

Combining the hazard classification and the consequence assessment according to the following equation makes it possible to determine the risk (Figure 55).

$$R = P_F \times P_P \times P_E \times V \times E$$

Figure 55 Risk equation, PF = probability of failure; PP = probability of propagation; PE = probability of presence of the element of risk; V = vulnerability; E = element at risk

Parameter		Probability of Propagation	Probability of Presence	Vulnerability	Element at Risk	Estimated Loss of Life
Average	Value	0.4	0.6	0.95	39	9
	Comment	In a detailed assessment is based on run-out modelling (and displacement wave assessment if relevant); otherwise estimated based on professional judgement and experience	Based on occupancy rate of the building type (house, office, shop, school etc.) or proportion of time to transit the affected area (eg. along a road within the landslide runout zone)	If the building is inundated or collapses then death is almost certain	Number of people living in the village within the runout zone of the landslide	
Maximum	Value	1	1	1	39	39
	Comment	Worst case scenario P_P, P_E and V are set to 1 (as assumed in a preliminary risk assessment to distinguish between low risk objects and medium to high risk objects that require more detailed risk analyses)			Number of people living in the village within the runout zone of the landslide	
Minimum	Value	0.2	0.3	0.9	39	2
	Comment	Best case estimate of P_P, P_E and V			Number of people living in the village within the runout zone of the landslide	

Table 5 Consequence assessment according; modified after Hermanns et al. (2012)

The result (Figure 56) shows that it is clearly below the 1/5000 nominal annual likelihood danger level, which does not necessitate restricting new construction in the area under current Norwegian law (Byggteknisk forskrift (TEK17), 2017). However, the calculated risk is precisely between the safe area and periodic monitoring. Hence, the Sieidi URS should not be forgotten in the future, should be reassessed and the risk assessment adjusted accordingly.

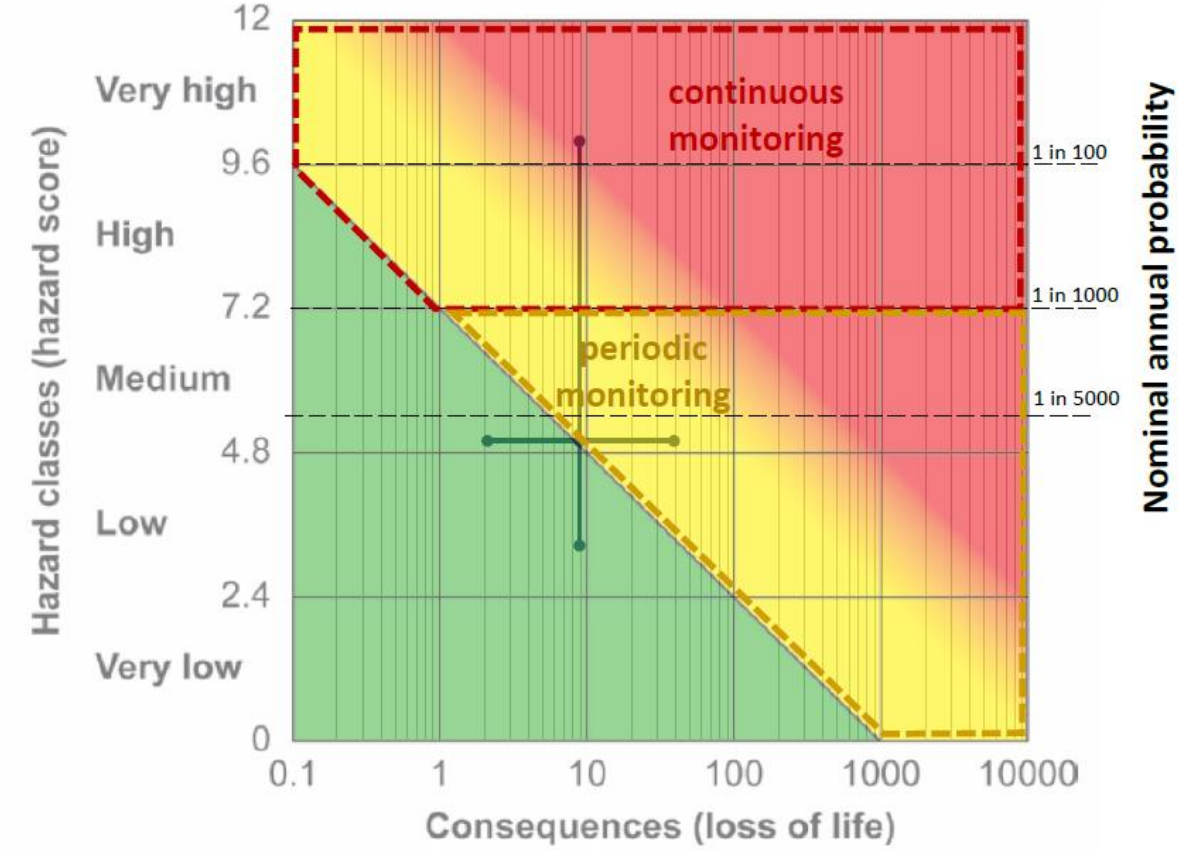

Figure 56 Risk classification matrix for the Sieidi RSD; modified after Hermanns et al. (2012)

6 Conclusion

This thesis presents a comprehensive investigation of kinematics, structural properties, and failure mechanisms of the Sieidi unstable rock slope carried out through a multidisciplinary approach. By integrating field work, structural analysis, morphological mapping, thin section analysis and 2D InSAR data, a model of Seidi, which gives both an insight into the nature of the slope instability and the conjecture of the geometry of the back and basal rupture surfaces, is proposed in order to address the research objectives.

A significant outcome of this study is the production of a detailed morphological map. It shows the spatial distribution and orientation of the scarps and dislocated blocks. In addition, the map visualises that the majority of the slope is covered by disaggregated rock. This map serves as a visual representations, thereby providing a foundation for understanding the research results.

The bedrock at Sieidi is presented as phyllite in the lower altitudes, and with increasing altitude, the metamorphic gradient also increases, and the rock transitions to schist. However, it is impossible to determine an exact line where the lithologies change. The inherent structures in the Seidi unstable rock slope are brittle joints and foliation. The field measurements recorded the average foliation at 254°/9°, Joint set 1 at 103°/80°, Joint set 2 at 335°/89° and Joint set 3 at 228°/87.

Furthermore, microstructural analysis elucidates the role of primarily brittle discontinuities in controlling slope behaviour. The propagation of microfractures along the mica grains and zones of weaknesses within the rock mass contribute to and ultimately lead to the development of the mentioned macro scale joint sets and step fractures. These geological structures suggest a basal rupture surface along step fractures where the foliation S1 is flat and the joint planes the step.

Moreover, the 2D InSAR data highlights that the highest displacement rates (>20mm/a) are in the NW below the uppermost block and in the NE. The middle part of the slope shows displacement rates of 10-20mm/a. The velocity profiles advocate a complex compound sliding mechanism with characteristics of a translational basal rupture surface with a rototranslational component increasing towards the SW.

The gliding surface forms along stepped fractures with a rear rupture controlled by joint set 1. Moreover, joint set 2 controls the formation of the scarps. The identification of slight toe bulge structures and morphological depressions further emphasise the complex nature of the progressive slope deformation processes at Sieidi.

The results show a complex interplay between structural features and deformation patterns within the rock slopes. In particular, the influence on the movement of the foliation dipping into the slope is interesting, with the slope utilising the degradation of negative rock bridges to form a sliding surface with step fractures along the joint sets and foliation surfaces. This is further confirmed by InSAR vector analysis, field observation and thin section analyses, the latter of which accentuates the presence of stepped fractures utilising anisotropic properties and weak shear zones along the different schistosity generations.

Lastly, the importance of this thesis, namely quantifying and thereby minimising the risks posed by the Sieidi unstable rock slope, is highlighted through the application of the established NGU hazard analysis techniques. Despite the classification as a low-risk object the presence of uncertainties highlights the need for sporadic monitoring and further investigation. The integration of different methodologies in rock slope analysis, combining fieldwork, laboratory investigation, and remote sensing techniques, underscores the value of this study in achieving a comprehensive overall understanding of rock slope dynamics. For future research, continued efforts to refine monitoring techniques and further the understanding of slope processes will be critical to effectively managing unstable rocky slopes and ensuring the safety of people and infrastructure at risk.

7 Acknowledgement

First and foremost, I would like to thank Associate Professor Louise Vick, my supervisor, who gave me valuable guidance in the scientific world and always helped me and brought me back on the right track if necessary. Furthermore, I thank Trine Dahl for introducing and supporting me in the laboratory and Prof. Jiri Konopasek for providing me with guidance with the rock saw. In addition, I would like to thank Dr. Martina Böhme, Vanja Skålnes Haugsnes and Marie Bredalfor from NGU for their assistance, feedback and help with fieldwork. I want to thank Dr. Carly Faber for helping me with the interpretation of the thin sections and rock samples.

A special thanks goes to my family and my parents, who supported and accompanied me the whole way. They made it possible in the first place for me to study at the Arctic University of Norway, and I am forever grateful for their help and their support. Last but not least, a big thank you to all my fellow geology Master friends. You are the best, and I will always keep you close in my heart; you made this time truly extraordinary.

8 Bibliography

Agliardi, F., Crosta, G. B., & Frattini, P. (2012). Slow rock-slope deformation. In *Landslides: Types, Mechanisms and Modeling* (pp. 207–221). Cambridge University Press.

Agliardi, F., Crosta, G., & Zanchi, A. (2001). Structural constraints on deep-seated slope deformation kinematics. *Engineering Geology*, *59*(1), 83–102. https://doi.org/10.1016/S0013-7952(00)00066-1

Allaby, M. (2020). *Dictionary of Geology and Earth Sciences* (5th ed.). Oxford University Press.

Ambrosi, C., & Crosta, G. B. (2006). Large sackung along major tectonic features in the Central Italian Alps. *Engineering Geology*, *83*(1), 183–200. https://doi.org/10.1016/j.enggeo.2005.06.031

Ballantyne, C. K. (2002). Paraglacial geomorphology. *Quaternary Science Reviews*.

Bergh, S., Eig, K., Kløvjan, O. S., Henningsen, T., Olesen, O., & Hansen, J.-A. (2007). The Lofoten-Vesterålen continental margin: A multiphase Mesozoic-Palaeogene rifted shelf as shown by offshore-onshore brittle fault-fracture analysis. *Norsk Geologisk Tidsskrift*, *87*, 29–58.

BGS. (2023). Understanding landslides. *British Geological Survey*. https://www.bgs.ac.uk/discovering-geology/earth-hazards/landslides/

Blikra, L. H., & Christiansen, H. H. (2014). A field-based model of permafrost-controlled rockslide deformation in northern Norway. *Geomorphology*, *208*, 34–49. https://doi.org/10.1016/j.geomorph.2013.11.014

Blikra, L. H., Henderson, I., & Nordvik, T. (2009). *Faren for fjellskred fra Nordnesfjellet i Lyngenfjorden, Troms* (2009.026; p. 29). NGU.

Blikra, L. H., Longva, O., Braathen, A., Anda, E., Dehls, J. F., & Stalsberg, K. (2006). ROCK SLOPE FAILURES IN NORWEGIAN FJORD AREAS: EXAMPLES, SPATIAL DISTRIBUTION AND TEMPORAL PATTERN. In S. G. Evans, G. S. Mugnozza, A. Strom, & R. L. Hermanns (Eds.), *Landslides from Massive Rock Slope Failure* (Vol. 49, pp. 475–496). Springer Netherlands. https://doi.org/10.1007/978-1-4020-4037-5_26

Böhme, M. (2014). *Spatial and temporal variability of rock slope instability in western Norway*. NTNU.

Bois, T., Bouissou, S., & Guglielmi, Y. (2008). Influence of major inherited faults zones on gravitational slope deformation: A two-dimensional physical modelling of the La Clapière area (Southern French Alps). *Earth and Planetary Science Letters*. https://www.academia.edu/34324001/Influence_of_major_inherited_faults_zones_on_gravitational_slope_deformation_A_two_dimensional_physical_modelling_of_the_La_Clapi%C3%A8re_area_Southern_French_Alps_

Braathen, A., Blikra, L. H., Berg, S. S., & Karlsen, F. (2004). Rock-slope failures in Norway; type, geometry, deformation mechanisms and stability. *NORWEGIAN JOURNAL OF GEOLOGY*.

Bradley, R. S. (2015). *PALEOCLIMATOLOGY Reconstructing Climates of the Quaternary* (3rd ed.). Elsevier Inc.

Brideau, M.-A., Yan, M., & Stead, D. (2009). The role of tectonic damage and brittle rock fracture in the development of large rock slope failures. *Geomorphology*, *103*, 30–49. https://doi.org/10.1016/j.geomorph.2008.04.010

Bunkholt, H. S. S., Redfield, T. F., Osmundsen, P. T., Oppikofer, T., Hermanns, R. L., & Dehls, J. F. (2012). *Landslide processes in hard rock in Troms, Norway*. 855–861.

Carlà, T., Tofani, V., Lombardi, L., Raspini, F., Bianchini, S., Bertolo, D., Thuegaz, P., & Casagli, N. (2019). Combination of GNSS, satellite InSAR, and GBInSAR remote sensing monitoring to improve the understanding of a large landslide in high alpine environment. *Geomorphology*, *335*, 62–75. https://doi.org/10.1016/j.geomorph.2019.03.014

Carter, T. G., & Marinos, V. (2020). Putting Geological Focus Back into Rock Engineering Design. *Rock Mechanics and Rock Engineering*, *53*(10), 4487–4508. https://doi.org/10.1007/s00603-020-02177-1

Clague, J. J., & Stead, D. (Eds.). (2012). *Landslides: Types, Mechanisms and Modeling*. Cambridge University Press. https://doi.org/10.1017/CBO9780511740367

Coker-Dewey, J., Steltenpohl, M. G., & Andresen, A. (2000). Geology of western Ullsfjord, North Norway, with emphasis on the development of an inverted metamorphic gradient at the top of the Lyngen Nappe Complex. *Norsk Geologisk Tidsskrift*, *80*(2), 111–118. https://doi.org/10.1080/002919600750042609

Crippa, C., Valbuzzi, E., Frattini, P., Crosta, G. B., Spreafico, M. C., & Agliardi, F. (2021). Semi-automated regional classification of the style of activity of slow rock-slope deformations using

PS InSAR and SqueeSAR velocity data. *Landslides*, *18*(7), 2445–2463. https://doi.org/10.1007/s10346-021-01654-0

Crosta, G. B., Frattini, P., & Agliardi, F. (2013). Deep seated gravitational slope deformations in the European Alps. *Tectonophysics*, *605*, 13–33. https://doi.org/10.1016/j.tecto.2013.04.028

Dahl, H., Anda, E., Saintot, A., & Saetre, S. (2008). *Faren for fjellskred fra fjellet Mannen i Romsdalen* (2008.087; p. 21). NGU.

Dannevig, P. (2023). *Store norske leksikon*. https://snl.no/Troms_-_klima

Delaloye, R., & Echelard, T. (2021). *IPA Action Group Rock glacier inventories and kinematics*. University of Fribourg.

Eggers, M. (2023). *Hazard assessment_GEO_3135*.

Eiken, T., Redfield, T., Böhme, M., Bunkholt, H., Otterå, S., Yugsi Molina, F. X., Hermanns, R. L., Dehls, J., & Osmundsen, P. T. (2013). Undersøkelser av ustabile fjellpartier i Troms—Status og planer etter feltarbeid 2011 og 2012. In *110* [Report]. NGU. https://openarchive.ngu.no/ngu-xmlui/handle/11250/2664473

Einstein, H., Veneziano, D., Baecher, G., & O'Reilly, K. J. (1983). The effect of discontinuity Persistence an Rock Slope Stability. *International Journal of Rock Mechanics and Mining Sciences & Geomechanics Abstracts*, *20*, 227–236. https://doi.org/10.1016/0148-9062(83)90003-7

Elmo, D., Donati, D., & Stead, D. (2018). Challenges in the characterisation of intact rock bridges in rock slopes. *Engineering Geology*, *245*, 81–96. https://doi.org/10.1016/j.enggeo.2018.06.014

Eriksen, H. Ø., Bergh, S. G., Larsen, Y., Skrede, I., Kristensen, L., Lauknes, T. R., Blikra, L. H., & Kierulf, H. P. (2017). Relating 3D surface displacement from satellite- and ground-based InSAR to structures and geomorphology of the Jettan rockslide, northern Norway. *Norwegian Journal of Geology*. https://doi.org/10.17850/njg97-4-03

Ferretti, A., Prati, C., & Rocca, F. (2001). Permanent scatterers in SAR interferometry. *IEEE Transactions on Geoscience and Remote Sensing*, *39*(1), 8–20. https://doi.org/10.1109/36.898661

Frattini, P., Crosta, G. B., Rossini, M., & Allievi, J. (2018). Activity and kinematic behaviour of deep-seated landslides from PS-InSAR displacement rate measurements. *Landslides*, *15*(6), 1053–1070. https://doi.org/10.1007/s10346-017-0940-6

Harbitz, C. B., Pedersen, G., & Gjevik, B. (1991). *Model simulations of large water waves due to landslides*.

Henderson, I. H. C., Osmundsen, P. T., & Redfield, T. F. (2008). *ROS Fjellskred i Troms: Statusrapport 2007 | NGU* (310000). NGU. https://www.ngu.no/publikasjon/ros-fjellskred-i-troms-statusrapport-2007

Hermanns, R. L., & Longva, O. (2012). Rapid rock-slope failures. In J. J. Clague & D. Stead (Eds.), *Landslides: Types, Mechanisms and Modeling* (1st ed., pp. 59–70). Cambridge University Press. https://doi.org/10.1017/CBO9780511740367.007

Hermanns, R. L., Oppikofer, T., & John, D. (2014). Approach for Systematic Rockslide Mapping of Unstable Rock Slopes in Norway. *Landslide Science for a Safer Geoenvironment*, *3*, 129–134. https://doi.org/10.1007/978-3-319-04996-0_2

Hermanns, R., Oppikofer, T., Anda, E., Blikra, L., Böhme, M., Bunkholt, H., Crosta, G., Dahle, H., Devoli, G., Fischer, L., Jaboyedoff, M., Loew, S., Sætre, S., & Yugsi Molina, F. X. (2012). *Recommended hazard and risk classification system for large unstable rock slopes in Norway*.

Highland, L. M., & Bobrowsky, P. (2008). *The landslide handbook—A guide to understanding landslides* (Circular 1325). U.S. Geological Survey.

Hoek, E., Carranza-Torres, C., & Corkum, B. (2002). *HOEK-BROWN FAILURE CRITERION – 2002 EDITION*.

Höpfl, S., & Konopásek, J. (2023). *Tectonic position and evolution of the Balsfjord Series in the North Norwegian Caledonides* (EGU23-8445). EGU23. Copernicus Meetings. https://doi.org/10.5194/egusphere-egu23-8445

Hungr, O., Leroueil, S., & Picarelli, L. (2014). The Varnes classification of landslide types, an update. *Landslides*, *11*(2), 167–194. https://doi.org/10.1007/s10346-013-0436-y

Indrevaer, K., Bergh, S. G., Koehl, J.-B., Hansen, J.-A., & Schermer, E. R. (2013). Post-Caledonian Brittle Fault Zones on the Hyperextended SW Barents Sea Margin: New Insights into Onshore and Offshore Margin Architecture. *NORWEGIAN JOURNAL OF GEOLOGY*.

Intrieri, E., Frodella, W., Raspini, F., Bardi, F., & Tofani, V. (2020). Using Satellite Interferometry to Infer Landslide Sliding Surface Depth and Geometry. *Remote Sensing*, *12*(9), Article 9. https://doi.org/10.3390/rs12091462

ISRM. (1985). SUGGESTED METHOD FOR DETERMINING POINT LOAD STRENGTH. *International Journal of Rock Mechanics and Mining Sciences*, *22*, 51–60.

Koehl, J.-B. P., Bergh, S. G., Osmundsen, P.-T., Redfield, T. F., Indrevær, K., Lea, H., & Bergø, E. (2019). Late Devonian–Carboniferous faulting and controlling structures and fabrics in NW Finnmark. *Norwegian Journal of Geology*. https://doi.org/10.17850/njg99-3-5

Kranz, R. (1983). *Microcracks-in-rocks*.

Lauknes, T. (2010). Detailed rockslide mapping in northern Norway with small baseline and persistent scatterer interferometric SAR time series methods. *Remote Sensing of Environment*. https://www.academia.edu/30819068/Detailed_rockslide_mapping_in_northern_Norway_with_small_baseline_and_persistent_scatterer_interferometric_SAR_time_series_methods

Leroueil, S., & Locat, J. (1996). *Slope movements—Geotechnical characterization, risk assessment and mitigation*. 933–944. https://doi.org/10.1201/9781003078173-6

Liu, L., Millar, C. I., Westfall, R. D., & Zebker, H. A. (2013). Surface motion of active rock glaciers in the Sierra Nevada, California, USA: Inventory and a case study using InSAR. *The Cryosphere*, *7*(4), 1109–1119. https://doi.org/10.5194/tc-7-1109-2013

Lysså, A. (1999). *Kartblad Balsfjord 1533-1, kvartærgeologisk kart* [Map]. Norges geologiske undersøkelse.

McKERROW, W. S., Mac Niocaill, C., & Dewey, J. F. (2000). The Caledonian Orogeny redefined. *Journal of the Geological Society*, *157*(6), 1149–1154. https://doi.org/10.1144/jgs.157.6.1149

Meteorologisk institutt. (2023). https://seklima.met.no/observations/

NGU. (2024a). *Nasjonal database for ustabile fjellparti* [dataset]. https://geo.ngu.no/kart/ustabilefjellparti_mobil/

NGU. (2024b). *Om InSAR Norge*. Norges Geologiske Undersøkelse. https://www.ngu.no/geologisk-kartlegging/hva-er-insar

Northrup, C. J. (1996). Structural expressions and tectonic implications of general noncoaxial flow in the midcrust of a collisional orogen: The northern Scandinavian Caledonides. *Tectonics*, *15*(2), 490–505. https://doi.org/10.1029/95TC02951

Olsen, L., Sveian, H., Bergstrøm, B., Ottesen, D., & Rise, L. (2013). *Quaternary glaciations and their variations in Norway and on the Norwegian continental shelf*.

Oppikofer, T., Saintot, A., Hermanns, R. L., Böhme, M., Scheiber, T., Gosse, J., & Dreiås, G. M. (2017). From incipient slope instability through slope deformation to catastrophic failure—Different stages of failure development on the Ivasnasen and Vollan rock slopes (western Norway). *Geomorphology*, *289*, 96–116. https://doi.org/10.1016/j.geomorph.2017.03.015

Özbek, A., Gül, M., Karacan, E., & Alca, Ö. (2018). Anisotropy effect on strengths of metamorphic rocks. *Journal of Rock Mechanics and Geotechnical Engineering*, *10*(1), 164–175. https://doi.org/10.1016/j.jrmge.2017.09.006

Panazzolo, D., & da Silva, P. R. (2017). Regularization of discontinuous foliations: Blowing up and sliding conditions via Fenichel theory. *Journal of Differential Equations*, *263*(12), 8362–8390. https://doi.org/10.1016/j.jde.2017.08.042

Paronuzzi, P., Bolla, A., & Rigo, E. (2015). Brittle and Ductile Behavior in Deep-Seated Landslides: Learning from the Vajont Experience. *Rock Mechanics and Rock Engineering*, *49*. https://doi.org/10.1007/s00603-015-0815-x

Penna, I. M., Magnin, F., Nicolet, P., Etzelmüller, B., Hermanns, R. L., Böhme, M., Kristensen, L., Nöel, F., Bredal, M., & Dehls, J. F. (2023). Permafrost controls the displacement rates of large unstable rock-slopes in subarctic environments. *Global and Planetary Change*, *220*, 104017. https://doi.org/10.1016/j.gloplacha.2022.104017

Ramberg, I. B., Bryhni, I., Nøttvedt, A., & Rangnes, K. (2013). *Landet blir til* (2nd ed.). Norsk Geologisk Forening.

Rasmussen, E. (2011). *Fjellskred i Laksvatnfjellet, Balsfjord, Troms: Indre struktur, morfologi og skredmekanismer* [Master's thesis]. Norges arktiske universitet.

Rigopoulos, I., Tsikouras, B., Pomonis, P., & Hatzipanagiotou, K. (2013). Petrographic Investigation of Microcrack Initiation in Mafic Ophiolitic Rocks Under Uniaxial Compression. *Rock Mechanics and Rock Engineering*, *46*. https://doi.org/10.1007/s00603-012-0310-6

Rouyet, L., Lauknes, T. R., Christiansen, H. H., Strand, S. M., & Larsen, Y. (2019). Seasonal dynamics of a permafrost landscape, Adventdalen, Svalbard, investigated by InSAR. *Remote Sensing of Environment*, *231*, 111236. https://doi.org/10.1016/j.rse.2019.111236

Saintot, A., Henderson, I. H. C., & Derron, M.-H. (2011). Inheritance of ductile and brittle structures in the development of large rock slope instabilities: Examples from western Norway. *Geological Society, London, Special Publications*, *351*(1), 27–78. https://doi.org/10.1144/SP351.3

Samsonov, S., Dille, A., Dewitte, O., Kervyn, F., & d'Oreye, N. (2019). Satellite interferometry for mapping surface deformation time series in one, two and three dimensions: A new method illustrated on a slow-moving landslide. *Engineering Geology*, *266*, 105471. https://doi.org/10.1016/j.enggeo.2019.105471

Sandbakken, H. (2021). *Characterizing slope processes along the Piggtind mountain ridge, using 2D InSAR* [Master's thesis]. Norges arktiske universitet.

Solhaug, R. M. (2015). *Hvorfor er det så vanskelig å forutsi fjellskred?* [University website]. https://uit.no/nyheter/artikkel?p_document_id=444054

Stead, D., & Eberhardt, E. (2013). Understanding the mechanics of large landslides. *Italian Journal of Engineering Geology and Environment*, *2013 book series n.6*, 85–112. https://doi.org/10.4408/IJEGE.2013-06.B-07

Stead, D., & Wolter, A. (2015). A critical review of rock slope failure mechanisms: The importance of structural geology. *Journal of Structural Geology*, *74*, 1–23. https://doi.org/10.1016/j.jsg.2015.02.002

Steltenpohl, M. G., Andresen, A., & Tull, J. M. (1990). Lithostratigraphic correlation of the Salangen (Ofoten) and Balsfjord (Troms) Groups: Evidence for post-Finnmarkian unconformity, North Norwegian Caledonides. *Norges Geologiske Undersøkelse Bulletin*, *418*, 61–77.

Varnes, D. J. (1978). Slope Movement Types and Processes. *Special Report 176*, 11–33.

Vick, L. M. (2023, September 1). *Slow mountain and rock slope deformations* [Lecture].

Vick, L. M., Böhme, M., Rouyet, L., Bergh, S. G., Corner, G. D., & Lauknes, T. R. (2020). Structurally controlled rock slope deformation in northern Norway. *Landslides*, *17*(8), 1745–1776. https://doi.org/10.1007/s10346-020-01421-7

Wright, T. J., Parsons, B. E., & Lu, Z. (2004). Toward mapping surface deformation in three dimensions using InSAR. *Geophysical Research Letters*, *31*(1). https://doi.org/10.1029/2003GL018827

Zangerl, C., Prager, C., Brandner, R., Brückl, E., Edeer, S., Fellin, W., Tentschert Ewald, Poscher, G., & Schönlaub, H. (2008). Methodischer Leitfaden Zur Prozessorientierten Bearbeitung von Massenbewegungen. *Geo. Alp*, *5*, 1–51.

Zwaan, K. B. (1995). *Geology of the West Troms Basement Complex, northern Norway, with emphasis on the Senja Shear Belt: A preliminary account*.

Zwaan, K. B., Fareth, E., & Grogan, P. W. (1998). *Berggrunnskart Tromsø 1:250 000 trykt i farger* [Scannet fra kart]. Norges geologiske undersøkelse.

Appendix

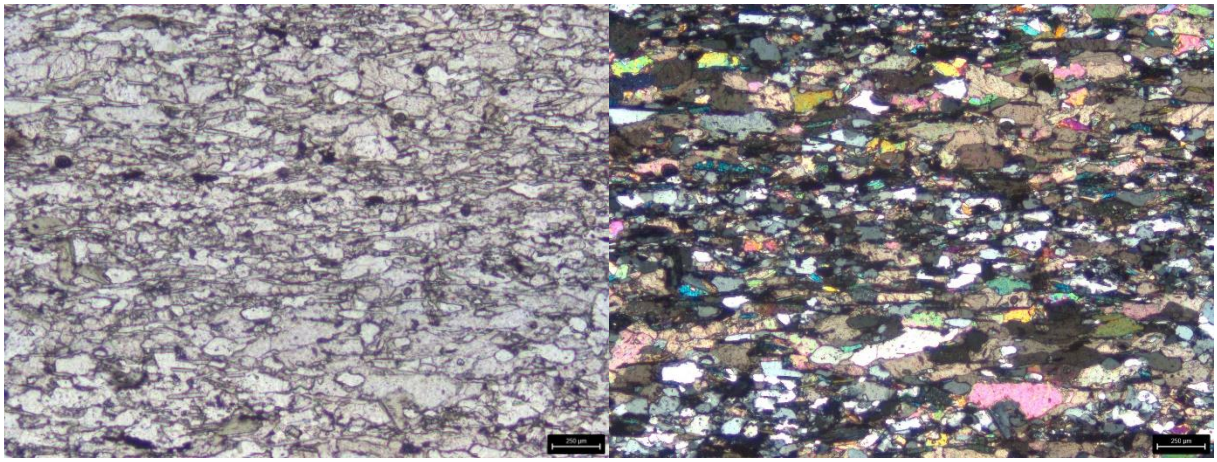

Figure 1 Thin section from location 3, PPL on the left and in XPL on the right.

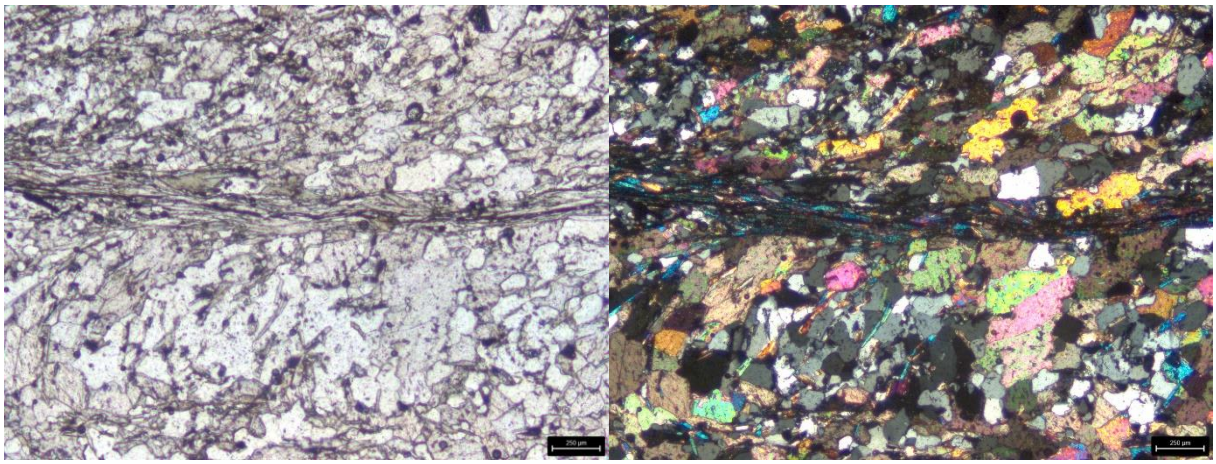

Figure 2 Thin section from location 3, PPL on the left and in XPL on the right.

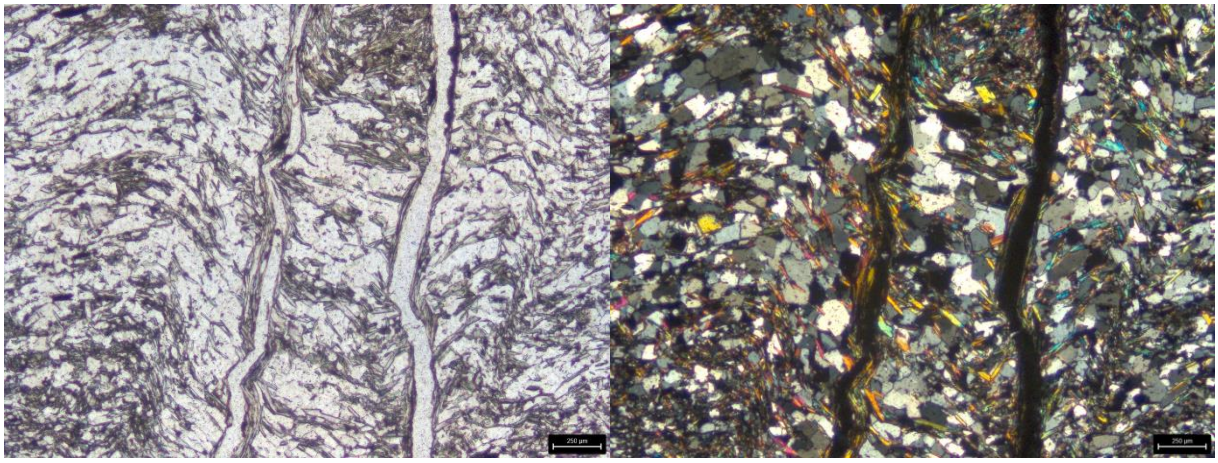

Figure 3 Thin section from location 4, PPL on the left and in XPL on the right.

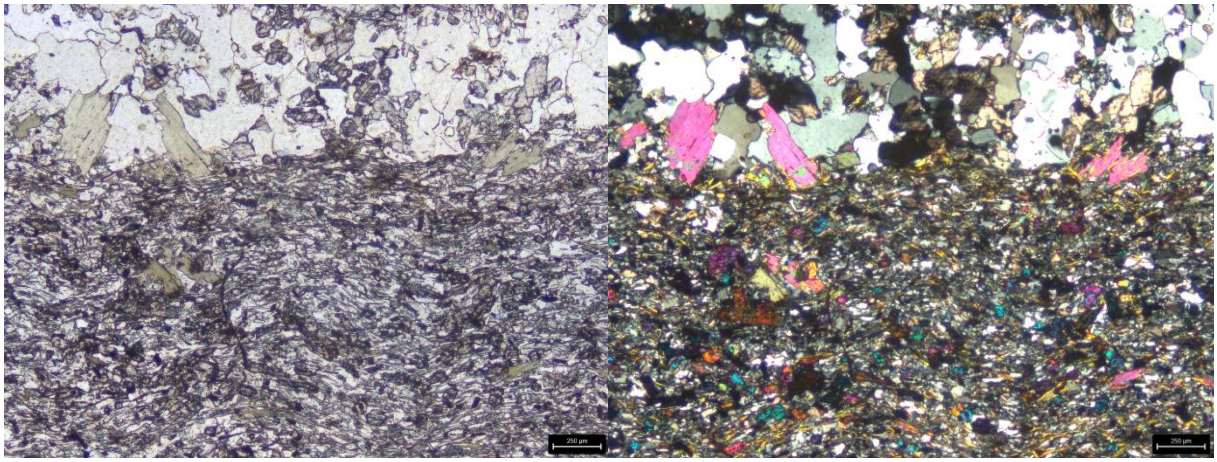

Figure 4 Thin section from location 5, PPL on the left and in XPL on the right.

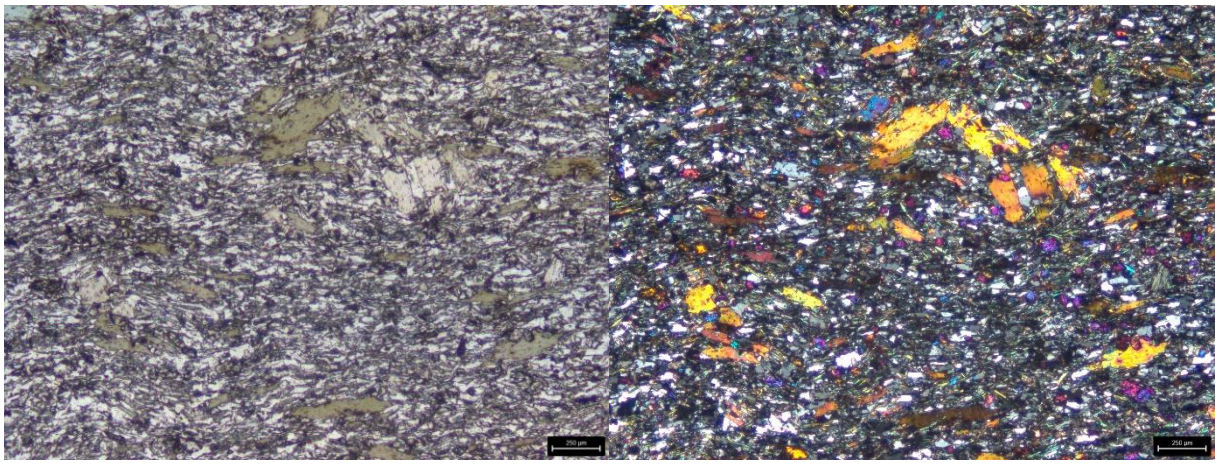

Figure 5 Thin section from location 5, PPL on the left and in XPL on the right.

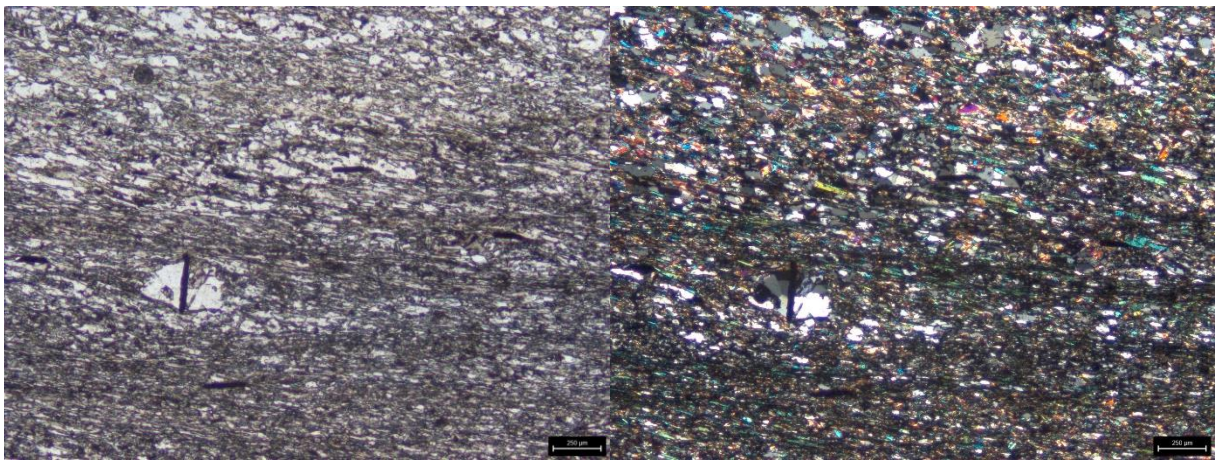

Figure 6 Thin section from location 6, PPL on the left and in XPL on the right.

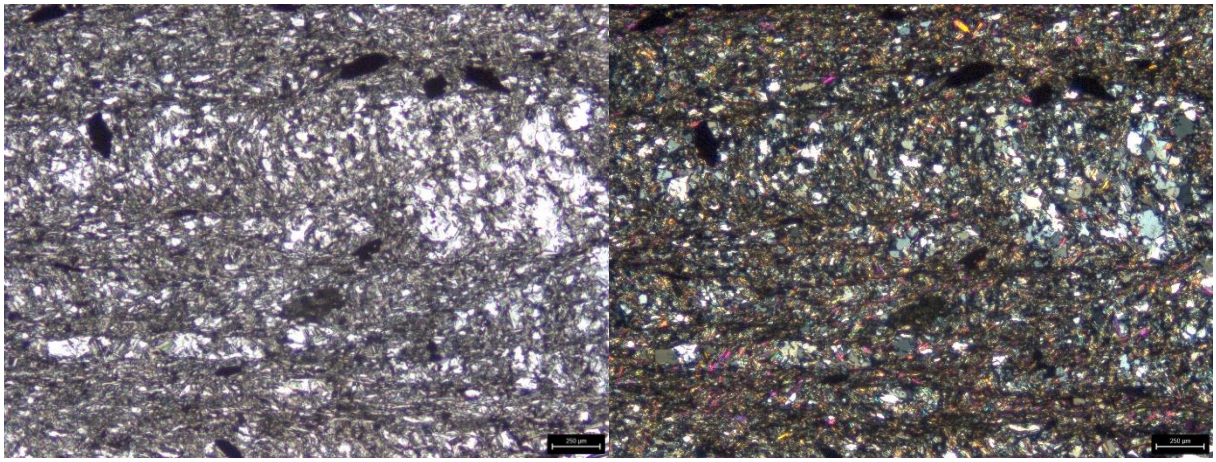

Figure 8 Thin section from location 8, PPL on the left and in XPL on the right.

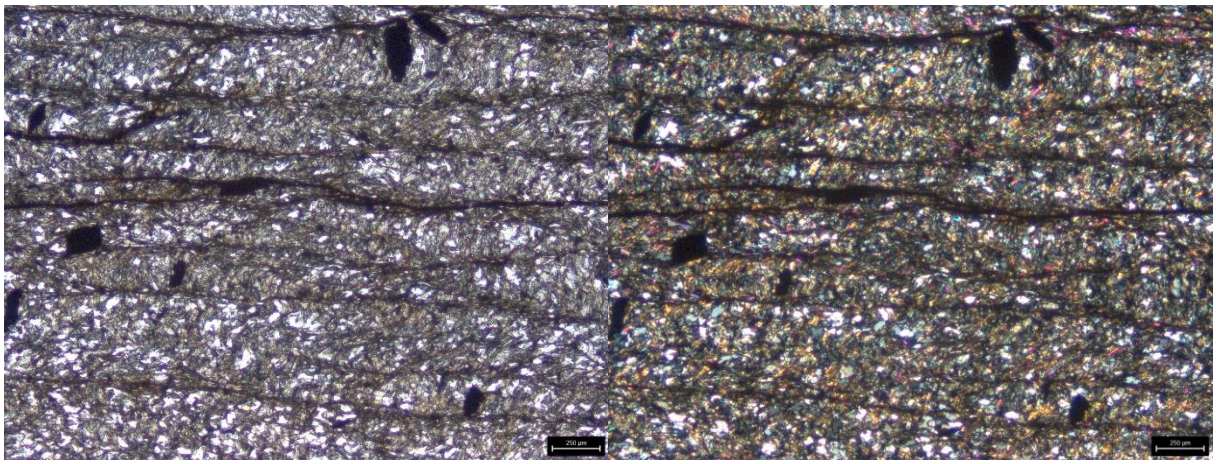

Figure 7 Thin section from location 8, PPL on the left and in XPL on the right.

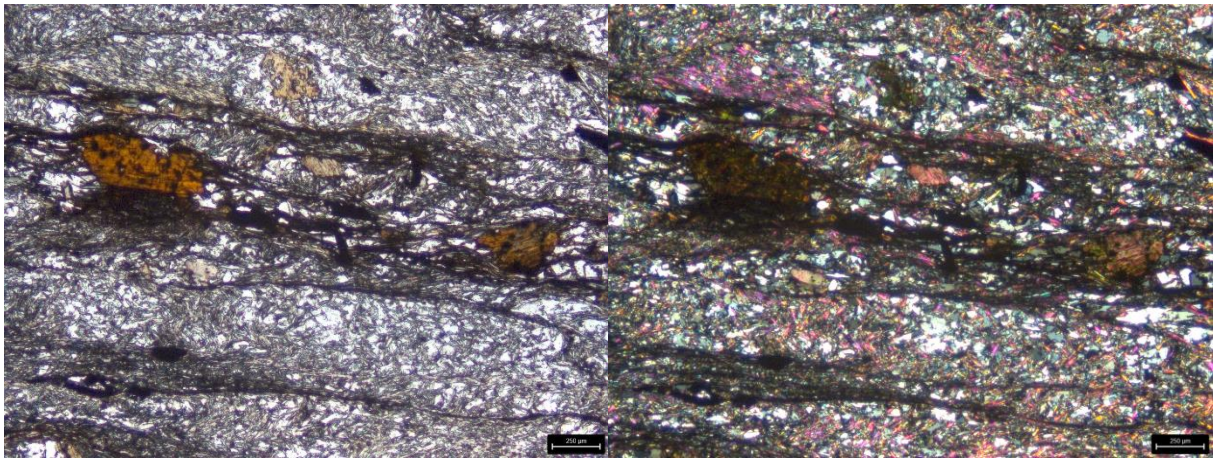

Figure 9 Thin section from location 9, PPL on the left and in XPL on the right.

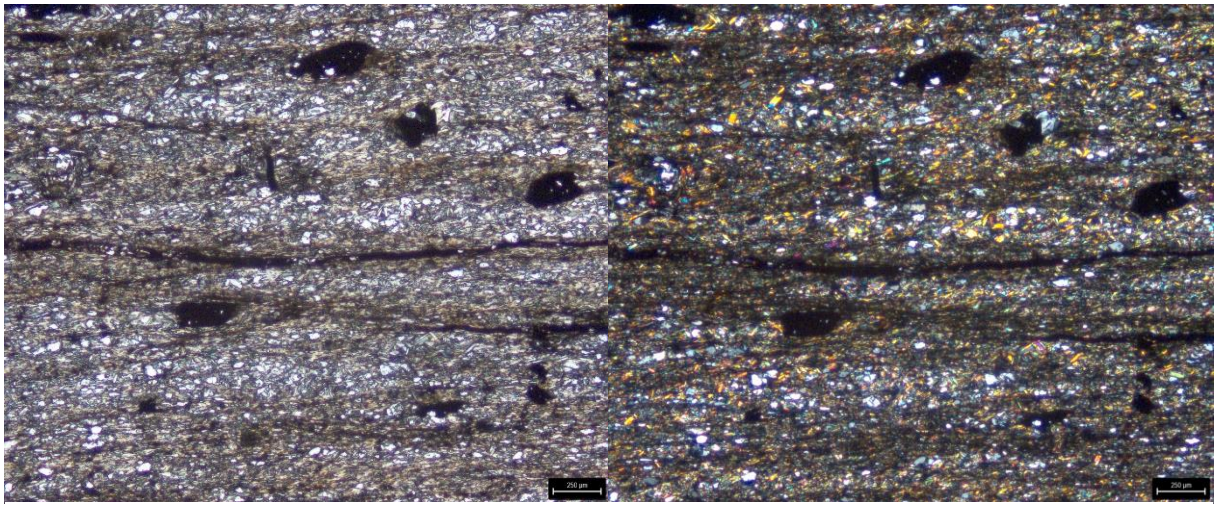

Figure 11 Thin section from location 10, PPL on the left and in XPL on the right.

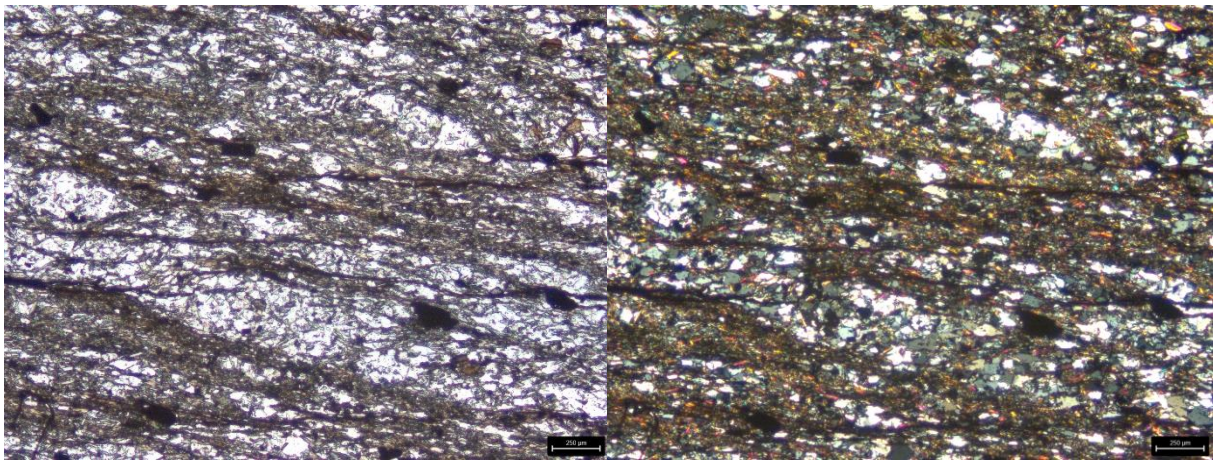

Figure 10 Thin section from location 11, PPL on the left and in XPL on the right.

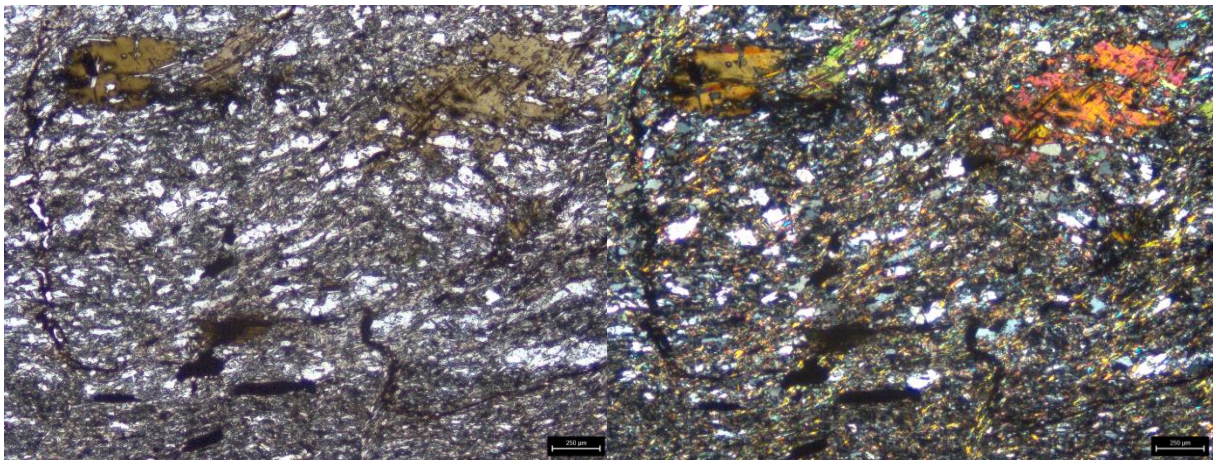

Figure 12 Thin section from location 12, PPL on the left and in XPL on the right.

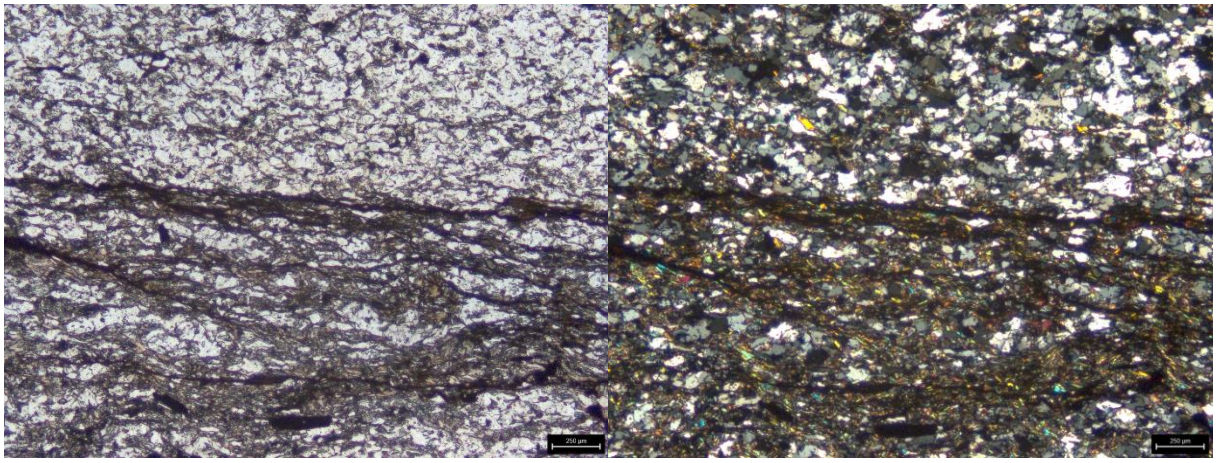

Figure 13 Thin section from location 12, PPL on the left and in XPL on the right.

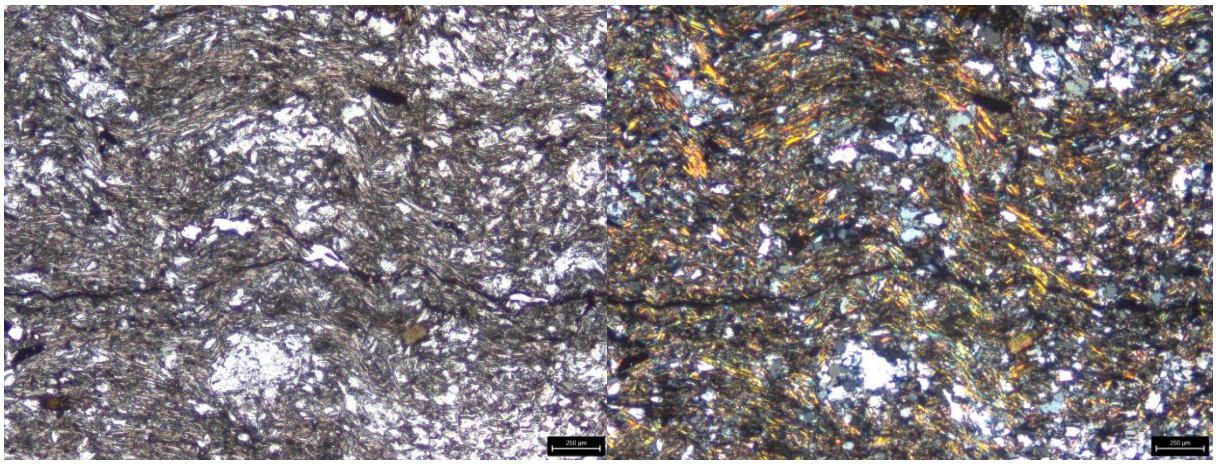

Figure 14 Thin section from location 13, PPL on the left and in XPL on the right.

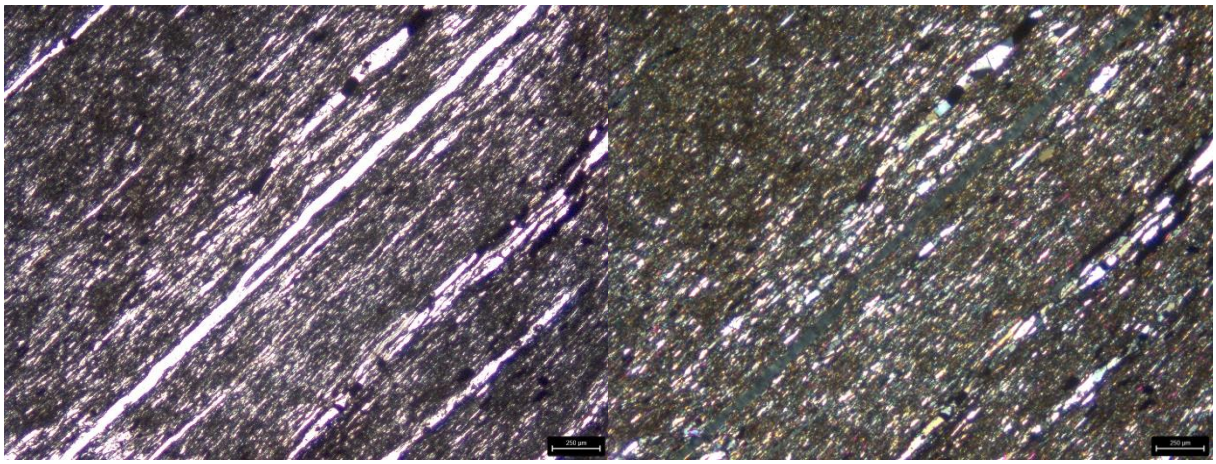

Figure 15 Thin section from location 14, PPL on the left and in XPL on the right.

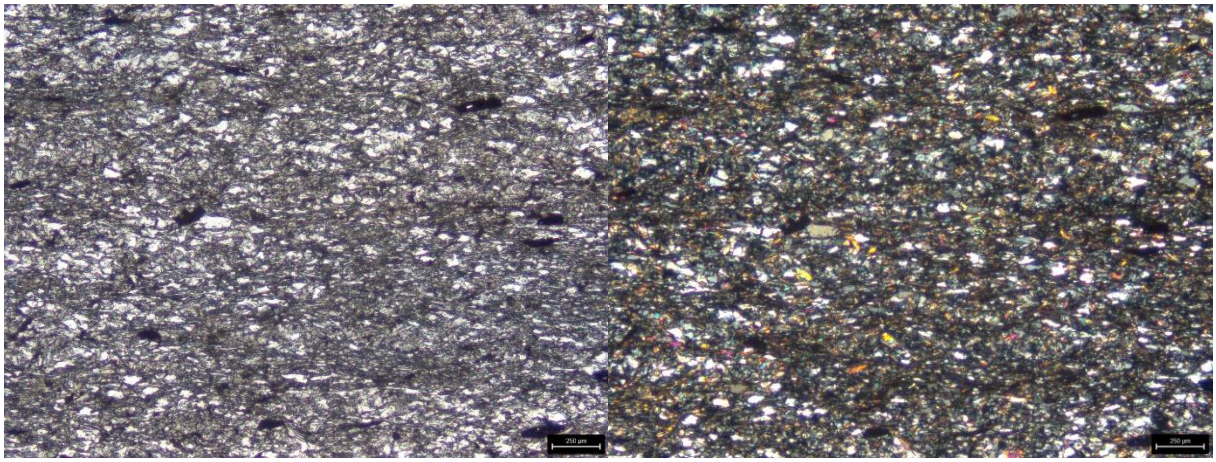

Figure 16 Thin section from location 15, PPL on the left and in XPL on the right.

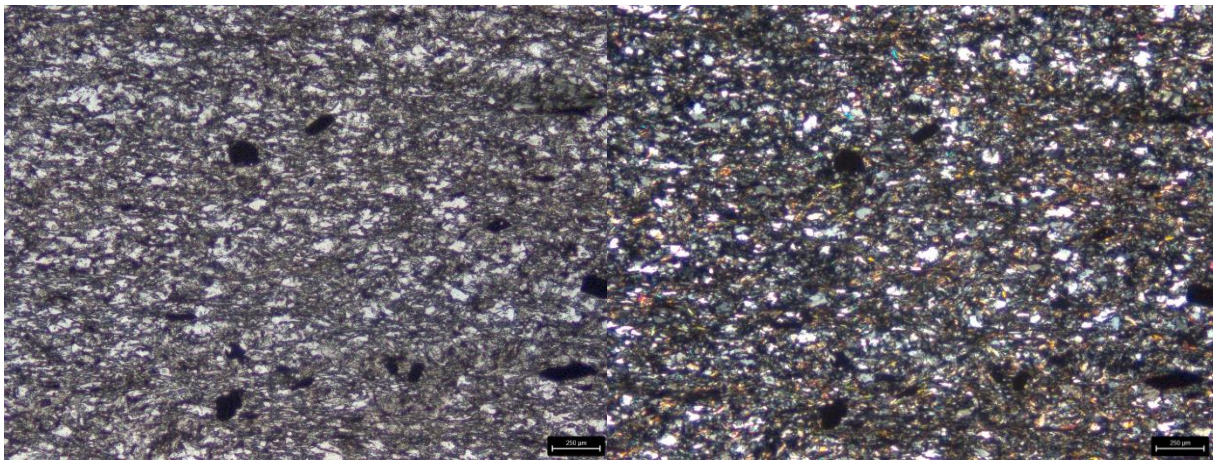

Figure 17 Thin section from location 15, PPL on the left and in XPL on the right.

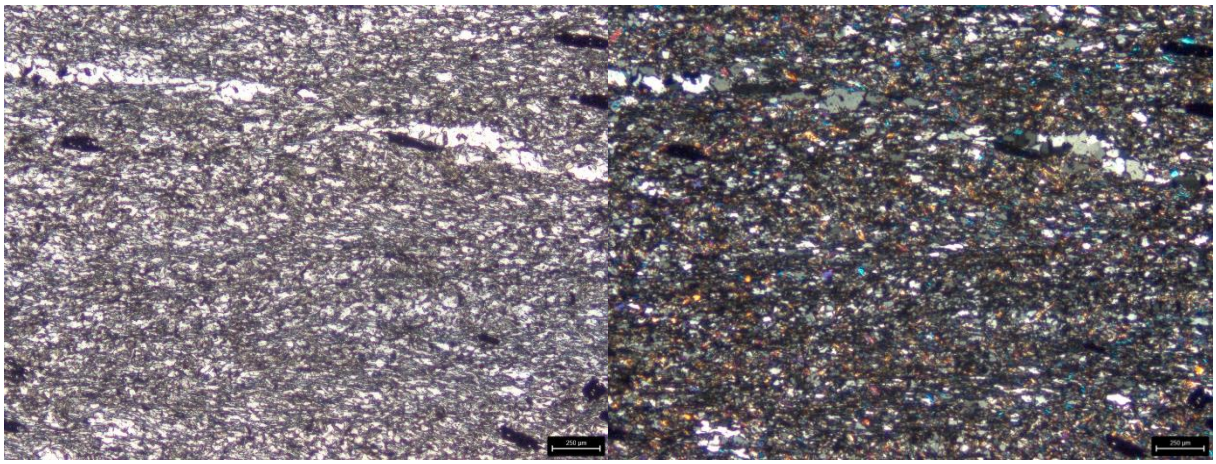

Figure 18 Thin section from location 16, PPL on the left and in XPL on the right.

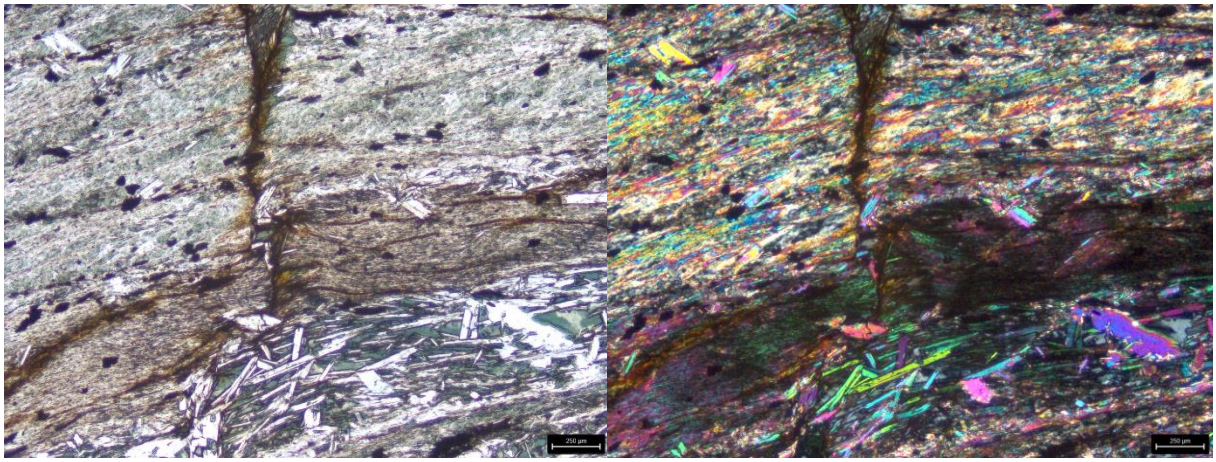

Figure 20 Thin section from location 17, PPL on the left and in XPL on the right.

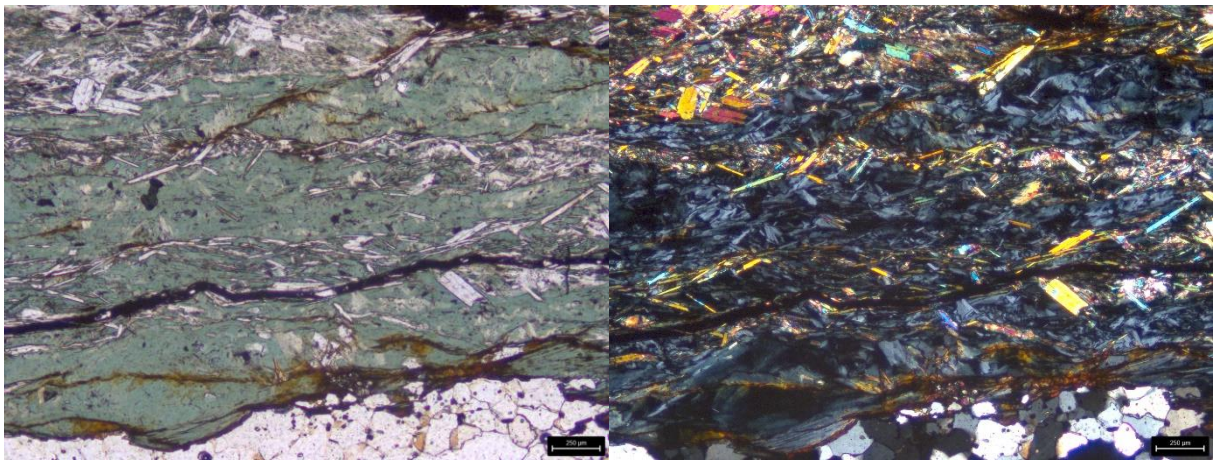

Figure 19 Thin section from location 17, PPL on the left and in XPL on the right.

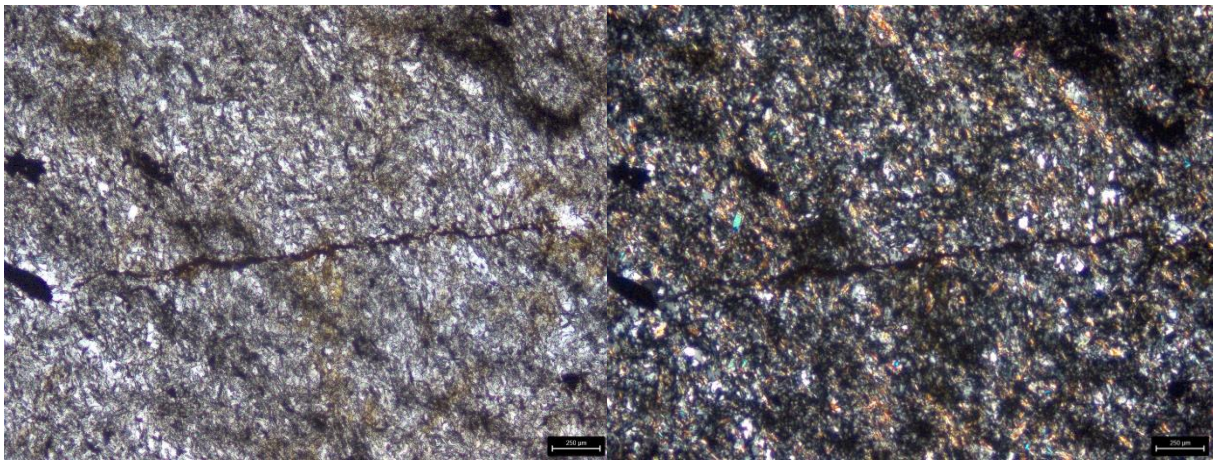

Figure 21 Thin section from location M2, PPL on the left and in XPL on the right.

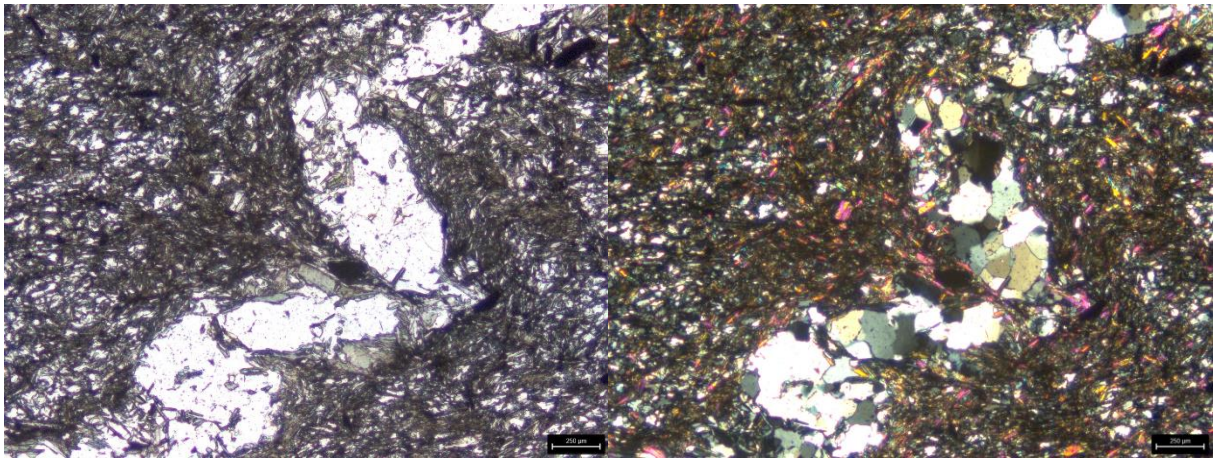

Figure 23 Thin section from location M3, PPL on the left and in XPL on the right.

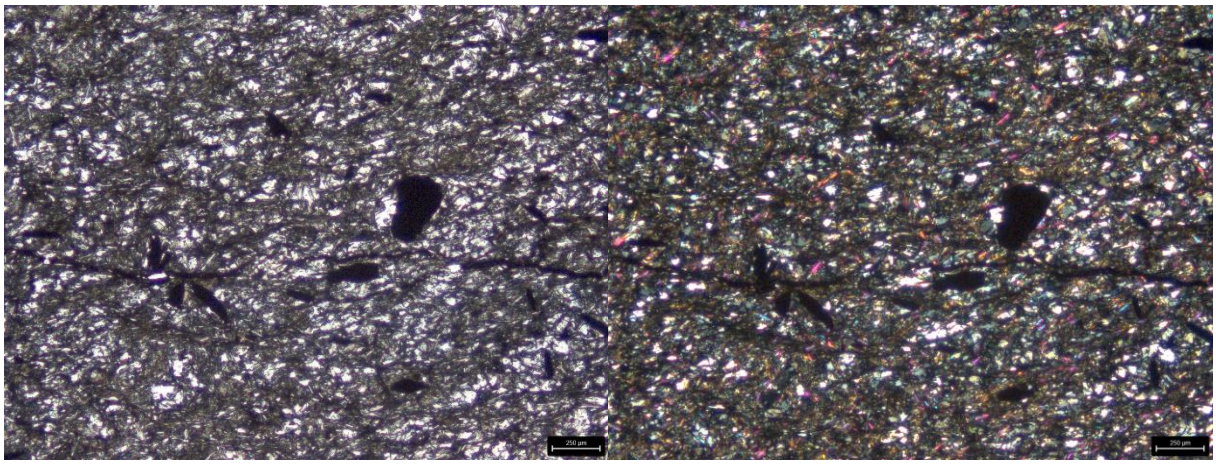

Figure 22 Thin section from location M3, PPL on the left and in XPL on the right.

Location 1	Fracture Plane			Foliation Plane		Comments
	Dip Direction	Dip		Dip Direction	Dip	
	308	78		183	15	
	317	66		332	10	
	314	70		108	15	
	125	90		184	13	
	122	87		173	12	
	218	28		273	11	
1b	98	82		124	12	
1b	122	81		326	0	
1b	184	79		146	10	
1b	197	87		146	9	
1b	113	82		184	3	1b
				179	8	1b
Location 2	90	59		260	13	
	217	52		294	14	
	63	66		267	17	
	74	66		249	11	
	97	39		289	8	
	94	54		256	27	
	92	50		302	12	
	286	10		292	10	
	100	48		314	14	
	57	41		257	16	
	106	54		302	14	
	38	67		289	16	
	188	68		280	6	
	118	54		280	16	
	90	49		238	18	
	200	52				
	148	86				
	150	19				
	128	78				
	226	42				
	146	28				
Location 3	107	58		321	28	
	176	66		313	18	
	127	50		208	58	Fa 122/06
	174	75		210	60	
	104	80		258	58	
	179	60		258	18	
	81	34				
	82	90				
	272	59				

	149	36				
Location 4				138	19	S1
				214	44	S2
				176	31.5	
Location 5	79	65		213	12	
	39	40		116	26	
	85	89				
	49	34				
	39	28				
Location 6	137	87		32	29	
	46	24		45	28	
	152	76		47	25	
	141	82		57	18	
	139	90		6	27	
	44	24		62	23	
	296	62		39	27	
	136	81				
Location 7	98	86		272	11	
	166	73		352	20	
	61	73		333	14	
	284	80		332	9	
	320	82		30	30	
	296	85		32	25	
	257	78		274	19	
				358	15	
Location 8	186	32		178	26	
	48	61		202	36	
	41	65		218	48	
	41	14				
	126	86				
	132	90				
	138	83				
Location 9	220	18		245	16	
	298	61		246	17	
	325	86		221	19	
	249	48		249	29	
	231	47		243	22	
	306	86		225	17	
	320	85		235	34	
Location 10	142	88		116	4	

	324	62		199	31	
	217	66		203	18	
	233	53		215	14	
	320	80		281	20	
	310	74		266	38	
	338	77		221	16	
	314	61		281	4	
	346	72		210	16	
	321	86		196	3	
	237	62				
	350	85				
	354	80				
	353	82				
	239	29				
	243	54				
	342	82				
	343	80				
	339	85				
	226	62				
	255	38				
	310	86				
	335	72				
	355	78				
Location 11	114	48		138	18	
	166	74		190	10	
	137	61		212	11	
	267	84		329	3	
	108	80		233	9	
	113	88		221	13	
	359	68		183	10	
	336	67		207	10	
	328	71		189	12	
	334	59		205	9	
	229	84		234	9	
	340	71		177	9	
	54	82		186	9	
	219	88		189	9	
	329	82		226	10	
	102	88		229	10	
	115	78		230	10	
	78	85				
	26	88				
	94	85				
	113	83				
	100	80				

	112	89				
	285	55				
	190	29				
	15	66				
	165	84				
	15	82				
	10	81				
	358	82				
	40	81				
	353	81				
	299	82				
	289	50				
	74	79				
	75	74				
	74	87				
	85	75				
	81	75				
	93	77				
	347	46				
	353	48				
	110	69				
	111	70				
	238	88				
	1	66				
	5	66				
	2	65				
Location 12	156	76		314	19	
	149	85		326	23	
	130	87		281	20	
	143	80		329	16	
	138	78		291	12	
	139	80		330	16	
	206	58		312	23	
	48	73		322	23	
	215	80		320	19	
	125	80		320	21	
	49	75		168	81	
	120	82		331	28	
	217	74		338	25	
	83	86		315	23	
	127	88				
	251	51				
	252	63				
	84	80				
	32	57				

	44	73				
	272	75				
	264	43				
	297	65				
	220	68				
	215	72				
	283	80				
	251	62				
	237	81				
	326	87				
	193	77				
	148	82				
	154	81				
	154	67				
	238	66				
	267	58				
	318	87				
	318	86				
	221	80				
	301	55				
	127	83				
	118	78				
	46	26				
	143	76				
	102	65				
Location 13	141	81		348	27	
	146	78		331	13	
	231	81		239	23	
	140	83				
	227	74				
	209	84				
	139	82				
	63	83				
	13	81				
	5	73				
	329	74				
	357	79				
	352	90				
	47	55				
	15	64				
	35	54				
	19	76				
	51	67				
	163	78				
	105	77				

	159	88				
	37	74				
	197	88				
	157	72				
	155	75				
	211	67				
	240	64				
	54	82				
	96	84				
	190	80				
Location 14	99	82		164	12	207/08 fold axis
	114	80		150	7	197/09 fold axis
	102	87		162	4	192/11 fold axis
	99	88		159	5	195/09 fold axis
	16	38				
	10	35				
	14	40				
Location 15	102	83		113	18	
	109	74		228	15	
	168	88		156	30	
	152	81		187	4	
	138	80		187	7	
	188	89		228	10	
	358	86		222	18	
	101	86				
	105	72				
	178	82				
	176	79				
	92	77				
	99	83				
Location 16	64	76		238	9	
	140	84		184	18	
	225	74		215	8	
	137	78		175	20	
	84	78		162	7	
	100	82		156	18	
	184	88		200	10	
	113	81		210	11	
	82	86		188	7	
	20	77		193	9	

	110	87				
	91	88				
	172	85				
Location 17	93	79		196	4	
	52	80		300	30	
	104	86		303	18	
	118	88		294	19	
	114	83		293	25	
	187	82		295	11	
	182	84		291	9	
	98	75		303	6	
	110	42				
	112	44				
	109	46				
Entities	266	266		136	136	

Table 1 Structural measurements at each location; measurements in beige are taken with the Field move

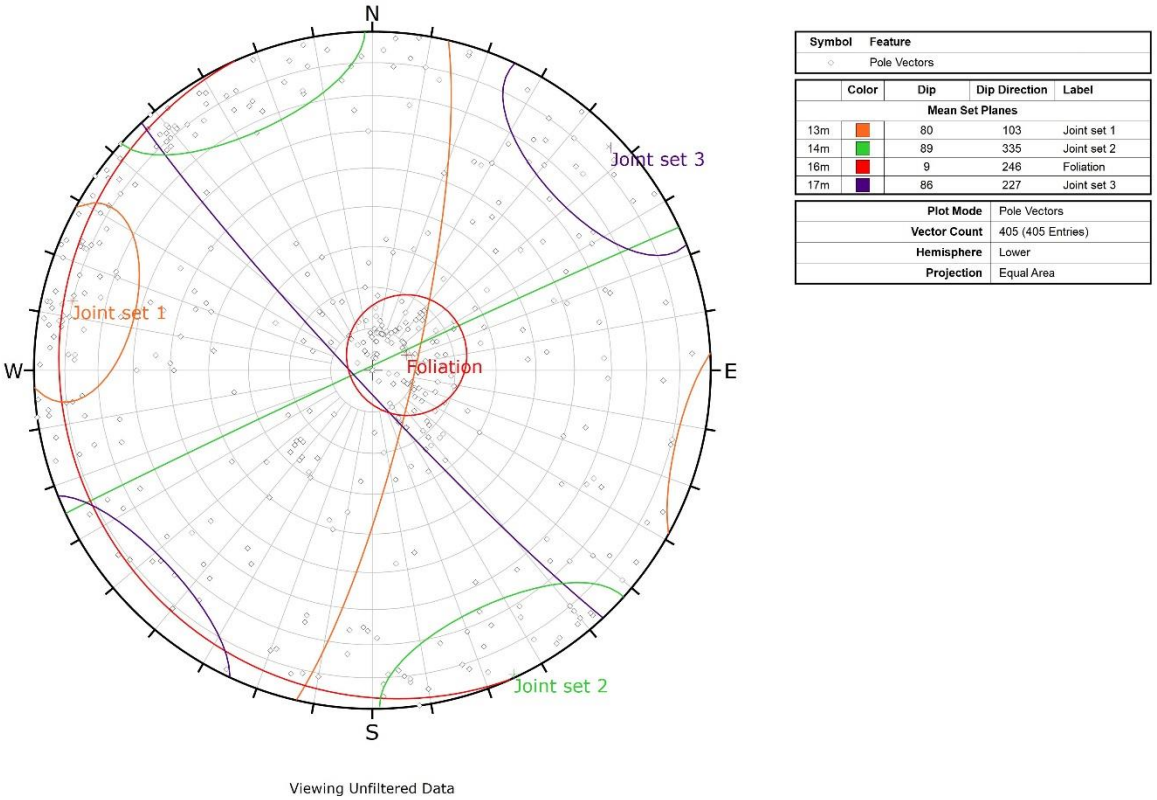

Figure 24 Stereographic projection with vector poles, foliation and joint sets

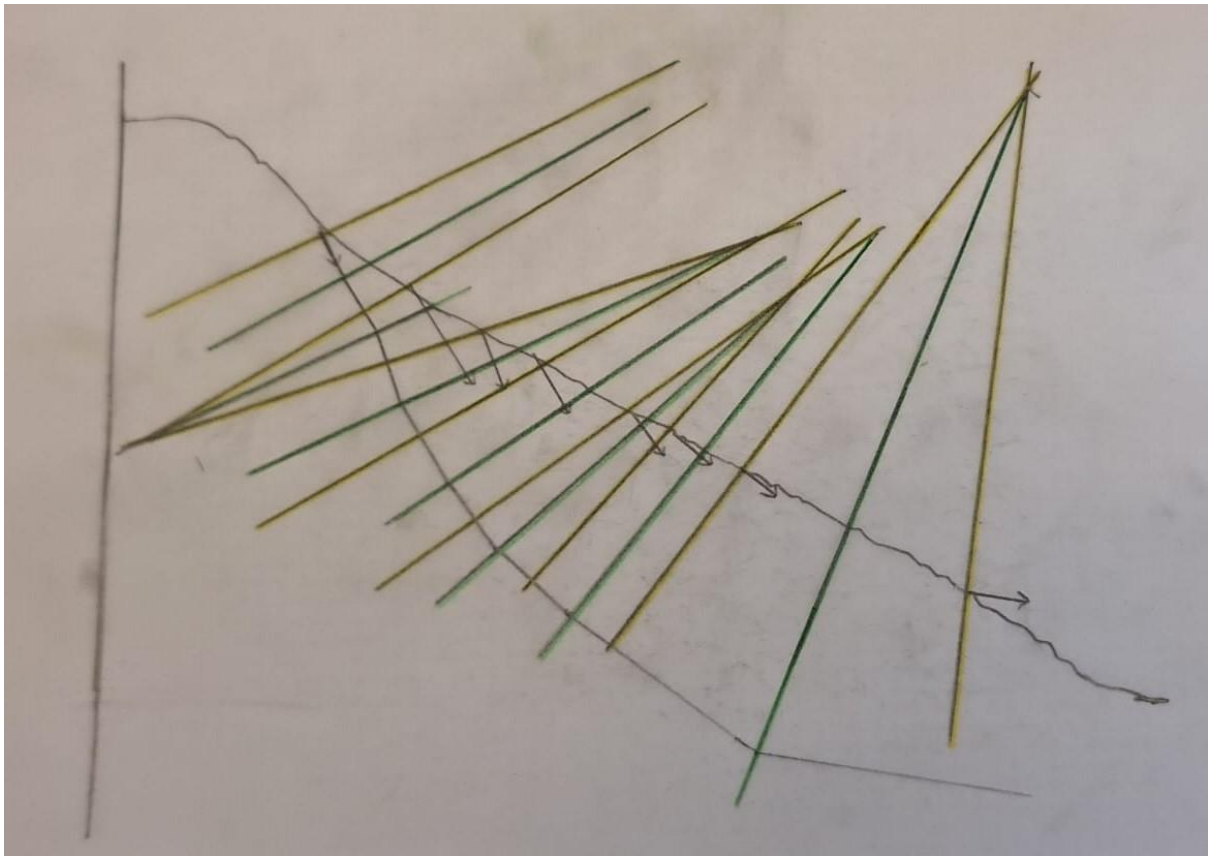

Figure 25 Result using the method presented by Intrieri et al. (2020), drawn by hand